

**MEASUREMENT OF THE PROTON
 A_1 AND A_2 SPIN ASYMMETRIES:
PROBING COLOR FORCES**

A Dissertation
Submitted to
the Temple University Graduate Board

In Partial Fulfillment of the
Requirements for the Degree of
Doctor of Philosophy

by
Whitney Richard Armstrong
Diploma Date May 2015

Examining Committee Members:

Zein-Eddine Meziani, Advisory Chair, Physics Department

Andreas Metz, Physics Department

Nikolaos Sparveris, Physics Department

Bernd Sorrow, Physics Department

Mark Jones, External Member, Jefferson Lab

©
Copyright
2015

by

Whitney Richard Armstrong

All Rights Reserved

ABSTRACT

The Spin Asymmetries of the Nucleon Experiment (SANE) measured the proton spin structure function g_2 in a range of Bjorken x , $0.3 < x < 0.8$, where extraction of the twist-3 matrix element d_2^p (an integral of g_2 weighted by x^2) is most sensitive. The data was taken from Q^2 equal to 2.5 GeV^2 up to 6.5 GeV^2 . In this polarized electron scattering off a polarized hydrogen target experiment, two double spin asymmetries, A_{\parallel} and A_{\perp} were measured using the BETA (Big Electron Telescope Array) Detector. BETA consisted of a scintillator hodoscope, gas Čerenkov counter, lucite hodoscope and a large lead glass electromagnetic calorimeter. With a unique open geometry, a threshold gas Čerenkov detector allowed BETA to cleanly identify electrons for this inclusive experiment. A measurement of d_2^p is compared to lattice QCD calculations.

To my wonderful mother, Susan.
It is what dad would have wanted.

ACKNOWLEDGMENTS

First, I must thank Zein-Eddine Meziani for giving me such a great opportunity and for all the support he provided along the way. I also want to thank the SANE spokespersons for allowing me to undertake this analysis. Specifically, I learned a great deal by chasing Mark Jones around Hall C during the experiment and having him patiently answer my questions. Also, I want to thank Oscar Rondon for his useful comments and support through every analysis meeting. Also for his careful reading of this document.

I want to thank the students and postdocs who worked on the SANE analysis. In particular, I must acknowledge the fine target analysis of James Maxwell and the elastics analysis of Anusha Liyanage, which showed that I finally got the calibrations right. I also want to thank Matt Posik and David Flay for their friendly collaborations during the past few years.

I must thank Ed Kaczanowicz for his great work and friendship. I learned a great deal from Ed and he is certainly one of Temple University's greatest assets. I cannot overstate the value of his contributions in making the SANE gas Čerenkov counter a success. There is nothing quite like Easter Sundays in Hall C.

I also must acknowledge those who guided me in the early days. I want to thank Leonard Gamberg, who always answered my theoretical questions and pointed me towards relevant and interesting reading material. Brad Sawatzky, for teaching me many things as a young student and for sharing his delicious coffee over always stimulating discussions.

Finally, I have to acknowledge my wonderful family. Without their love, patience, and support I could not have accomplished anything.

TABLE OF CONTENTS

	Page
ABSTRACT	iii
ACKNOWLEDGMENTS	vii
LIST OF TABLES	xiv
LIST OF FIGURES	xv
 CHAPTER	
1 INTRODUCTION	1
1.1 A brief historical perspective	1
1.2 Color Forces	5
1.3 Motivation	6
2 ELECTRON SCATTERING	9
2.1 Kinematics	9
2.2 Elastic Scattering	11
2.3 Resonance Production and Quasielastic Scattering	13
2.4 Deep Inelastic Scattering	15
2.4.1 Formalism	15
2.4.2 Scaling Structure Functions	17
2.4.3 Elastic Contribution	18
2.4.4 Cross Section Differences	20
2.5 Measured Asymmetries	22
2.6 Parton Model	24
2.6.1 Quark PDFs and Structure Functions	25
3 THE STRUCTURE OF THE NUCLEON	29
3.1 Moments and Models	30

	Page
3.1.1 Ellis-Jaffe Sum Rule	31
3.1.2 Bjorken Sum Rule	33
3.2 Scaling Violations	33
3.2.1 QCD Improved Parton Model	34
3.2.2 DGLAP Evolution Equations	34
3.2.3 PDFs	37
3.3 Operator Product Expansion	38
3.3.1 Higher Twists	40
3.3.2 Moments	41
3.4 Color Forces	43
3.4.1 Status of d_2	45
3.5 Remarks	46
4 THE EXPERIMENT	49
4.1 Accelerator and Beamline	49
4.1.1 Hall C Beamline	51
4.2 Polarized Target	56
4.3 BETA	59
4.3.1 BigCal	60
4.3.2 Gas Čerenkov	62
4.3.3 Lucite Hodoscope	63
4.3.4 Forward Tracker	64
4.4 Data Acquisition	65
5 DATA ANALYSIS	69
5.1 Analysis Overview	69
5.2 Clustering	70
5.2.1 Clustering Algorithm	72
5.2.2 Cluster Characterization	73
5.3 Detector Calibrations	74

	Page	
5.3.1	BigCal Energy Calibration	74
5.3.2	Gas Čerenkov	75
5.3.3	Lucite Hodoscope Calibration	77
5.3.4	Forward Tracker Calibration	79
5.4	Event Reconstruction and Selection	79
5.5	Asymmetry Measurements	82
5.5.1	Measured Asymmetry	83
5.5.2	Corrected Asymmetry	86
5.5.3	Dilution factor	87
5.6	Pair Symmetric Background	88
5.7	Radiative Corrections	89
6	RESULTS	97
6.1	Virtual Compton Scattering Asymmetries	97
6.2	Spin Structure Functions	97
6.3	Twist-3 Matrix Element	99
7	RECOMMENDATIONS	103
	REFERENCES CITED	104
A	VIRTUAL COMPTON SCATTERING ASYMMETRIES	113
A.1	Extracting Virtual Compton Scattering Asymmetries . .	116
B	OPERATOR PRODUCT EXPANSION	119
B.1	Nucleon Matrix Elements	120
B.2	Moments	121
B.2.1	Target Mass Corrections	122
B.2.2	Twist-3 Evolution Equations	123
C	ARTIFICIAL NEURAL NETWORKS	125
C.1	Network Training	125
C.2	Overview of Networks	126
C.3	Position Correction at BigCal	126

	Page
C.3.1	Photon Position Correction 127
C.3.2	Electron and Positron Corrections 130
C.4	Reconstructing Scattering Angles 131
C.5	Momentum Direction at BigCal 133
D	BIGCAL CALIBRATION 135
D.1	Event Selection 135
D.1.1	Kinematics and Geometry 136
D.2	Calibration Method 136
D.3	Calibration Procedure 139
D.3.1	Previous method 140
D.3.2	New Method 141
D.4	Independent Checks 141
E	RADIATIVE CORRECTIONS 145
E.1	The Elastic Radiative Tail 146
E.1.1	Corrections to the Elastic Peak 148
E.1.2	Internal Elastic Radiative Tail Corrections 148
E.1.3	External Corrections 150
E.2	The Inelastic Radiative Tail 151
E.2.1	Internal Corrections 151
E.2.2	Energy Peaking Approximation 152
E.3	Comparing Codes 154
E.3.1	POLRAD 155
F	PAIR SYMMETRIC BACKGROUND CORRECTIONS 159
F.1	BETA Background subtraction 159
F.2	Background Simulation 160
G	ERROR ANALYSIS 163
G.1	Statistical Uncertainty 163
G.2	Systematic Uncertainties 164

	Page
G.2.1 Measured Asymmetry	164
G.2.2 Physics Asymmetry	165
G.2.3 Pair Symmetric Background Corrected Asymmetry	165
G.2.4 Elastic Radiative Tail Correction	165
G.2.5 Inelastic Radiative Tail Correction	166
G.3 Systematic Uncertainty Estimates	166
H TABLES OF RESULTS	167
H.1 A_1 and A_2 with 4.7 GeV Beam	167
H.2 A_1 and A_2 with 5.9 GeV Beam	169

LIST OF TABLES

Table	Page
4.1 SANE triggers defined for TS and their nominal prescale factors. .	67
5.1 An outline of tasks for each analysis pass.	71
G.1 Systematic uncertainty estimates.	166
H.1 A_1 results for $1.0 < Q^2 < 2.25$ and $E = 4.7$ GeV.	167
H.2 A_1 results for $2.25 < Q^2 < 3.5$ and $E = 4.7$ GeV.	168
H.3 A_1 results for $3.5 < Q^2 < 5.0$ and $E = 4.7$ GeV.	168
H.4 A_2 results for $1.0 < Q^2 < 2.25$ and $E = 4.7$ GeV.	169
H.5 A_2 results for $2.25 < Q^2 < 3.5$ and $E = 4.7$ GeV.	169
H.6 A_2 results for $3.5 < Q^2 < 5.0$ and $E = 4.7$ GeV.	170
H.7 A_1 results for $1.0 < Q^2 < 2.25$ and $E = 5.9$ GeV.	170
H.8 A_1 results for $2.25 < Q^2 < 3.5$ and $E = 5.9$ GeV.	171
H.9 A_1 results for $3.5 < Q^2 < 5.0$ and $E = 5.9$ GeV.	171
H.10 A_1 results for $5.0 < Q^2 < 7.5$ and $E = 5.9$ GeV.	172
H.11 A_2 results for $1.0 < Q^2 < 2.25$ and $E = 5.9$ GeV.	172
H.12 A_2 results for $2.25 < Q^2 < 3.5$ and $E = 5.9$ GeV.	172
H.13 A_2 results for $3.5 < Q^2 < 5.0$ and $E = 5.9$ GeV.	173
H.14 A_2 results for $5.0 < Q^2 < 7.5$ and $E = 5.9$ GeV.	173

LIST OF FIGURES

Figure	Page
1.1 The unpolarized parton distributions (left) and the polarized parton distributions (right).	5
2.1 Elastic electron scattering	11
2.2 Exclusive resonant pion production.	13
2.3 Electron scattering cross section over a broad range of kinematics showing the elastic peak (black), resonance region (red), and the onset of the DIS region (blue). The lines of constant W are solid and the lines of constant x are dashed. Note that for the elastic peak these lines are the same $x = 1$ and $W = M_p$. Beyond the resonance region ($W > 2$ GeV and $Q^2 > 1$ GeV ² /c ²) is the deep inelastic scattering region.	14
2.4 Cross sections for scattering a 1.8 GeV electron beam from nuclear targets of deuterium (red) and carbon (blue) at 23°. The total cross sections (dashed) are shown in addition to the pure quasi-elastic contribution (solid).	15
2.5 Deep inelastic scattering scattering.	16
2.6 F_2^p over a wide range of x and Q^2 reproduced from [22].	19
2.7 Definitions of angles used in polarized DIS experiments.	21
2.8 Kinematic coverage of world data on g_1^p . Lines of constant W are shown for 1 GeV (black), 2 GeV (red), and 3 GeV (blue).	22
2.9 Kinematic coverage of world data on g_2^p . Lines of constant W are shown for 1 GeV (black), 2 GeV (red), and 3 GeV (blue).	23
2.10 Cartoon of the nucleon at increasing Q^2 values and smaller distance scales.	25
3.1 A chart outlining the various finite Q^2 corrections.	31
3.2 An example diagrams contributing to the leading order calculation of P_{qq}	35
3.3 Lead order contribution to the splitting function P_{qq} . This illustrates the coupling of the quark and gluon PDFs.	35

Figure	Page
3.4 Graphical representation of P_{ij}	38
3.5 Data on the structure function F_2^p along with the result calculated from an evolved fit [35]. The fit is calculated at the mean value of Q^2 for the selected data around $Q^2 = 2 \text{ GeV}^2$ (black) and $Q^2 = 90 \text{ GeV}^2$ (red).	39
3.6 Diagrams for operators in the twist expansion.	44
3.7 The world data on \tilde{d}_2^p from SLAC [43] (open square) and RSS [45] (filled square), and a lattice QCD calculation [46] (open circle).	46
4.1 Kinematic coverage of BETA for the two beam energies, 4.7 GeV (blue) and 5.9 GeV (red).	50
4.2 Overview of CEBAF reproduced from [47]	51
4.3 Beam energies vs run number showing two beam energies, 4.7 GeV and 5.9 GeV.	52
4.4 Layout of the hall-C Møller polarimeter. The top figure shows a close up view of the collimation system and the bottom shows a larger view including the quadrupole magnet and electron detectors.	53
4.5 Beam polarization vs run for the two helicities, positive (red) and negative (blue).	54
4.6 Target polarization by run number.	57
4.7 Drawing of the target vacuum chamber and magnet systems.	58
4.8 BETA detectors with simulated event.	59
4.9 BETA dimensions with side view (upper figure) and a top view (lower figure). Shown from left to right are the calorimeter, hodoscope, Čerenkov counter, forward tracker and polarized target.	60
4.10 BigCal timing groups and trigger summing scheme. Note that some blocks belong to more than one timing/trigger groups. See the text for more detail.	61
4.11 A simplified diagram of the BigCal electronics.	63
4.12 The SANE Gas Čerenkov counter on floor in Hall C.	64
4.13 Čerenkov counter ADC spectrum for all the toroidal mirrors (top) and spherical mirrors (bottom).	65
4.14 Photograph of three bars before mounting PMTs and wrapping.	66
4.15 Definitions of the two main triggers, BETA2 and PI0.	68

Figure	Page
5.1 Diagram demonstrating the clustering energy threshold.	72
5.2 Various classes of clusters. See text for details.	73
5.3 A fit to the calibrated two photon invariant mass spectrum near the π^0 mass peak.	75
5.4 Number of photoelectrons for each Čerenkov mirror.	76
5.5 ADC Aligned response for each Čerenkov mirror.	77
5.6 A calibration of the mirror edges.	78
5.7 An example of a Lucite Hodoscope X position calibration. Note the fit function gives the BigCal x-cluster position (vertical axis) as a function of the Lucite hodoscope bar TDC difference.	79
5.8 Definition of BETA tracking positions.	80
5.9 Results of training for a position correction δ_x . The red histogram shows the difference between the network output (black) and the training data set (blue).	81
5.10 The Čerenkov TDC peak without (black) and with (red) a time-walk correction. The Vertical lines define the TDC selection cut.	82
5.11 The Čerenkov ADC spectrum without (black) and with (red) a TDC cut. The Čerenkov ADC window cut is defined by the vertical lines.	83
5.12 The Lucite Hodoscope TDC spectrum without (black) and with (red) the Čerenkov TDC cut.	84
5.13 The charge asymmetry vs run number.	85
5.14 Asymmetries after correcting for beam polarization, target polarization, and target dilution. The top plots show the anti-parallel configuration and the bottom show the perpendicular.	86
5.15 A diagram of the target cup showing the packing fraction.	87
5.16 The dilution factor calculated for run 72925 as a function of x, showing the increasing contribution from the elastic tails at lower energies (i.e. lower x).	88
5.17 The background dilution (left), $1/f_{bg}$, and background contamination (right), C_{bg} , terms calculated for the anti-parallel 5.9 GeV configuration.	89
5.18 Same as Figure 5.14 but with the asymmetries corrected for the pair symmetric background.	90

Figure	Page
5.19 Elastic radiative tail dilution $1/f_{el}$ (left), and contamination C_{el} (right) calculated for the parallel (black) and perpendicular (red) configurations for a 4.7 GeV incident beam energy.	92
5.20 Same as Figure 5.14 but with the elastic radiative tail subtracted.	93
5.21 The inelastic radiative tail (blue), elastic radiative tail (red), and inelastic Born (black) cross sections for the anti-parallel target configuration and 5.9 GeV incident beam energy. The dashed lines are the cross sections corresponding to the two beam helicity states. .	94
5.22 The inelastic radiative tail (blue), elastic radiative tail (red), and inelastic Born (black) cross sections for the anti-parallel target configuration and 5.9 GeV incident beam energy. The dashed lines are the cross sections corresponding to the two beam helicity states. .	95
5.23 Same as Figure 5.14 but with the inelastic radiative tail corrected.	96
6.1 The results for A_1^p . The data [77–82] shown is limited to the range $8 > Q^2 > 1 \text{ GeV}^2$	98
6.2 The results for A_2^p . The data [43, 78, 80, 83, 84] shown is limited to the range $8 > Q^2 > 1 \text{ GeV}^2$	98
6.3 The results for A_1^p vs Bjorken x with model predictions for $x \rightarrow 1$.	99
6.4 The results for $x^2 g_1^p$	100
6.5 The results for $x^2 g_2^p$	101
6.6 The results for the CN moment extraction of $\tilde{d}_2^p = I(Q^2)$	101
6.7 The results of a Nachtmann moment extraction of $\tilde{d}_2^p = 2M_2^3$ shown against the existing data. [43, 44, 90]	102
A.1 The results for A_2^p . The data [43, 78, 80, 83, 84] shown is limited to the range $8 > Q^2 > 1 \text{ GeV}^2$. Also shown is the Soffer limit [92] for two $Q^2 = 2$ and 6 GeV^2	117
C.1 A blown up view of the BigCal plane where the cluster position is corrected. Note the BigCal plane is actually flush with the front face of the calorimeter.	128
C.2 An example of the y position correction network for photons. The thickness of the line indicates the trained neuron’s output weight for the neurons in the following layer.	129
C.3 Histogram show the size of the impact on the y position correction caused by a small change in the input variables of the test dataset.	129

Figure	Page
C.4 Same as Figure C.4 but for the x position correction.	130
C.5 Results of training for the photon's correction δ_x . The red histogram shows the difference between the network output (black) and the training data set (blue).	131
C.6 An Electron angle correction neural network.	132
C.7 Histograms showing the impact of the inputs, shown in Figure C.6, on the angle correction, $\delta\theta$	133
C.8 Same as Figure C.7 but for the angle correction $\delta\phi$	134
D.1 The BigCal calibration sectors are shown in Figures (a-f). All active blocks participating in calibrating sector (f) are shown in (g). . .	140
D.2 The elastic events energy difference checking the energy reconstruction of BigCal [106].	142
E.1 Elastic radiative tail (black) for 5.5 GeV incident electrons scattered at 40° . The elastic cross section is shown in blue (solid) for the incident beam energy. It is also shown for lower incident energies (dashed). The arrows point to the location of the elastic peak for scattering at 40°	147
E.2 Feynman diagrams for calculating radiative corrections.	149
E.3 The difference between asymmetries of the elastic radiative tail calculated from the same input model using the two methods described in the text.	150
E.4 Comparisons between different codes and methods for calculating the internal contribution to the inelastic radiative tail	151
E.5 The inelastic asymmetry correction (equation 5.18) calculated from the same input model using two different internal radiative correction methods: the equivalent radiator (red) and the polarized treatment (blue).	152
E.6 A comparison of the inelastic radiative tail for different cross models.	153
E.7 The asymmetries of the inelastic cross sections shown in Figure E.6.	154
E.8 The inelastic asymmetry correction calculated using two very different cross section models.	155
E.9 The extreme case of any model dependence on the elastic radiative tail. The dipole form factors were used as a baseline comparison.	156

Figure	Page
F.1 The energy distribution of the reconstruction of simulated events. The blue curve shows the relative yield for events that originate with a scattered electron. The green and pink curves show the diluting background events with and without a Čerenkov ADC window cut. Similarly, the red and black show the sum of all events with and with the window cut.	161
F.2 The ratio of positrons to electrons from simulation with and without a Čerenkov ADC window cut applied.	161

CHAPTER 1

INTRODUCTION

The strong force is responsible for the formation of the nucleon and all atomic nuclei. Although four orders of magnitude smaller in size than the atom, the nucleus accounts for almost all the mass of an atom. The correct theory of the strong force is believed to be quantum chromodynamics (QCD) where the equations of motion describe near massless quarks and massless gluon fields. It remains a mystery exactly how almost all the mass of the observable universe (i.e. the mass of atomic nuclei) is generated from the interactions of these quark and gluon fields.

Before diving directly into the motivating theory and experiment at hand, it is instructive to look to the past in order to provide the context for our current knowledge of the strong force. In a non-technical way, we begin with a very brief and incomplete history of nuclear physics in order to emphasize the importance of small steps in advancing our understanding.

1.1 A brief historical perspective

In 1911 Rutherford formulated an atomic model which concentrated the atomic mass almost entirely in the center of the atom [1], giving birth to the now familiar atomic nuclei. Later, in 1919, he identified the proton. James Chadwick deduced the existence of the neutron [2] in 1932, the missing particle needed to explain the hierarchy in the masses of the nucleus.¹ It is worth noting

¹Various models were considered for the neutron by Rutherford and collaborators. One such model was an atom within an atom, where the neutral particle is an electron somehow embedded in a proton. In hindsight, this model is quite close to the constituent quark model of the nucleon!

that Chadwick's discovery was motivated by some results of the Joliot-Curies, where after bombarding paraffin with a neutral and strongly penetrating form of radiation, they erroneously attributed the apparent excess of ejected protons to the absorption of what they thought were photons. Upon the suggestion of Rutherford, Chadwick had already been looking for a neutral particle similar in mass to the proton. Through careful experiment and analysis he was able to discover what the Joliot-Curies had overlooked earlier that year.

From the time of Rutherford's discovery of the nucleus over 20 years had passed until the identification of its basic ingredients, namely the proton and neutron. This passage of time begins to highlight the difficulty of understanding the nucleus.

In 1933, one year after the discovery of the neutron, Stern and collaborators measured the magnetic moment of the proton, finding an unexpectedly large value. This was the first indication that the nucleon was a composite particle. By 1940 Alvarez and Block [3] measured the magnet moment of the neutron to a similar precision and write in their conclusion:

The fact alone that μ_p differs from unity and μ_n differs from zero indicates that, unlike the electron, these particles are not sufficiently described by the relativistic wave equation of *Dirac* and that other causes underly their magnetic properties.

Another 14 years passed until Hofstadter, in 1956 [4], using elastic electron scattering, clearly showed that protons and neutrons have a finite size and are not elementary particles. This discovery marked the beginning of investigation of nucleon structure.

Enter Quarks

Following the discovery that the nucleon was not elementary, it took less than a decade for theoretical physicist, Gell-Mann [5], to propose the "eight-fold

way” and subsequent quark model which explained the ever increasing “zoo” of particles being discovered at higher and higher energy accelerators.

A few year after the prediction of the new elementary particles, the SLAC-MIT [6, 7], experiments probed the nucleon through deep inelastic electron scattering in order to try to understand its composition. The results showed that the nucleon contained nearly free, non-interacting point-like particles. For a detailed review of the history of deep inelastic scattering the reader is referred to [8] [9] [10].

The 1964 prediction of quarks by Gell-Mann [5] and Zweig [11] made the results of the MIT-SLAC experiments (1967-1973) the first concrete evidence for the existence of quarks.

Today, the existence of quarks is widely accepted². There is a large body of evidence supporting the existence of quarks, however, a direct measurement of a free quark (in a detector) has never been achieved. After half a century, this problem still persists and is known phenomenologically as *confinement*.

QCD and Asymptotic Freedom

Soon after the quark model was proposed, it was realized that a few of the new hadrons like the Δ^{++} and the Ω^- were violating the Pauli exclusion principle and should not exist. In the quark model these particles would have a symmetric wave function but the wave function should be anti-symmetric for a fermion. In order to anti-symmetrize the wave function a new additional internal degree of freedom called *color* was introduced by Greenberg [12].

The theory of the strong force, quantum chromodynamics, was solidified by Fritsch, Gell-Mann and Leutwyler [13], who wrote down the Lagrangian as

$$\mathcal{L} = \bar{q}(x)[\gamma_\mu D^\mu - m]q(x) - \frac{1}{4}G^{\mu\nu}G_{\mu\nu} \quad (1.1)$$

²Half of the Standard Model’s fermions are quarks, which make up all hadronic matter. Hadronic matter makes up 99.9% of all atomic matter.

where $q(x)$ is the quark field, D is the gauge covariant derivative, and G is the gluon field strength tensor. This looks just like the QED Lagrangian except for the covariant derivative and field strength tensors, which are slightly different because QCD is a non-Abelian gauge theory. Embodied in this difference is the fact that, at leading order, gluons interact with other gluons unlike their QED analog, photons, which do not.

In 1973 Gross, Politzer, and Wilczek [14, 15] show that the interactions between quarks in QCD become increasingly weaker at higher energies. Known as *asymptotic freedom*, this property forms the empirical backbone of QCD. It permits tractable perturbative calculations to be performed for high energy scattering which agree very well with experiment.

Partons and Color Confinement

While perturbative QCD (pQCD) calculations are useful at high energies, the low energy structure of the vacuum and the nucleon is very complicated. Therefore a natural starting point for describing hadronic matter begins at high energies where theoretical calculations can be performed.

The parton model introduced in 1969 treats the quarks as non-interacting particles in the infinite momentum frame [16, 17]. In this picture of a hadronic system the transverse motion of quarks and gluons is suppressed due to the large Lorentz boost and only the longitudinal momentum is relevant. Many experiments and analyses have been performed to measure and extract these longitudinal parton distribution functions (PDFs) for unpolarized and polarized quarks and gluons as shown in Figure 1.1.

About three decades of experiments were devoted to measuring the PDFs and testing pQCD. Although providing a useful flavor decomposition of the nucleon's structure, the PDFs provide little insight into the color structure of the nucleon. This is because their starting point was specifically chosen nearest to asymp-

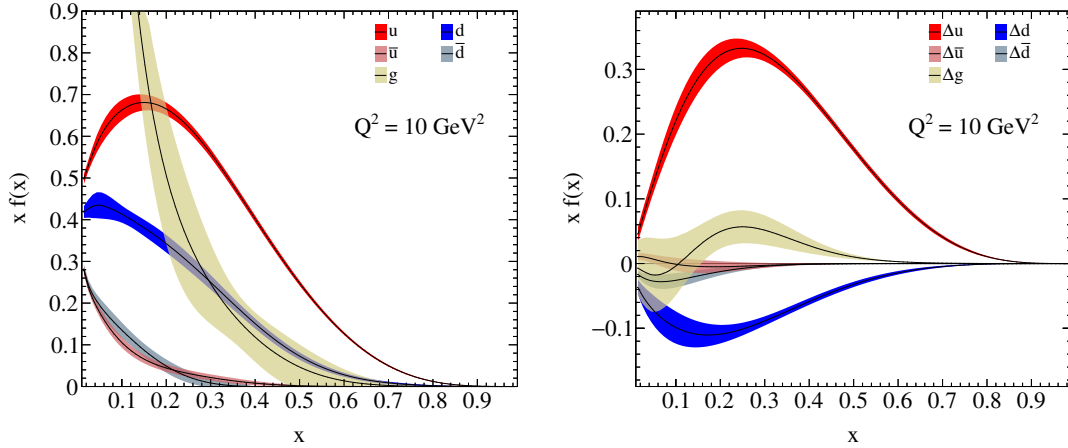


Figure 1.1.: The unpolarized parton distributions (left) and the polarized parton distributions (right).

totically free QCD to avoid the consequences of strongly coupled and confined quarks.

Color confinement states that all observable particles are color singlets, that is, they are *neutrally color charged*. Quarks and gluons only appear in tightly bound hadronic states which consist of two or more constituent quarks, but in QCD these hadrons are states of many (infinite) current quarks and gluons. Most of the successes of QCD come from the perturbative regime where the coupling constant is small. However, the exact nature of confinement and the behavior of the color fields remains unknown and locked in the PDFs.

1.2 Color Forces

The longitudinal PDFs are an important starting point for a description of the nucleon, however, they do not provide a complete description. In recent years the parton distributions have been generalized to larger dimensions and different variables. The transverse momentum distribution (TMD) is a function of longitudinal and transverse momentum, but appear only in high energy (or hard) semi-inclusive reactions. Generalized parton distributions (GPDs) have an

additional momentum variable as well, but appear in hard exclusive reactions. Without going into further detail, these distributions have been further generalized and are ultimately related to parton correlation functions of increasing complexity.

These distributions only provide a framework; they are a starting point from which the nucleon can be systematically decomposed. Each type of parton distribution has a domain of applicability and they become difficult to measure as their phase space increases. Furthermore, with the exception of the longitudinal PDFs, the experimental reactions for TMDs and GPDs require input from non-perturbative fragmentation functions that describe the formation of hadrons. This is, of course, a consequence of color confinement which remains a mystery and further complicates their analysis.

On the other hand, precision polarized deep inelastic scattering experiments with longitudinal *and* transverse target polarizations have a *unique opportunity* to measure a transverse *average color Lorentz force* that a quark feels just after absorbing a virtual photon [18]. It should be emphasized that this is a clean process free of fragmentation functions or other factorization dependent distributions.

1.3 Motivation

As will be discussed in the coming chapters, there is much to be learned from studying the spin structure of the nucleon. The ultimate goal is to test our knowledge of the strong force and provide insight into corners where theory becomes very difficult. Somehow QCD conspires to keep color confined and everything color neutral. In the spirit of Chadwick's discovery of the neutron through careful attention to detail and experiment, and with some theoretical tools, we may begin to peek through the veil of color confinement.

Polarized deep-inelastic electron scattering uniquely provides a way to measure an average color-Lorentz force. The scale dependence of this force can provide insight into how QCD confines color within the nucleon, and perhaps more importantly, it can give a better idea of exactly where to look in future experiments [19].

This thesis begins with a chapter devoted to the formalism of electron scattering. Chapter 3 will discuss the structure of the nucleon and theoretical tools needed to extract a color force. Chapters 4 and 5 present the apparatus and data analysis. Final results are presented in chapter 6 followed by a discussion of their impact.

CHAPTER 2

ELECTRON SCATTERING

In order to study structure at smaller sizes, scattering experiments use higher energy particles. Hofstadter scattered 100 MeV to 400 MeV electrons from various nuclei to determine their size and charge densities. Scattering electrons at energies of 20 GeV, the early SLAC-MIT experiments [6, 7] were able to determine the existence of point-like particles inside the nucleon. HERA, the first (and currently only) electron-proton collider had a center of mass energy above 300 GeV and was able to scan a wide range of kinematics at which the nucleon's point-like constituents appear as non-interacting particles. We now know these point-like particles to be the quarks confined within the nucleon exhibiting a scaling property, a consequence of an asymptotically free strong force.

Before diving too much into the nucleon structure, we must first discuss the techniques of electron scattering experiments used to probe said structure. This chapter begins by defining the kinematic variables used in electron scattering. This followed by a brief discussion of elastic scattering and resonance production cross sections. Then formal definitions of the nucleon's unpolarized and polarized structure functions are presented, followed by a discussion of its physical interpretation and the parton model.

2.1 Kinematics

Lepton scattering typically is given by the exchange of a single virtual photon, a consequence of the Born approximation. Furthermore, the lepton mass is neglected, which is a good approximation for most electron scattering experiments. The incoming (outgoing) electron energy is E (E'). The initial and final four

momenta, k and k' , are labeled in Figure 2.1 and their difference defines a four momentum transfer $q = k - k'$. The momentum transfer is usually characterized by the (lab) photon energy, ν , and invariant $Q^2 = -q^2$.

The target nucleus mass is M . The initial and final hadronic four momentum are P and P' . The final target system has an invariant mass squared $W^2 = (P - P')^2$.

The scalar invariants $x = Q^2/2P \cdot q$ and $y = P \cdot q/P \cdot k$ are commonly used. The former, as we will see, plays a special role in deep inelastic scattering. For reference, common kinematic variables are defined below in the laboratory system for fixed target experiments.

$$P = (M, \vec{0}) \quad (2.1)$$

$$k = (E, \vec{k}) \quad (2.2)$$

$$k' = (E', \vec{k}') \quad (2.3)$$

$$\nu = E - E' \quad (2.4)$$

$$Q^2 = -q^2 = 4EE' \sin^2(\theta/2) \quad (2.5)$$

$$W^2 = M^2 + 2M\nu - Q^2 \quad (2.6)$$

$$x = \frac{Q^2}{2M\nu} \quad (2.7)$$

$$y = \frac{\nu}{E} \quad (2.8)$$

$$\epsilon = \left[1 + 2 \left(1 + \frac{\nu^2}{Q^2} \right) \tan^2(\theta/2) \right]^{-1} \quad (2.9)$$

$$\gamma^2 = \frac{Q^2}{\nu^2} \quad (2.10)$$

$$\xi = \frac{2x}{1+r} \quad (2.11)$$

$$r = \sqrt{1 + \frac{4x^2 M^2}{Q^2}} \quad (2.12)$$

The scattering kinematics can be split up into three different regions that depend on which process dominates the cross section. They are the elastic, resonance, and deep inelastic regions and discussed in following sections.

2.2 Elastic Scattering

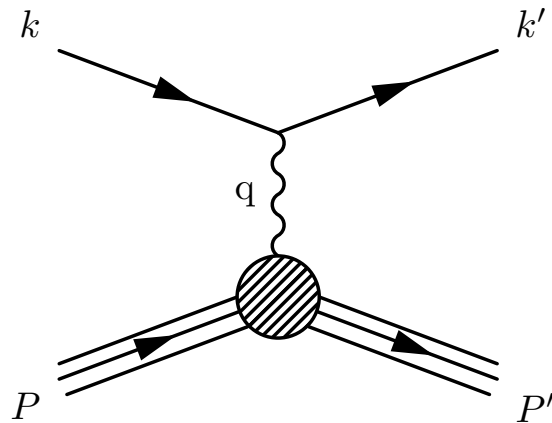


Figure 2.1.: Elastic electron scattering

The differential cross section for scattering relativistic electrons from a point-like particle with no structure and mass M is given by

$$\left(\frac{d\sigma}{d\Omega}\right)_{NoSt} = \left(\frac{d\sigma}{d\Omega}\right)_{Mott} \frac{E'}{E}. \quad (2.13)$$

The Mott cross section formula [20] for a target of infinite mass, i.e., a target that does not recoil, is given by

$$\begin{aligned} \left(\frac{d\sigma}{d\Omega}\right)_{Mott} &= \frac{\alpha^2}{4E^2} \left(\frac{\cos^2(\theta/2)}{\sin^4(\theta/2)}\right) \\ &= \left(\frac{2\alpha E' \cos(\theta/2)}{Q^2}\right)^2. \end{aligned} \quad (2.14)$$

The last term in equation 2.13 is known as the “recoil factor”. This term is necessary for targets of finite mass and is commonly written as

$$\frac{E'}{E} = \frac{1}{1 + \tau} \quad (2.15)$$

where $\tau = Q^2/4M^2$.

For electron-proton scattering the elastic peak is located at invariant mass $W = M_p$ as shown in Figure 2.3 which shows the cross section divided by the Mott cross section as a function of ν and Q^2 . In order to account the proton’s structure two form factors describing the charge and magnetic response of the proton are introduced.

The Rosenbluth [21] formula for elastic scattering is

$$\frac{d\sigma}{dE'd\Omega} = \left(\frac{d\sigma}{d\Omega} \right)_{NoSt} \left[G_E^2(Q^2) + \frac{\tau}{\epsilon} G_M^2(Q^2) \right] \quad (2.16)$$

where G_E and G_M are the Sachs electric and magnetic form factors respectively. The Sachs form factors are related to the Dirac (F_1) and Pauli (F_2) form factors by

$$G_E = (F_1 + \tau F_2), \quad G_M = (F_1 + F_2) \quad (2.17)$$

For real photons, $Q^2 = 0$, the proton and neutron form factors reduce to

$$G_E^p(Q^2 = 0) = 1, \quad G_M^p(Q^2 = 0) = \mu_p \quad (2.18)$$

$$G_E^n(Q^2 = 0) = 0, \quad G_M^n(Q^2 = 0) = \mu_n \quad (2.19)$$

reflecting their respective electric charges and magnetic moments.

In order to isolate the electric and magnetic contributions from the experimental cross sections, a so-called *Rosenbluth separation* is commonly performed by measuring the cross section at a fixed value of Q^2 for different values of ϵ . This

typically requires a small (forward) angle measurement and a large (backward) angle measurement. By rewriting 2.16 as

$$\frac{\tau}{\epsilon} \left(\frac{d\sigma}{dE'd\Omega} \right)_{exp} / \left(\frac{d\sigma}{d\Omega} \right)_{NoSt} = \frac{\epsilon}{\tau} G_E^2(Q^2) + G_M^2(Q^2) \quad (2.20)$$

where τ is constant, and by fitting the l.h.s. with the experimental cross sections as a linear function of ϵ , the form factors can be separated at constant Q^2 . The electric form factor is proportional to the slope and the magnetic form factor is the intercept of the fit.

2.3 Resonance Production and Quasielastic Scattering

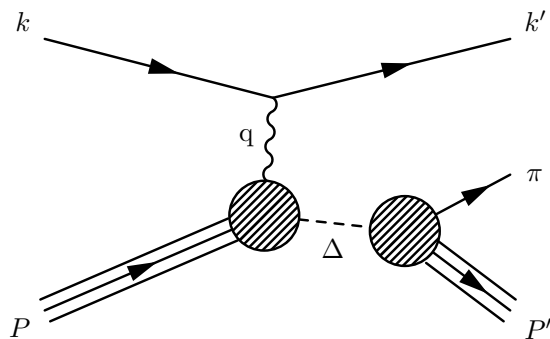


Figure 2.2.: Exclusive resonant pion production.

For elastic scattering the final state is simply the recoiling target, i.e., $W = M$. At a fixed value of Q^2 , W increases with increasing photon energy, ν , and the cross section displays a series of resonance peaks associated with the production of Δ and other nucleon resonances as shown in Figure 2.2. This region between the elastic peak and $W = 2$ GeV is therefore called the *resonance region*. Figure 2.3 shows the electron scattering cross section as function of ν and Q^2 . The resonance region (red) sits between the elastic peak (black) and the deep inelastic scattering region. Lines of constant W (solid) are parallel to each other and the Δ resonance sits at $W = M_\Delta \simeq 1.232$ GeV. Lines of constant $x = Q^2/2M\nu$ are

shown as dashed lines. Note that the elastic peak at $W = M_p$ coincides with the line of constant $x = 1$.

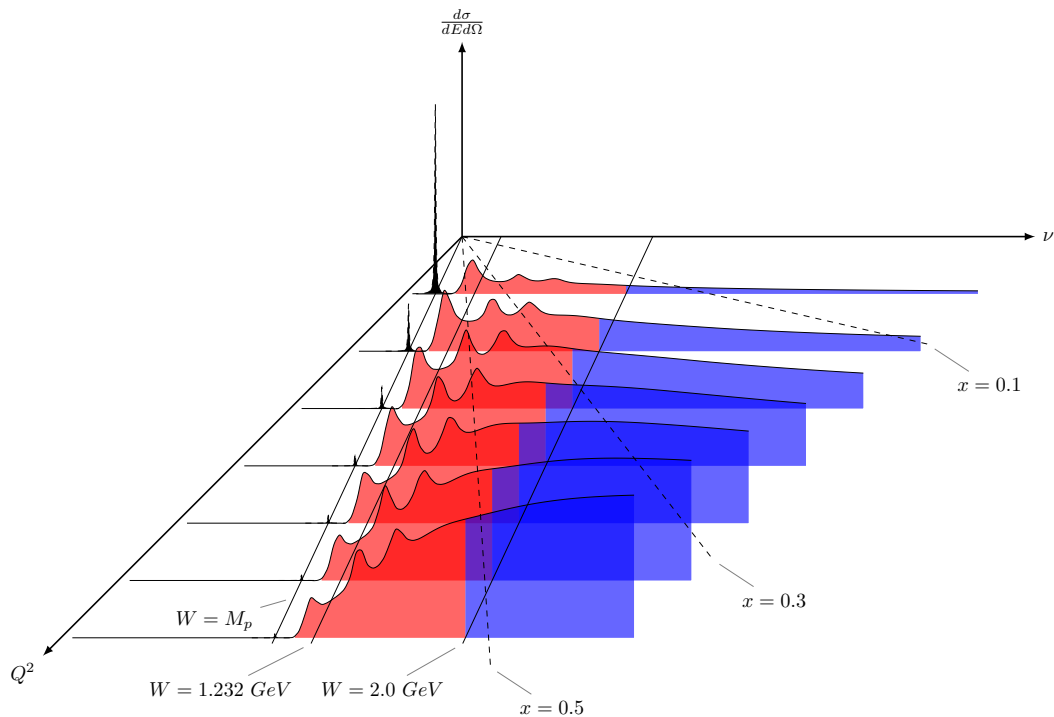


Figure 2.3.: Electron scattering cross section over a broad range of kinematics showing the elastic peak (black), resonance region (red), and the onset of the DIS region (blue). The lines of constant W are solid and the lines of constant x are dashed. Note that for the elastic peak these lines are the same $x = 1$ and $W = M_p$. Beyond the resonance region ($W > 2 \text{ GeV}$ and $Q^2 > 1 \text{ GeV}^2/c^2$) is the deep inelastic scattering region.

Electron scattering from nuclear targets is characterized by an extra feature absent for a proton target, namely the quasi-elastic scattering of an electron from a nucleon bound in a nucleus. The Fermi motion of a bound nucleon gives width to the so-called quasi-elastic peak which is centered around $W = M_p$. Figure 2.4 shows the contribution of the quasi-elastic peak near the resonance region for deuterium and carbon targets. The quasielastic peak is less pronounced in carbon due to the larger Fermi momentum. Similarly, the nucleon resonances peaks become wider due to Fermi motion.

Like the various peaks in the resonance region, the quasielastic peak also decreases with increasing Q^2 because the relative contribution from deep inelastic scattering is growing.

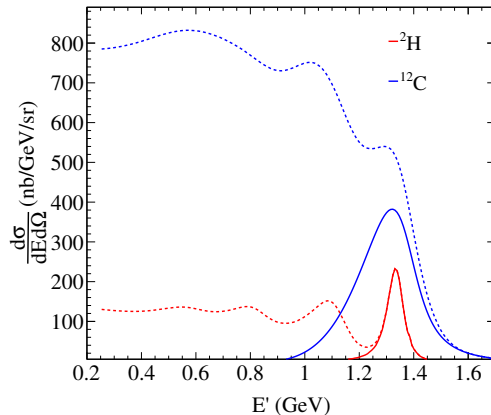


Figure 2.4.: Cross sections for scattering a 1.8 GeV electron beam from nuclear targets of deuterium (red) and carbon (blue) at 23° . The total cross sections (dashed) are shown in addition to the pure quasi-elastic contribution (solid).

2.4 Deep Inelastic Scattering

The deep inelastic regime sets in when high energy leptons are scattered with momentum transfers $Q^2 > 1(\text{GeV}/c)^2$ and large invariant mass $W > 2\text{GeV}$. The target system is broken apart into many hadrons which are not detected. These final state target remnants are labeled by X in Figure 2.5. The virtual photon exchanged probes the target at scales distance inversely proportional to Q .

2.4.1 Formalism

We begin by writing down the general tensor form of the cross section for the reaction

$$\vec{e}(k) + \vec{N}(P) \rightarrow e(k') + X \quad (2.21)$$

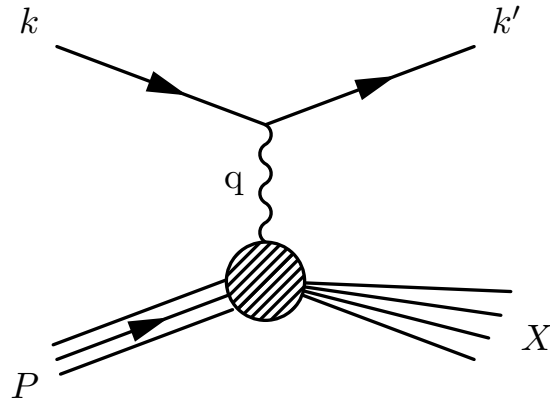


Figure 2.5.: Deep inelastic scattering.

where the arrows above the initial electron and target indicate they are polarized. The inclusive differential cross section for scattering into the solid angle $d\Omega$ and with an energy between E' and $E' + dE'$ is

$$\frac{d^2\sigma}{d\Omega dE'} = \frac{\alpha^2}{2Mq^4} \frac{E'}{E} L_{\mu\nu} W^{\mu\nu}, \quad (2.22)$$

where $L_{\mu\nu}$ and $W^{\mu\nu}$ are the leptonic and hadronic tensors respectively.

In general, $L_{\mu\nu}(k, s, k', s')$ is a function of the incoming and outgoing electron momenta and spins. Summing over s' because the polarization of the scattered lepton is not measured, we obtain

$$L_{\mu\nu}(k, s, k') = 2L_{\mu\nu}^S(k, k') + 2iL_{\mu\nu}^A(k, s, k') \quad (2.23)$$

where

$$L_{\mu\nu}^S(k, k') = k_\mu k'_\nu + k'_\mu k_\nu - g_{\mu\nu} (k \cdot k' - m^2) \quad (2.24)$$

$$L_{\mu\nu}^A(k, s, k') = m\epsilon_{\mu\nu\alpha\beta} s^\alpha (k - k')^\beta. \quad (2.25)$$

Averaging over the initial lepton spin yields the symmetric part of the leptonic tensor $L_{\mu\nu}^S$ which is the first term on the r.h.s. of equation 2.23.

Similarly, the hadronic tensor can be decomposed into symmetric and anti-symmetric parts,

$$W_{\mu\nu}^A(P, q, S) = W_{\mu\nu}^S(P, q) + iW_{\mu\nu}^A(P, q, S) \quad (2.26)$$

For an unpolarized target only the symmetric part of the tensor contributes to the cross section and it is given by

$$\begin{aligned} W_{\mu\nu}^S = 2M & \left[-g_{\mu\nu} + \frac{q_\mu q_\nu}{q^2} \right] W_1(\nu, Q^2) \\ & + \frac{2}{M} \left[P_\mu - \frac{P \cdot q}{q^2} q_\mu \right] \left[P_\nu - \frac{P \cdot q}{q^2} q_\nu \right] W_2(\nu, Q^2). \end{aligned} \quad (2.27)$$

where S is the target covariant spin vector, W_1 and W_2 are the unpolarized structure functions. For a polarized target the asymmetric part also contributes

$$\begin{aligned} W_{\mu\nu}^A = 2M^2 & \epsilon_{\mu\nu\lambda\sigma} q^\lambda S^\sigma G_1(\nu, Q^2) \\ & + 2M \epsilon_{\mu\nu\lambda\sigma} q^\lambda [P \cdot q S^\sigma - S \cdot q P^\sigma] G_2(\nu, Q^2) \end{aligned} \quad (2.28)$$

where G_1 and G_2 are the polarized structure functions.

2.4.2 Scaling Structure Functions

The results from the SLAC-MIT experiments showed that the structure function $W_2(\nu, Q^2)$ at large Q^2 displayed a scaling behavior. They appear to be a function of only ν and becoming approximately independent of Q^2 . As will be discussed further in section 2.6, it is convenient to introduce the dimensionless structure functions defined as

$$F_1(x, Q^2) = MW_1(\nu, Q^2), \quad (2.29)$$

$$F_2(x, Q^2) = \nu W_2(\nu, Q^2), \quad (2.30)$$

$$g_1(x, Q^2) = M^2 \nu G_1(\nu, Q^2), \quad (2.31)$$

and

$$g_2(x, Q^2) = M \nu^2 G_2(\nu, Q^2). \quad (2.32)$$

The hadronic tensor in terms of these structure functions becomes

$$\begin{aligned} W_{\mu\nu} = & 2 \left[-g_{\mu\nu} + \frac{q_\mu q_\nu}{q^2} \right] F_1(x, Q^2) \\ & + \frac{2}{M\nu} \left[P_\mu - \frac{P \cdot q}{q^2} q_\mu \right] \left[P_\nu - \frac{P \cdot q}{q^2} q_\nu \right] F_2(x, Q^2) \\ & + i \frac{2M}{P \cdot q} \epsilon_{\mu\nu\lambda\sigma} q^\lambda S^\sigma g_1(x, Q^2) \\ & + i \frac{2M}{(P \cdot q)^2} \epsilon_{\mu\nu\lambda\sigma} q^\lambda [(P \cdot q) S^\sigma - (S \cdot q) P^\sigma] g_2(x, Q^2). \end{aligned} \quad (2.33)$$

Scaling is clearly demonstrated in Figure 2.6 where the F_2 is plotted for a wide range in x and Q^2 . At low x and Q^2 scaling violations are observed, however, as we will discuss in chapter 3, pQCD calculations turn these violations into the predictable logarithmic scaling violations, one of the primary successes of QCD.

2.4.3 Elastic Contribution

If we restrict the kinematics to elastic scattering, i.e. $x = 1$, the structure functions are related to the electric and magnetic form factors through

$$F_1^{el} = \delta(x - 1) M \tau G_M^2(Q^2) \quad (2.34)$$

$$F_2^{el} = \delta(x - 1) 2M\tau \frac{G_E^2(Q^2) + \tau G_M^2(Q^2)}{1 + \tau} \quad (2.35)$$

$$g_1^{el} = \delta(x - 1) G_M(Q^2) \frac{G_E(Q^2) + \tau G_M(Q^2)}{2(1 + \tau)} \quad (2.36)$$

$$g_2^{el} = \delta(x - 1) \tau G_M(Q^2) \frac{G_E(Q^2) - G_M(Q^2)}{2(1 + \tau)} \quad (2.37)$$

Placing these into 2.33 and averaging the cross section over the spins yields the Rosenbluth formula for elastic scattering 2.16.

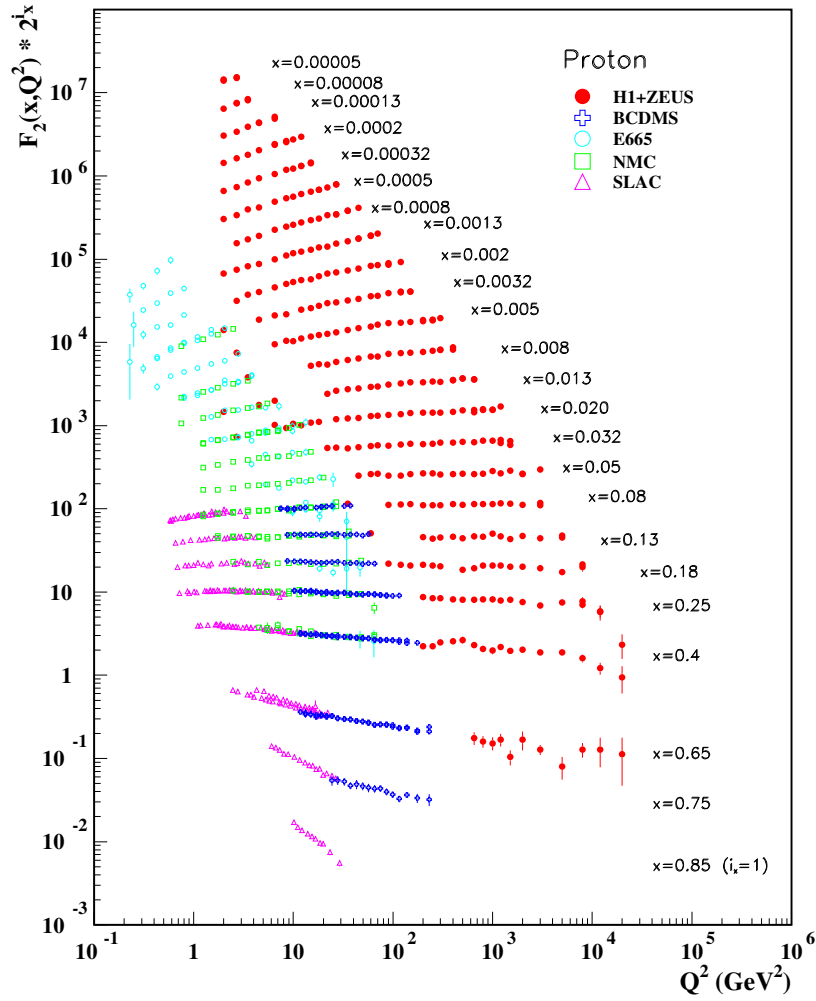


Figure 2.6.: F_2^p over a wide range of x and Q^2 reproduced from [22].

Like in the case of elastic scattering, the unpolarized structure functions are separated from the unpolarized cross section via a Rosenbluth separation. This involves measuring the cross section at fixed Q^2 for many different angles (or ϵ). This angular dependence can be easily understood by writing the unpolarized cross section as

$$\sigma_0 = \frac{4\alpha^2 E'^2}{q^4} [2W_1 \sin^2(\theta/2) + W_2 \cos^2(\theta/2)]. \quad (2.38)$$

2.4.4 Cross Section Differences

Using a polarized electron beam and a polarized target, the cross section difference of opposite nucleon polarization states is given by [23]

$$\begin{aligned}
\Delta\sigma(k) &= \frac{d^2\sigma}{dE'd\Omega}(k, s, S) - \frac{d^2\sigma}{dE'd\Omega}(k, s, -S) \\
&= \frac{-\alpha^2}{2Mq^4} \frac{E'}{E} (2L_{\mu\nu}^{(A)} W^{\mu\nu(A)}) \\
&= \frac{8m\alpha^2 E'}{q^4 E} \left[\frac{1}{M\nu} ((q \cdot S)(q \cdot s) + Q^2(s \cdot S)) g_1 \right. \\
&\quad \left. + \frac{Q^2}{M^2\nu^2} ((s \cdot S)(P \cdot q) - (q \cdot x)(P \cdot s)) g_2 \right]
\end{aligned} \tag{2.39}$$

With a longitudinally polarized electron beam this cross section difference reduces to¹

$$\Delta\sigma(k) = -\frac{4\alpha^2}{Q^2} \frac{E'}{E} [(E \cos \alpha + E' \cos \Theta)MG_1 + 2EE'(\cos \Theta - \cos \alpha)G_2] \tag{2.40}$$

where the angles are defined as shown in Figure 2.7. The angles α (polar) and β (azimuth) define the target spin vector. The angle between the target spin and outgoing electron is

$$\cos \Theta = \sin \theta \sin \alpha \cos \phi + \cos \theta \cos \alpha \tag{2.41}$$

and $\phi = \beta - \varphi$ is the angle between the scattering plane (formed by \vec{k} and \vec{k}') and the polarization plane (formed by \vec{k} and \vec{S}).

¹This result is at leading order in m/E . It is worth noting the appearance of m/E in 2.39 is canceled by the longitudinally polarized electron's Lorentz transformed spin vector, $s_{\parallel} \simeq (E/m)(1, \hat{z})$, whereas for transversely polarized electrons the spin vector, $s_{\perp} = (0, \vec{s}_{\perp})$, contains no such enhancement. Consequently, the cross section for transversely polarized electrons is suppressed by (m/E) relative to longitudinal cross section and therefore can be safely ignored when the beam is not 100% longitudinally polarized.

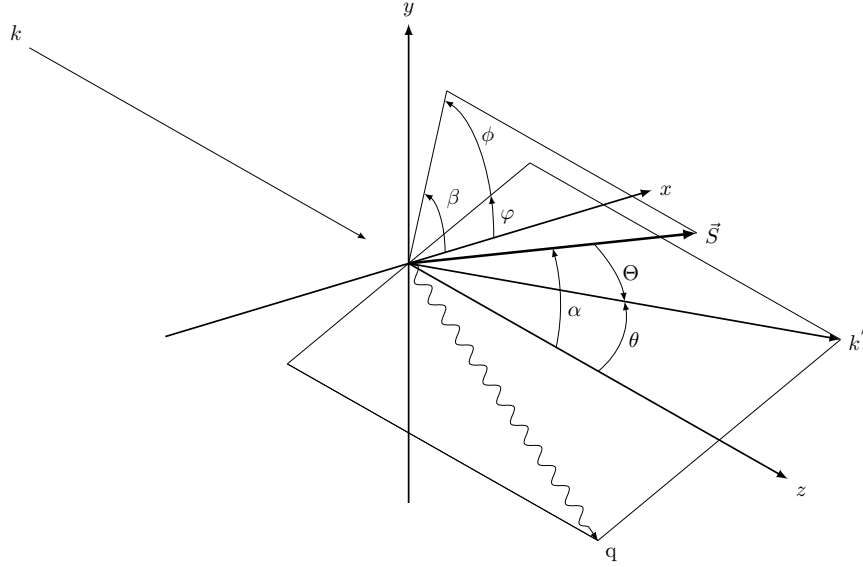


Figure 2.7.: Definitions of angles used in polarized DIS experiments.

The need for a transverse target

The cross section difference in 2.40 is sensitive to both polarized structure functions. Using a longitudinally polarized target the difference becomes

$$\Delta\sigma_{\parallel}(k) = -\frac{4\alpha^2}{Q^2} \frac{E'}{E} \left[(E + E' \cos \theta) \frac{1}{M\nu} g_1 - \frac{Q^2}{M\nu^2} g_2 \right]. \quad (2.42)$$

At first glance, a Rosenbluth-like separation of g_1 and g_2 might be considered. However, cleanly separating the contributions of g_1 and g_2 is made difficult by the presence of the extra factor of $1/\nu$ in front of g_2 which suppresses its contribution relative to g_1 . That is, a measurement of $\Delta\sigma_{\parallel}$ is generally insensitive to g_2 .

For a transversely polarized target 2.40 becomes

$$\Delta\sigma_{\perp}(k) = -\frac{4\alpha^2}{Q^2} \frac{E'^2}{E} \sin \theta \cos \phi \left[\frac{1}{M\nu} g_1 - \frac{2E}{M\nu^2} g_2 \right]. \quad (2.43)$$

The extra factor of $2E$ in front of g_2 cancels the extra factor of $1/\nu$, leading to a measurement that is equally sensitive to g_1 and g_2 .

It should be emphasized that in order to measure the g_2 structure function, both longitudinal and transverse targets are necessary. Experimentally, longitudinal targets are typically much easier, thus significantly more data exists for g_1 as is shown by comparing Figures 2.8 and 2.9, which show their kinematic coverage in x and Q^2 .

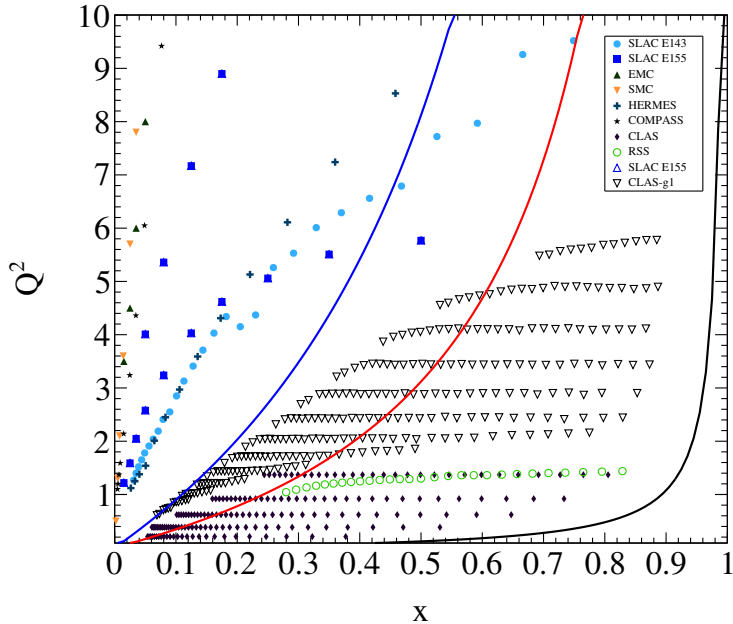


Figure 2.8.: Kinematic coverage of world data on g_1^p . Lines of constant W are shown for 1 GeV (black), 2 GeV (red), and 3 GeV (blue).

2.5 Measured Asymmetries

It is easier to measure an asymmetry instead of cross sections because many systematic effects, such as acceptance corrections and detection efficiencies, cancel in the ratio. Therefore, the asymmetries

$$A_{\parallel} = \frac{d\sigma^{\uparrow\uparrow} - d\sigma^{\uparrow\downarrow}}{d\sigma^{\uparrow\uparrow} + d\sigma^{\uparrow\downarrow}} = \frac{d\sigma^{\uparrow\uparrow} - d\sigma^{\uparrow\downarrow}}{2\sigma_0} \quad (2.44)$$

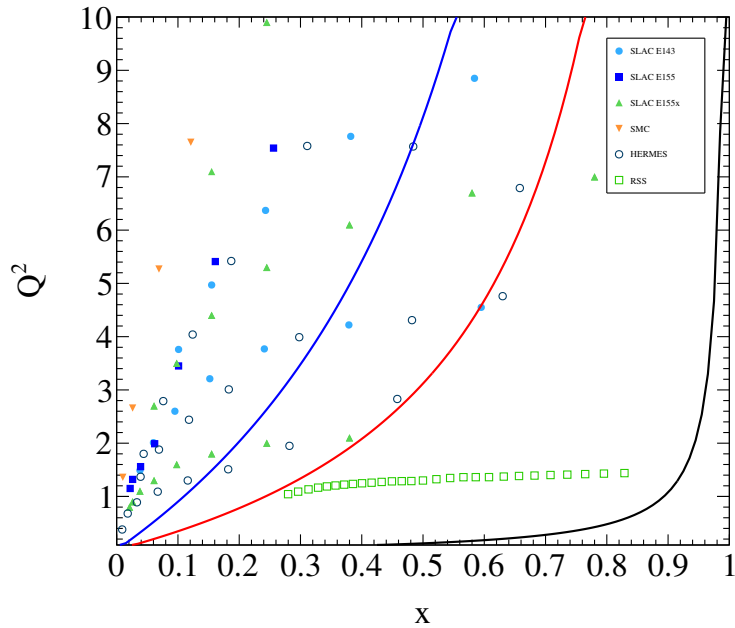


Figure 2.9.: Kinematic coverage of world data on g_2^p . Lines of constant W are shown for 1 GeV (black), 2 GeV (red), and 3 GeV (blue).

and

$$A_{\perp} = \frac{d\sigma^{\leftarrow\uparrow} - d\sigma^{\leftarrow\downarrow}}{d\sigma^{\leftarrow\uparrow} + d\sigma^{\leftarrow\downarrow}} = \frac{d\sigma^{\leftarrow\uparrow} - d\sigma^{\leftarrow\downarrow}}{2\sigma_0} \quad (2.45)$$

are often measured instead of individual cross sections. The single arrow for each cross section indicates the spin projection of the electron along the beam direction and the double arrow indicates the target polarization, which can be either parallel, \uparrow , or perpendicular, \leftarrow , to the beam direction.

These asymmetries are related to the virtual Compton scattering asymmetries through

$$A_{\parallel} = D(A_1 + \eta A_2) \quad (2.46)$$

and

$$A_{\perp} = d(A_2 - \xi A_1) \quad (2.47)$$

where the coefficients D , d , η , and ξ are given explicitly in A.1. The spin structure functions can be written in terms of these asymmetries as

$$g_1 = \frac{F_1}{1 + \gamma^2} [A_1 + \gamma A_2] \quad (2.48)$$

and

$$g_2 = \frac{F_1}{1 + \gamma^2} \left[-A_1 + \frac{1}{\gamma} A_2 \right] \quad (2.49)$$

where $\gamma^2 = Q^2/\nu^2$. Here it is clear that the unpolarized structure function is required in order to extract the spin structure functions from the measured asymmetries 2.46 and 2.47. For a more detailed discussion of the virtual Compton asymmetries see appendix A.

2.6 Parton Model

So far a physical meaning has not been attributed to the structure functions. The observed scaling behavior of F_2 leads to the interpretation that the nucleon contains point like particles which are resolved at high energies. Specifically, the scale at which the virtual photon probes the target is given by Q^2 and the length scales which it becomes sensitive to are proportional to $1/Q$ as shown in Figure 2.10.

At large distance scales the nucleon is a coherent mass that scatters elastically. At slightly smaller distance scales resonance production begins, as shown in Figure 2.3, and the virtual photon resolves the pion cloud around the nucleon. Once passing the resonance region, the virtual photon begins to scatter from the individual point-like constituents of the nucleon, called partons [17] [24]. The deep inelastic cross section is the sum of all these incoherent scattering cross sections.

The naive parton model is formally defined in the so-called Bjorken or DIS limit, where $Q^2 \rightarrow \infty$ and $\nu \rightarrow \infty$ but the scalar invariant, $x = Q^2/2M\nu$,

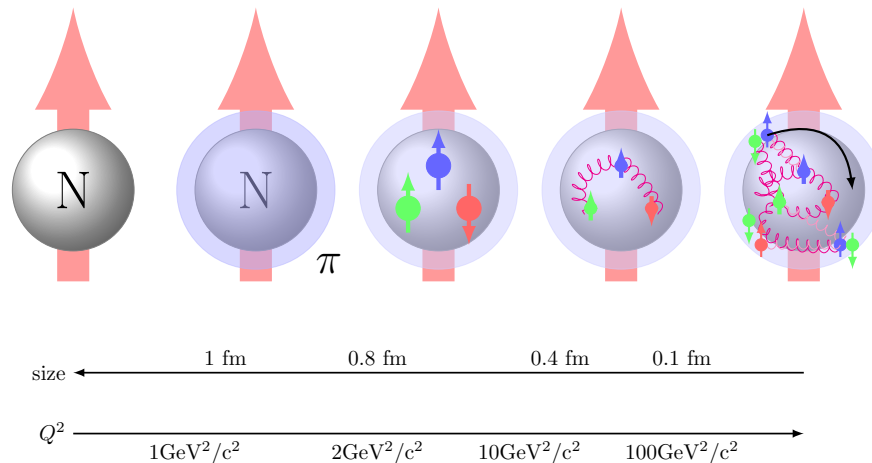


Figure 2.10.: Cartoon of the nucleon at increasing Q^2 values and smaller distance scales.

remains finite. The nucleon is in a fast moving reference such that transverse motion is suppressed causing the nucleon to appear flattened like a pancake with each parton carrying momentum xP . Here we give meaning to the Bjorken x variable; it is the fraction of the nucleon's momentum carried by the quark struck by the virtual photon. This is true only under certain approximations, namely the impulse approximation, where the scattering happens elastically a single non-interacting parton, and where the target and parton masses are small compared to Q^2 .

2.6.1 Quark PDFs and Structure Functions

The partons are the quarks and gluons bound within the nucleon. At leading order, a virtual photon only couples to quarks because the gluon does not carry any electric charge, therefore, DIS experiments are directly sensitive to just the

quark distributions. The Bjorken limit connects the parton distributions to the scaling structure functions

$$\lim_{\text{Bjorken}} F_1(x, Q^2) \longrightarrow F_1(x) = \frac{1}{2} \sum_{q=u,d,s} e_q^2 (q(x) + \bar{q}(x)) \quad (2.50)$$

where e_q is the quark electric charge and the sum is over all quark flavors. The PDFs can be interpreted as the probability, $q(x)dx$, of finding a quark with momentum fraction x in the interval $[x, x + dx]$. In this naive parton model picture, the nucleon is made of non-interacting, collinear moving quarks.

Similarly, spin structure function g_1 is related to the polarized quark PDFs through

$$\lim_{\text{Bjorken}} g_1(x, Q^2) \longrightarrow g_1(x) = \frac{1}{2} \sum_q e_q^2 \Delta q(x) \quad (2.51)$$

where Δq is the difference in the probability densities for finding a quark with its spin aligned and anti-aligned along the nucleon's spin axis. That is

$$\Delta q(x) \equiv q_{\uparrow}(x) - q_{\downarrow}(x) \quad (2.52)$$

and

$$q(x) \equiv q_{\uparrow}(x) + q_{\downarrow}(x) \quad (2.53)$$

where $q_{\uparrow/\downarrow}$ are the individual helicity distributions for quarks with spin projections aligned/opposite the nucleon spin.

A predictable consequence of quarks being spin-1/2, non-interacting, point-like particles is the Callan-Gross relation [15]. Holding only in the Bjorken limit, this relation connects the two unpolarized structure functions through

$$F_2(x) = 2xF_1(x) = \sum_q e_q^2 x (q(x) + \bar{q}(x)). \quad (2.54)$$

Conversely, the situation for the polarized structure functions differs in that there is no analogous relation among g_1 and g_2 . Within the naive parton model one arrives at the trivial result

$$g_2(x) = 0. \tag{2.55}$$

Although it evades a simple physical interpretation, g_2 provides useful information about the non-perturbative structure of the nucleon.

CHAPTER 3

THE STRUCTURE OF THE NUCLEON

The previous chapter provided the framework for measuring the nucleon structure functions and the foundations for its description in terms of parton distributions. Naturally, a connection between the partons and QCD, apart from its property of asymptotic freedom, is desirable. Before addressing the points of contact between data and theory it is worth putting the difficulties of quantum chromodynamics in perspective relative to quantum electrodynamics.

Unlike the QED coupling which gets weaker at larger distances, the QCD coupling constant becomes stronger at larger distances. In atomic physics the starting point is the hydrogen atom for which a solution to the Schrödinger equation (or Dirac equation) is known exactly. Perhaps it is obvious, but larger atoms are constructed from the ideas put forth from the smallest atom as one builds the periodic table of elements. This wonderful achievement is, in part, due to the weakness of the electromagnetic coupling at large distances and the mathematical solution it permits. Using perturbation theory, many corrections can be calculated and theoretical problems become limited only by complexity. Experimentalists can focus on measuring transitions, e.g. the Lamb shift, to test the theory at remarkable precisions.

QCD does not have a hydrogen atom analog because at large distances the coupling constant becomes large enough that the energy required to maintain the fields between a quark and anti-quark is much more than that necessary to create another quark-antiquark pair. Nature chooses to create particle pairs instead of long distance chromo-electromagnetic fields. Therefore the bound state requires an infinite number of particles since quark masses are only a very

small fraction of the nucleon (or even pion) mass. As we will see, any connection between QCD and a simple quark model description of the nucleon (not to be confused with the naive parton model), even with all the successes of the quark model, is tenuous at best.

Void of a similar starting point, QCD's property of asymptotic freedom permits a description to begin in the Bjorken limit where partons are non-interacting particles without any transverse momentum. Although this may seem limiting, it provides a theoretically sound starting point from which corrections can be applied. Therefore, when considering finite Q^2 scales, i.e. experimental Q^2 values, the transverse size is limited to $1/Q$ and corrections must be calculated which fall under the larger category of finite Q^2 corrections as shown Figure 3.1.

This chapter will introduce two important theoretical tools for calculating finite Q^2 corrections. The first is the pQCD description of the Q^2 evolution of the PDFs, connecting measurements at very different scales. The second important tool is the Operator Product Expansion (OPE). Within the OPE framework, non-perturbative effects are quantified and allow us to consistently address all the finite Q^2 that Figure 3.1 outlines. We will conclude with the primary motivation of the experiment which includes extracting non-perturbative physics and tests of lattice QCD.

3.1 Moments and Models

Early on measurements of neutron and proton structure function F_2 provided an important piece of information about the partonic composition of the nucleon, namely that gluons carry roughly half of its momentum. Using the simple quark model and neglecting strange quarks, the momentum fraction carried by the up and down quarks can be determined from the x moments as

$$\int_0^1 dx x(u + \bar{u}) = \int_0^1 dx \left[\frac{12}{5} F_2^p(x) - \frac{3}{5} F_2^n(x) \right] \simeq 0.36 \quad (3.1)$$

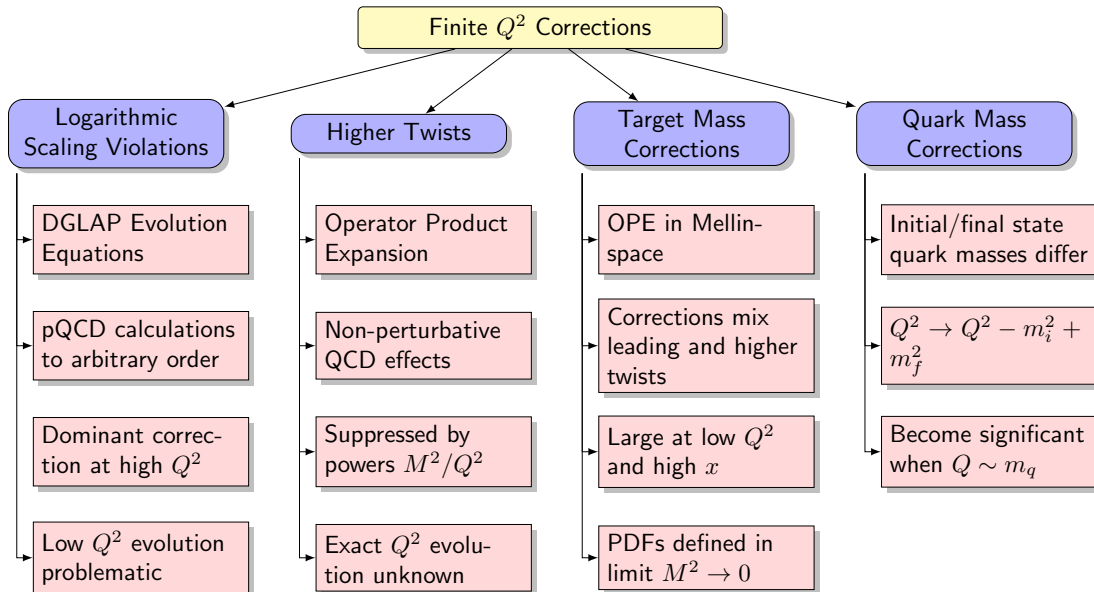


Figure 3.1.: A chart outlining the various finite Q^2 corrections.

and

$$\int_0^1 dx x(d + \bar{d}) = \int_0^1 dx \left[\frac{12}{5} F_2^n(x) - \frac{3}{5} F_2^p(x) \right] \simeq 0.18. \quad (3.2)$$

This result may seem surprising at first, but considering the quark masses relative to the nucleon mass, a large amount of quark pairs need to be created from gluons. This is the difference between the nearly massless *current quarks* of QCD, and the massive *constituent quarks* of the quark model. Quite naturally, the description must move from the simple quark model to the naive parton model (see section 2.6) in order to include gluons carrying a significant amount the nucleon momentum.

3.1.1 Ellis-Jaffe Sum Rule

As first noted by Alvarez and Block [3] (see section 1.1), “other causes” were responsible for the sizeable magnetic moments of the proton and neutron. The causes are now known to be the strongly interacting quark and gluon fields. The

quark model predicts the ratio $\mu_n/\mu_p = -2/3$, which is very close to the actual value of -0.68 . This seemingly nice result leads to the conclusion that the spin of the nucleon is due to the sum of all the quark spins. Ellis and Jaffe [25] originally derived their sum rule to test the quark spin content of the nucleon. It is

$$\Gamma_1 = \int_0^1 dx g_1(x) = \frac{1}{9}\Delta\Sigma \pm \frac{1}{12}a_3 + \frac{1}{36}a_8 \quad (3.3)$$

where the \pm indicates proton or neutron, and we have introduced the moments of the flavor singlet distribution

$$\Delta\Sigma = \int_0^1 dx \Delta\Sigma(x) , \quad (3.4)$$

along with the non-singlet distributions

$$a_{3,8} = \int_0^1 dx \Delta q_{3,8}(x). \quad (3.5)$$

Noting that the values of a_3 and a_8 are known from studying β -decays (section 3.2.2) and that the quark spin contribution to the nucleon spin is $S_z^q = \Delta\Sigma/2$, a measurement of Γ_1 provides a direct determination of the quark spin contribution to the total nucleon spin.

Results from the EMC experiment [26] showed Γ_1 was about half of what was expected, an apparent violation of the sum rule. This was the beginning of the “proton spin crisis” [27], because it turned out that the quarks only carried a small fraction of the nucleon spin.

In hindsight, calling this a *crisis* seems a bit hyperbolic considering the degree to which we do not understand the non-perturbative structure of QCD. Furthermore, this was a result of the simple quark model, which already failed to describe the gluon distribution (since there are no gluons in the simple quark model). Again, like the momentum fraction carried by quarks, there is still the contribution from the gluon helicity distribution to the nucleon spin. Furthermore,

the orbital motion of the partons was neglected. Orbital angular momentum is considered to play an important role and is an active area of reasearch.

3.1.2 Bjorken Sum Rule

Taking the difference between the proton and neutron moments yields an important test of the non-singlet part of Γ_1 . In his original paper [28] Bjorken derives his sum rule [29]

$$\Gamma_1^{p-n} = \Gamma_1^p - \Gamma_1^n = \int_0^1 dx (g_1^p(x, Q^2) - g_1^n(x, Q^2)) = \frac{g_A}{6} \quad (3.6)$$

where g_A is the nucleon isovector axial coupling constant. Experimental results conclude that the sum rule holds to about 10%. This result provides the important clue: the problem with the nucleon spin is connected to the singlet distribution.

In summary the gluon distributions and parton orbital motion play an undeniably important role in the structure of the nucleon. We will see in the next section that including the gluon distribution and other QCD effects leads to a fantastic description of the data.

3.2 Scaling Violations

The Bjorken limit is a theoretical nicety, but experimentally impossible. Every experiment occurs at a finite value of Q^2 . The connection between the parton model and experiments in the DIS kinematic region comes in the form of (radiative) corrections calculated using pQCD. These corrections are often referred to as *logarithmic scaling violations*.

3.2.1 QCD Improved Parton Model

At a large but constant value of Q^2 the parton distribution functions can be extracted by fitting DIS data, however, it is experimentally difficult to cover all of Bjorken x ($0 < x < 1$) for a fixed value of Q^2 . For example, this can be seen in the kinematic coverage for each experiment shown in Figure 2.8.

Fortunately, within the so-called *QCD improved parton model*, the evolution of the (leading twist) PDFs from the input scale, Q_0^2 , to the experimental scale, Q^2 , can be calculated from the well known DGLAP evolution equations. Therefore, data from a wide range of x and Q^2 can be simultaneously fit yielding one set of PDFs.

Conversely, as a test of pQCD one data set, say, at large Q^2 , can be fit and evolved to the scale of another data set at lower Q^2 . This has been one of the great achievements of pQCD: it can describe the data over a wide range of scales.

3.2.2 DGLAP Evolution Equations

The DGLAP [30–32] equations follow from perturbative QCD calculations that can be performed to arbitrary order in the coupling constant. The pQCD input comes in the form of splitting functions, which in the case of $P_{qq}(z)$, describes the probability of a quark emitting a gluon and reducing its momentum by a fraction z [33].

Qualitatively the DGLAP equations describe how the make up of the nucleon, contained in the PDFs, changes from the input scale (Q_0^2) to another. Thus it can predict what a photon “sees” at various Q^2 (see Figure 2.10). The leading order diagram for quark is shown in Figure 3.2 and some perturbative corrections to this are diagram are on the right. If these terms are included then all other possible terms at the same order in α_s should be included as well. As illustrated in Figure 3.3, these terms couple the quark and gluon parton distributions because

a photon can now be absorbed by a quark that originated from the distribution of gluons.

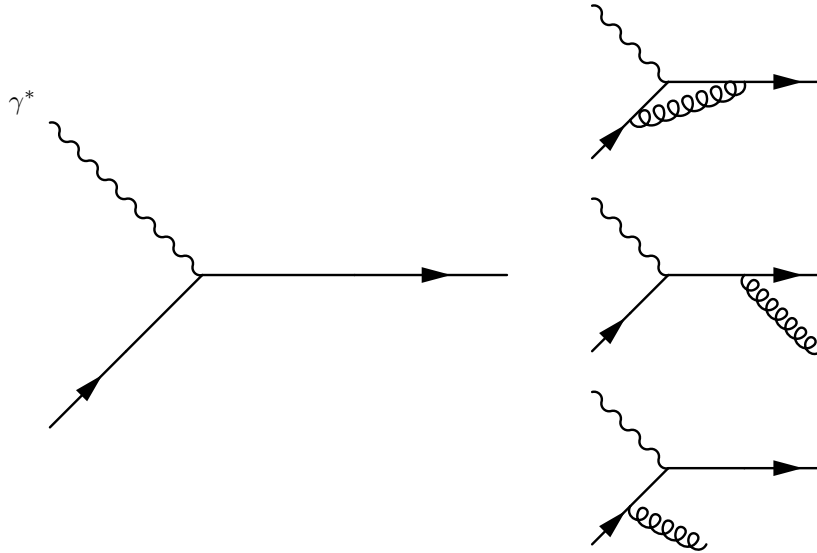


Figure 3.2.: An example diagrams contributing to the leading order calculation of P_{qq} .

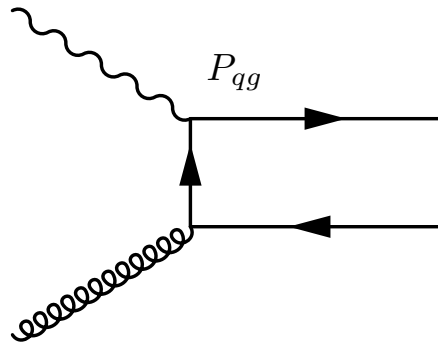


Figure 3.3.: Lead order contribution to the splitting function P_{qg} . This illustrates the coupling of the quark and gluon PDFs.

The unpolarized flavor singlet distribution is

$$\Sigma(x) = u(x) + \bar{u}(x) + d(x) + \bar{d}(x) + s(x) + \bar{s}(x) \quad (3.7)$$

and it evolves coupled to the gluon distribution, $g(x)$. Similarly, the polarized singlet distribution is

$$\Delta\Sigma(x) = \Delta u(x) + \Delta\bar{u}(x) + \Delta d(x) + \Delta\bar{d}(x) + \Delta s(x) + \Delta\bar{s}(x) \quad (3.8)$$

and evolves coupled to the polarized gluon distribution $\Delta g(x)$. The non-singlet distributions are defined as

$$q_3(x) = (u(x) + \bar{u}(x)) - (d(x) + \bar{d}(x)) \quad (3.9)$$

$$q_8(x) = (u(x) + \bar{u}(x)) + (d(x) + \bar{d}(x)) - 2(s(x) + \bar{s}(x)) \quad (3.10)$$

$$\Delta q_3(x) = (\Delta u(x) + \Delta\bar{u}(x)) - (\Delta d(x) + \Delta\bar{d}(x)) \quad (3.11)$$

$$\Delta q_8(x) = (\Delta u(x) + \Delta\bar{u}(x)) + (\Delta d(x) + \Delta\bar{d}(x)) - 2(\Delta s(x) + \Delta\bar{s}(x)) \quad (3.12)$$

where we have considered only three quark flavors.

The singlet evolution equation written in matrix form is

$$\frac{d}{d\ln Q^2} \begin{pmatrix} \Sigma(x, Q^2) \\ g(x, Q^2) \end{pmatrix} = \frac{\alpha_s}{2\pi} \begin{pmatrix} P_{qq} & P_{qg} \\ P_{gq} & P_{gg} \end{pmatrix} \otimes \begin{pmatrix} \Sigma(x, Q^2) \\ g(x, Q^2) \end{pmatrix} \quad (3.13)$$

where the convolution integral is defined as

$$P \otimes f = \int_x^1 \frac{dy}{y} f(y) P\left(\frac{x}{y}\right). \quad (3.14)$$

The non-singlet distributions evolve independent of the gluon distribution according to

$$\frac{d}{d\ln Q^2} q_{ns}(x, Q^2) = \frac{\alpha_s}{2\pi} P_{ns} \otimes q_{ns}. \quad (3.15)$$

Similar evolution equations exist for the polarized singlet and gluon distributions

$$\frac{d}{d\ln Q^2} \begin{pmatrix} \Delta\Sigma(x, Q^2) \\ \Delta g(x, Q^2) \end{pmatrix} = \frac{\alpha_s}{2\pi} \begin{pmatrix} \Delta P_{qq} & \Delta P_{qg} \\ \Delta P_{gq} & \Delta P_{gg} \end{pmatrix} \otimes \begin{pmatrix} \Delta\Sigma(x, Q^2) \\ \Delta g(x, Q^2) \end{pmatrix} \quad (3.16)$$

and for the polarized non-singlet distributions

$$\frac{d}{d\ln Q^2} \Delta q_{ns}(x, Q^2) = \frac{\alpha_s}{2\pi} \Delta P_{ns} \otimes \Delta q_{ns} . \quad (3.17)$$

The moments the non-singlet distributions, a_3 and a_8 , can be determined from studying hyperon β -decays. Additionally from isospin invariance $a_3 = g_A$, where the g_A is the usual axial vector coupling found in neutron β -decays. These provide some constraints on the polarized distributions analogous to the flavor conservation constraints on the unpolarized distributions.

The meaning of each splitting function can be understood from Figure 3.4, which illustrates that because the photon only couples to quarks, deep inelastic electron scattering is only sensitive to the upper two diagrams. Ideally, a virtual gluon probe, analogous to the virtual photon, would allow for a clean measurement of the gluon distributions but it does not exist due to confinement. Instead the Drell-Yan process (e.g. proton-proton collisions) can be used, in a limited fashion, to probe the gluon distributions. Calculations of splitting functions can be found in [34] and references therein.

3.2.3 PDFs

For nearly 30 years, experiments have extracted the PDFs from process that include DIS, Drell-Yan, and SIDIS. The parton distributions are the same in all processes and are therefore seen as universal. Figure 3.5 is one example of how the DGLAP equations succeed at describing the data over a wide of scales, but

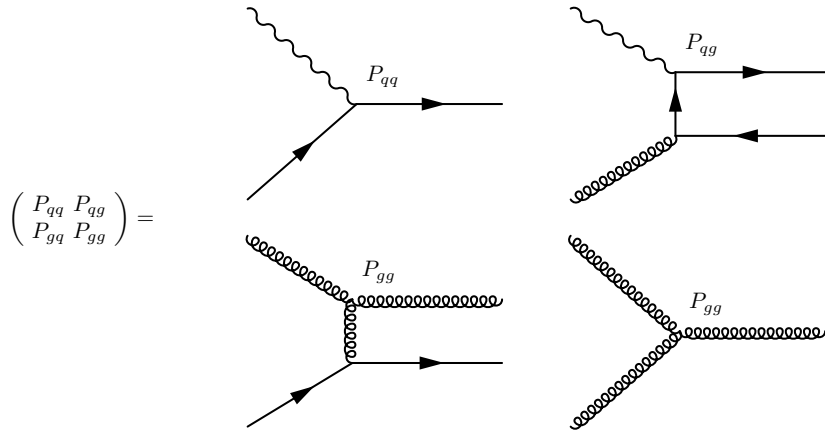


Figure 3.4.: Graphical representation of P_{ij} .

it is important to remember that these scales are all “small” distance scales, i.e., $Q^2 \gg 1 \text{ GeV}^2$.

The PDFs encapsulate the non-perturbative information contained only in the picture of the nucleon where the partons can be considered approximately non-interacting. They fail to include the many body, strongly correlated, non-perturbative picture that dominates at large distance scales, i.e., $Q^2 < 1 \text{ GeV}^2$.

3.3 Operator Product Expansion

The DGLAP equations are a wonderful result from QCD and are useful for extracting the PDFs from the data. But in order to test our knowledge in the non-perturbative regime, or lack there of, we can use the operator product expansion to isolate these effects. The goal of OPE is to turn a non-local operator into a sum of local operators. For example, consider the time ordered product

$$T[A(0)B(x)] \simeq \sum_i c_i(x) \mathcal{O}_i(0) . \quad (3.18)$$

where A and B are explicitly non-local operators which are then expanded in terms involving the Wilson coefficient functions, c_i , and local operators \mathcal{O} .

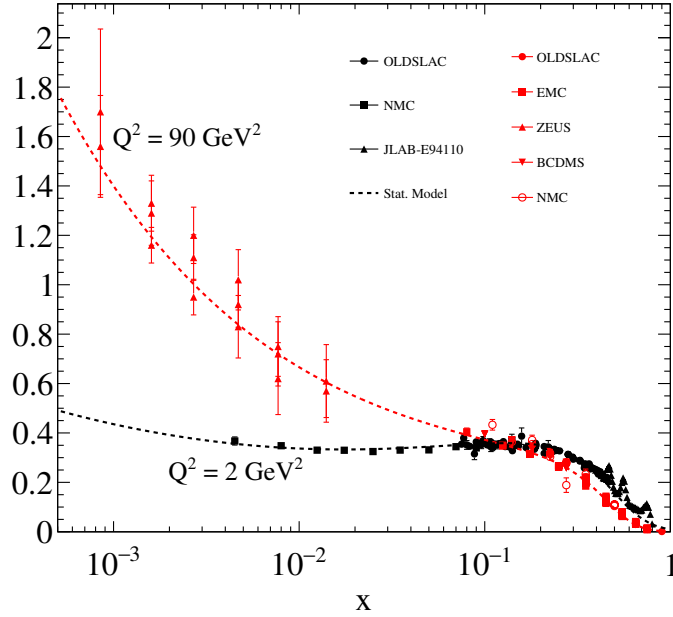


Figure 3.5.: Data on the structure function F_2^p along with the result calculated from an evolved fit [35]. The fit is calculated at the mean value of Q^2 for the selected data around $Q^2 = 2 \text{ GeV}^2$ (black) and $Q^2 = 90 \text{ GeV}^2$ (red).

The spin structure functions are related to the time ordered product appearing in the forward part of the virtual Compton amplitude (see Appendix A). The operators required in this expansion are characterized by isospin and twist. The leading twist ($\tau = 2$) operators are related to the parton distribution functions and their coefficient functions are directly related to the splitting functions of the DGLAP equations. For more details on the OPE see appendix B.

Revisiting the Ellis-Jaffe sum rule, and including the leading twist pQCD corrections [36], it now has the form

$$\int_0^1 dx g_1^p(x, Q^2) = C_{ns}(Q^2) \left(\pm \frac{1}{12} g_3(Q^2) + \frac{1}{36} a_8(Q^2) \right) + C_s(Q^2) \frac{1}{9} \Delta\Sigma(Q^2) + \text{HT} \quad (3.19)$$

where C_{ns} and C_s are the non-singlet and the singlet coefficient functions respectively. The HT represents the higher twist contributions to first moment of

g_1 . Note that there is now an explicit Q^2 dependence in the moments of the distributions implying a dependence on the gluon distribution.

3.3.1 Higher Twists

At large values of Q^2 non-perturbative effects contribute but their size is negligible. At lower Q^2 their contribution becomes important. These show up as corrections proportional to $(1/Q^2)^n$ and involve quark-gluon correlations that cannot be obtained in the naive parton model.

These non-perturbative corrections, referred to as higher twist or power corrections, can be carefully extracted from experiment using the operator product expansion beyond the leading-twist approximation. Often they can also be calculated from phenomenological models or Lattice QCD. Comparisons of higher twist corrections against Lattice QCD predictions provide fundamental tests of non-perturbative QCD.

Within the so-called *twist expansion* the moment has the form

$$\Gamma_1(Q^2) = \int_0^1 dx g_1(x, Q^2) = \mu_2(Q^2) + \frac{\mu_4(Q^2)}{Q^2} + \frac{\mu_6(Q^2)}{Q^4} + \dots \quad (3.20)$$

where the leading twist term

$$\mu_2^{p,n} = C_{ns}(Q^2) \left(\pm \frac{1}{12} g_A + \frac{1}{36} a_8 \right) + C_s(Q^2) \frac{1}{9} \Delta\Sigma \quad (3.21)$$

is just the sum rule in 3.19. The Q^2 of μ_2 is well understood and measured.

However, the higher twist contribution and their Q^2 dependence is not well understood or measured. It is clear from the twist expansion that at large Q^2 the higher twist terms are suppressed. As experiments probe larger distances there remains an important question to answer: At what scale do the higher twist terms become important?

At this point it is worth introducing the explicit notation for the twist decomposition of the spin structure functions

$$\begin{aligned} g_1^{exp}(x, Q^2) &= g_1^{\tau=2}(x, Q^2) + g_1^{\tau=3}(x, Q^2) + \dots \\ g_2^{exp}(x, Q^2) &= g_2^{\tau=2}(x, Q^2) + g_2^{\tau=3}(x, Q^2) + \dots \end{aligned} \quad (3.22)$$

where the $g_1^{\tau=2}$ should be substituted into 3.19 when neglecting the higher twist terms.

It should be emphasized that the PDFs measured in deep inelastic scattering only contribute to the leading twist part of the structure functions, and that at lower Q^2 , where the precise onset of higher twists is unknown, extraction of the leading twist alone can be problematic. That is, one should be careful not to mix higher twists with renormalization scale effects.

3.3.2 Moments

From the OPE an infinite set of sum rules relating the proton matrix elements to the x moments of the structure functions. Neglecting quark mass and target mass effects the reduced matrix elements (defined in Appendix B) can be calculated from moments of g_1 and g_2 ,

$$\int_0^1 dx x^{n-1} g_1(x, Q^2) = \frac{1}{2} \tilde{a}_{n-1}(Q^2) \quad n = 1, 3, 5 \dots \quad (3.23)$$

and

$$\int_0^1 dx x^{n-1} g_2(x, Q^2) = \frac{n-1}{2n} \left(\tilde{d}_{n-1}(Q^2) - \tilde{a}_{n-1}(Q^2) \right) \quad n = 3, 5, 7 \dots \quad (3.24)$$

where \tilde{a}_{n-1} are twist-2 and \tilde{d}_{n-1} are twist-3 reduced matrix elements. Noting that 3.24 starts at $n = 1$, the OPE does not predict the Burkhardt-Cottingham sum rule [37]

$$\int_0^1 dx g_2(x, Q^2) = 0. \quad (3.25)$$

Experimentally the sum rule seems to hold but the data is not precise enough at low x to very well constrain the result. It is interesting that should if equation 3.24 holds for $n = 1$ it would reduce to the BC sum rule.

Wandzura-Wilczek Relation

Perhaps the closest analog to the Callan-Gross relation for the spin structure functions comes from the leading twist approximation of the moments in equations 3.23 and 3.24 for $n = 3$. The Wandzura-Wilczek relation [38],

$$g_2^{WW}(x) \equiv g_2^{\tau=2}(x) = -g_1^{\tau=2}(x) + \int_x^1 \frac{dy}{y} g_1^{\tau=2}(y) \quad (3.26)$$

relates the leading twist part of g_1 to the leading twist part of g_2 . If the twist-3 contribution is included, the structure function g_2 has an additional term

$$g_2(x) = g_2^{WW}(x) + \bar{g}_2(x) \quad (3.27)$$

where the higher twist part is

$$\int_0^1 dx x^{n-1} \bar{g}_{n-1}(x) = \frac{n-1}{2n} \tilde{d}_{n-1}(Q^2) \quad n = 3, 5, 7 \dots \quad (3.28)$$

Blumlein-Tkabladze Relation

When considering target mass effects a relation [39] between the twist-3 part of g_2 shows up in g_1 as the target mass correction

$$g_1^{\tau=3}(x) = \frac{4M^2x^2}{Q^2} \left[g_2^{\tau=3}(x) - 2 \int_x^1 \frac{dy}{y} g_2^{\tau=3}(y) \right]. \quad (3.29)$$

As will soon be discussed, this target mass correction is responsible for the next-to-leading appearance of d_2 in the twist expansion of Γ_1 . This relation is as important to consider as the Wandzura-Wilczek relation when trying to extract higher twist decomposition of g_2 . A simultaneous separation of higher twists from both g_1 and g_2 would be the ideal method in order to avoid including spurious twist-3 contributions in g_2^{WW} by neglecting equation 3.29. It has been demonstrated [40] that making this mistake for the proton may end up causing a sinister cancellation of $g_2^{\tau=3}$.

3.4 Color Forces

The ground work laid out by the OPE allows for the extraction of interesting physics from precision measurements of the spin structure functions. A measurement of the g_2 structure function is directly sensitive to quark gluon correlations as shown in Figure 3.6b. In particular, the twist-3 matrix element can be extract from the data via

$$\tilde{d}_2(Q^2) = \int_0^1 dx x^2 (2g_1(x) + 3g_2(x)). \quad (3.30)$$

At large Q^2 where the d_2 is proportional to an average transverse color Lorentz force acting on the struck quark the instant after being struck by the virtual photon [18, 41]. This can be easily seen by explicitly writing the matrix element

$$\tilde{d}_2 = \frac{1}{2MP^{+2}S_x} \langle P, S | \bar{q}(0) g G^{+y}(0) \gamma^+ q(0) | P, S \rangle. \quad (3.31)$$

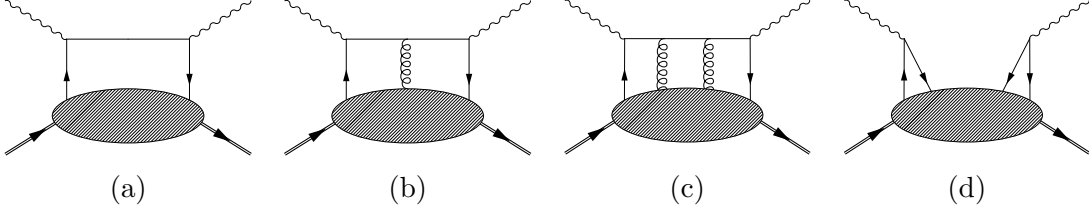


Figure 3.6.: Diagrams for operators in the twist expansion.

Exploiting the fact that the proton is moving in the infinite momentum frame, i.e., $\vec{v} = -c\hat{z}$, the field strength tensor becomes

$$\left[\vec{E} + \vec{v} \times \vec{B}\right]^y = E^y + B^x = \sqrt{2}G^{+y} \quad (3.32)$$

and

$$\begin{aligned} F^y &= -\frac{\sqrt{2}}{2P^+} \langle P, S | \bar{q}(0) G^{+y}(0) \gamma^+ q(0) | P, S \rangle \\ &= -2\sqrt{2} M P^+ S^x d_2 \\ &= -2M^2 d_2 \end{aligned} \quad (3.33)$$

It should be emphasized here that a measurement of g_2 is *directly* sensitive to an average color Lorentz force. This puts polarized DIS in an entirely unique situation to begin precision measurements in QCD.

Furthermore, when considering higher twist matrix elements Burkardt [18] showed that the color electric and magnetic forces can be separated by

$$F_E = \frac{-M^2}{4} \left[\frac{2}{3}(2\tilde{d}_2 + \tilde{f}_2) \right] \quad (3.34)$$

$$F_B = \frac{-M^2}{2} \left[\frac{1}{3}(4\tilde{d}_2 - \tilde{f}_2) \right]. \quad (3.35)$$

The twist-4 matrix element is defined as

$$\tilde{f}_2 M^2 S^\mu = \frac{1}{2} \sum_i e_i^2 \langle P, S | g \bar{\psi}_i \tilde{G}^{\mu\nu} \gamma_\nu \psi_i | P, S \rangle$$

and it can be extracted from the first moment of g_1 . The next-to-leading twist contribution to Γ_1 is written in terms of the reduced matrix elements [42]

$$\mu_4 = \frac{M^2}{9} \left(\tilde{a}_2 + 4\tilde{d}_2 + 4\tilde{f}_2 \right), \quad (3.36)$$

where \tilde{a}_2 is twist-2, \tilde{d}_2 is twist-3, and \tilde{f}_2 is twist-4. Since μ_4 does not enter at leading twist it must be determined by subtracting the, presumably well known, leading twist

$$\Delta\Gamma_1 = \Gamma_1 - \mu_2 \quad (3.37)$$

where the $\Delta\Gamma_1$ contains *all* higher twists. Therefore it should be clear that a clean determination of \tilde{f}_2 would require precision data taken at high Q^2 in order to make sure all higher twists are suppressed. Then by moving to lower Q^2 the with matched precision in \tilde{d}_2 and \tilde{a}_2 the difference can be attributed to \tilde{f}_2 or even higher twists. Before this can be done, however, the leading twist terms must be well determined by precision measurements at low x , where the integral of the first moment dominates, and large momentum transfers to ensure the absence of higher twists.

3.4.1 Status of d_2

So far there have only been two measurements of \tilde{d}_2^p , although the first is really an improved value by combining the results of SLAC E143, E155, and E155x [43]. This result is at an average Q^2 of 5 GeV². The second measurement was done by Resonance Spin Structure (RSS) experiment [44,45] which extracted a value \tilde{d}_2^p value at $Q^2 = 1.28$ GeV². These two results are shown in Figure 3.7 along with a lattice QCD calculation [46].

The elastic contribution to the integral at $x = 1$ can be calculated using equations 2.34 – 2.37 and fits to the elastic form factors. Interestingly, when

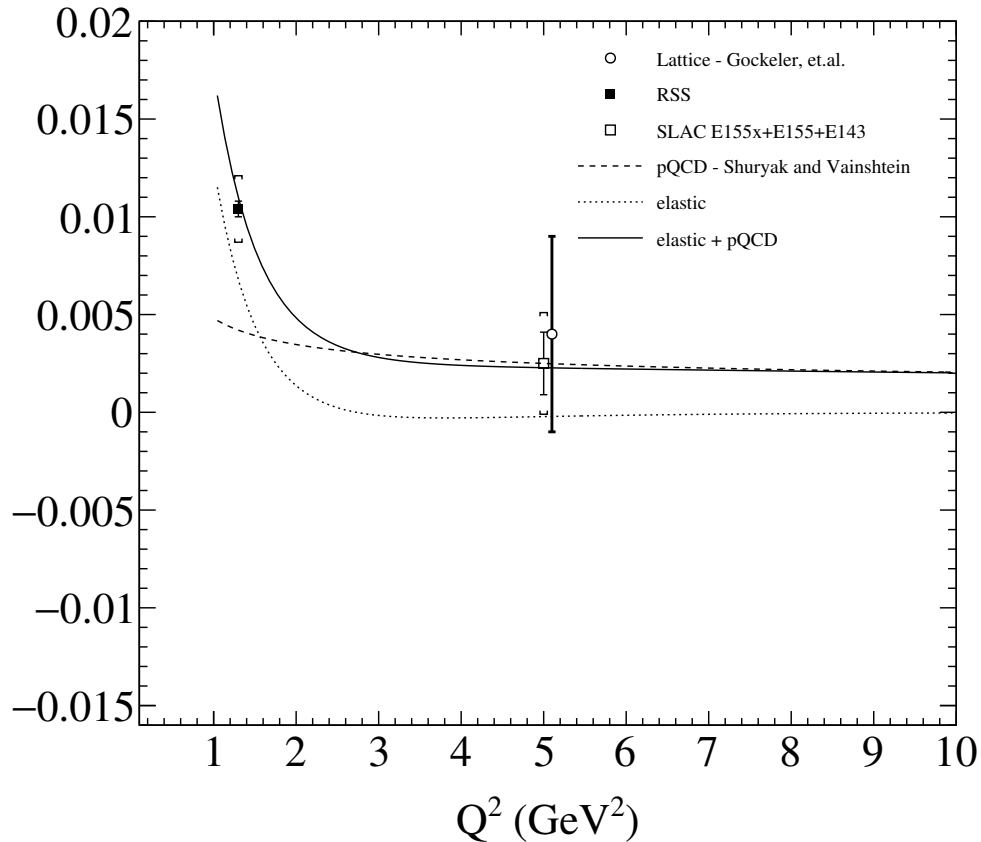


Figure 3.7.: The world data on \tilde{d}_2^p from SLAC [43] (open square) and RSS [45] (filled square), and a lattice QCD calculation [46] (open circle).

form factors that include a two photon exchange correction are used, the elastic contribution becomes slight negative around $Q^2 \sim 3 \text{ GeV}^2$.

3.5 Remarks

With the twist 3 matrix element and its physical interpretation, QCD is beginning to enter the realm of tests through precision experiments. Confinement does not permit us to measure color moments in the same way precision magnetic dipole moments are measured in QED. However, a d_2 measurement is an important step in moving our understanding of strong force into the precision

era. Just because it is small does not mean it is not important, e.g., the Lamb shift was instrumental in the development of QED. A precision measurement of d_2 hopes to spur the development of ab initio QCD calculations.

CHAPTER 4

THE EXPERIMENT

The Spin Asymmetries of the Nucleon Experiment (E03-007) finished taking data in March 2009 and the experiment took place in Hall C at Jefferson Lab. Utilizing a polarized electron beam and a polarized proton target, two double spin asymmetries were measured. The measured asymmetries are A_{180} and A_{80} , where the 180 (80) refers to α , the angle between the incoming beam and the target polarization vector (see Figure 2.7). A large solid angle and momentum acceptance detector package, the Big Electron Telescope Array (BETA), detected scattered electrons in an open configuration at a scattering angle of 40 degrees.

The kinematic coverage of BETA is shown in Figure. 4.1. Although BETA was fixed at 40 degrees, a large solid angle of about 200 mSr and large momentum acceptance allowed for kinematics covering $0.3 < x < 0.8$ and $2.0 \text{ GeV}^2 < Q^2 < 6.5 \text{ GeV}^2$. The experiment used two beam energies, 4.7 GeV and 5.9 GeV.

We will begin this chapter by describing the accelerator and polarized electron beam. The polarized target will be discussed in section 4.2, followed by an overview of BETA in section 4.3.

4.1 Accelerator and Beamline

The Thomas Jefferson National Accelerator Facility operated a longitudinally polarized electron beam capable of energies up to 6 GeV . The continuous electron beam accelerator facility (CEBAF), constructed in a “racetrack” configuration, accelerates injected electrons along the straight sections. These straight sections consist of multiple superconducting RF cavities through which electrons make multiple passes, increasing the energy with each pass.

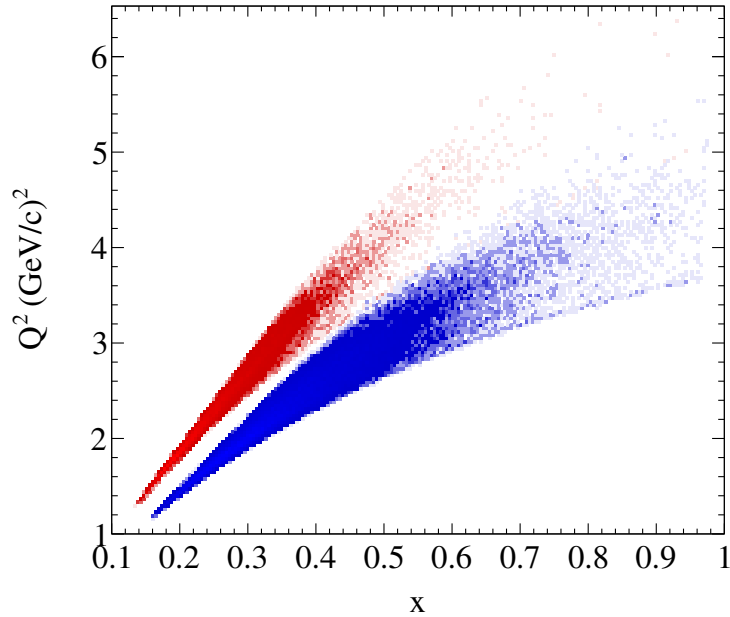


Figure 4.1.: Kinematic coverage of BETA for the two beam energies, 4.7 GeV (blue) and 5.9 GeV (red).

The polarized electron source begins with a cathode of strained GaAs. Alternating circularly polarized light is produced by a Pockel Cell which operates at a frequency of about 30 Hz. The laser light ejects polarized electrons from the cathode because the material is prepared, or strained, in order to lift the degeneracies that hamper high polarizations. Details of the injection system, design and operation can be found in [47], [48], [49].

CEBAF is able to simultaneously provide beam to all three experimental halls. However, the polarization at each hall is different and is dependent on the number of passes (due to Larmor precession in the magnetic fields) and the Wien filter angle used at the injector. Therefore, each hall measures the incoming electron beam polarization independently.

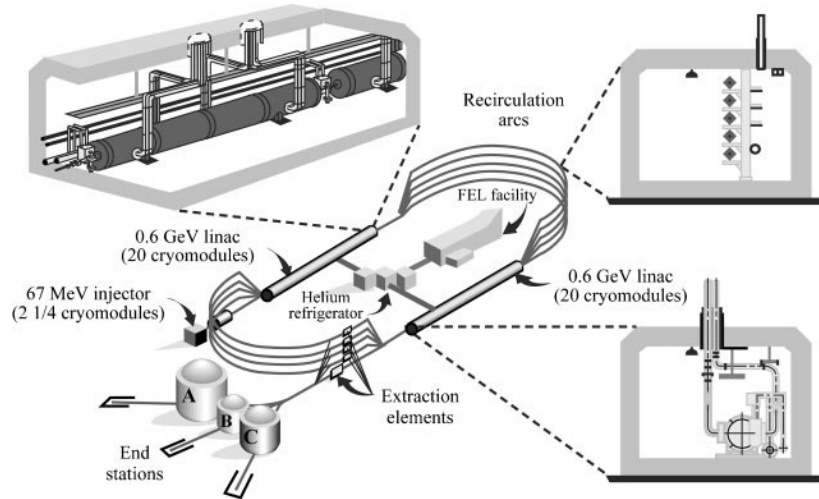


Figure 4.2.: Overview of CEBAF reproduced from [47]

4.1.1 Hall C Beamline

Beam Energy Measurement

The beam energy is determined by measuring the position of the beam after going through the well known arc magnets. The position is determined by using superharps [50], which is a destructive measurement that scans the beam profile with wires. The superharps can determine the position with a resolution of roughly $10 \mu\text{m}$ at the entrance, midpoint, and exit of the arc [51]. The beam energy is then calculated as

$$E \simeq \frac{e}{\theta} \int B dl \quad (4.1)$$

where e is the electron charge, θ is the bend angle after traveling through the arc, and the line integral is over the trajectory through the arc magnets with known magnetic field B . As part of the Hall C standard beamline for more than a decade [52], an accurate determination of the beam energy can be deduced from the arc magnet current settings. These beam energies are shown Figure 4.3 for each run.

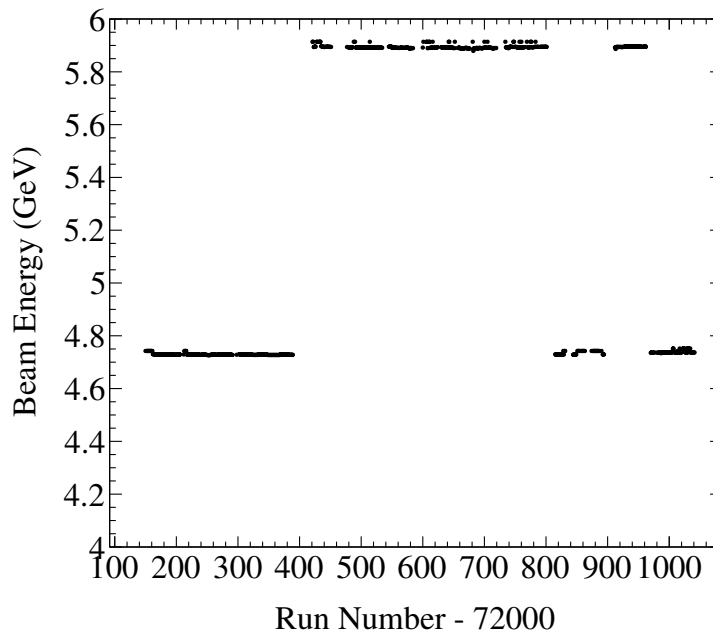


Figure 4.3.: Beam energies vs run number showing two beam energies, 4.7 GeV and 5.9 GeV.

Polarimeter

The Hall-C Møller polarimeter was used to measure the beam polarization during the SANE to precision of less than a percent [53]. A disruptive measurement, the Møller polarimeter measured the polarization a few times throughout the experiment. The polarimeter consists of an iron target in a 4T magnetic field, which predictably polarizes the target's electrons. The scattering asymmetry determines the beam polarization by using the Møller cross section equation

$$\frac{d\sigma}{d\Omega} = \left(\frac{d\sigma_0}{d\Omega} \right) [1 + P_b P_t A_{zz}(\theta)] \quad (4.2)$$

where $\left(\frac{d\sigma_0}{d\Omega} \right)$ is the unpolarized Møller cross section, P_b is the beam polarization, P_t is the target electron polarization, and A_{zz} is the so-called analyzing power, which is a known function of the center of mass angle θ .

An effective electron target polarization of about 8% is achieved using a pure iron target. The iron target sat upstream a few meters from a focusing quadrupole, which is then followed by a collimation system which can be seen in Figure 4.4. A defocussing quadrupole follows the collimator. A symmetric pair of detectors consisting of a hodoscope and lead glass calorimeter measure the coincident pair, a scattered electron and recoiling target electron.

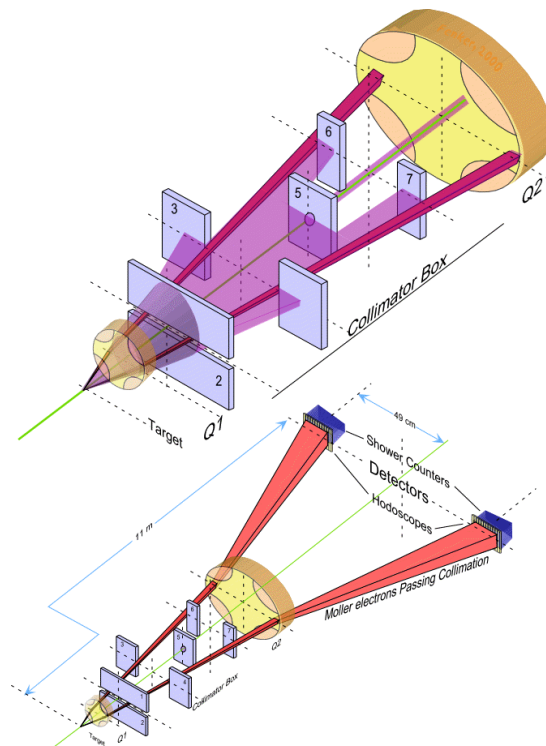


Figure 4.4.: Layout of the hall-C Møller polarimeter. The top figure shows a close up view of the collimation system and the bottom shows a larger view including the quadrupole magnet and electron detectors.

Beam Position Monitors

Two beam position monitors (BPM) were used to determine electron beam position at locations upstream in the alcove and arc sections of the beamline. Each BPM consists of a resonant cavity designed to match the accelerator beam

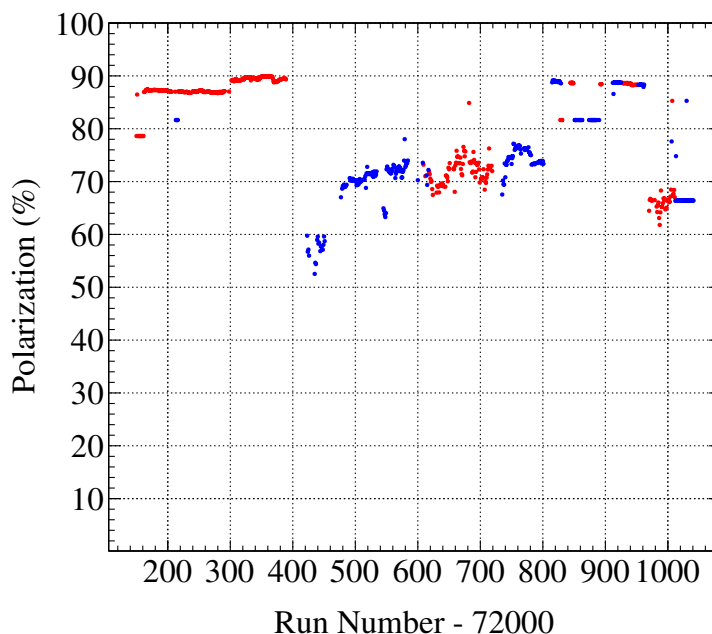


Figure 4.5.: Beam polarization vs run for the two helicities, positive (red) and negative (blue).

pulse frequency at 1497 MHz, along with four antennae around the beam. These antennae are rotated 45° so that they are not damaged by synchrotron radiation from the horizontal steering magnets. By measuring the phase locked signal difference between opposite antennae, the relative position of the beam can be determined.

Chicane and Helium Bag

A large magnetic field was required to operate the polarized target (see section 4.2). For the longitudinal target polarizations this does not pose any additional problems, however, for the transverse target configuration there was significant beam deflection. An uncompensated beam therefore would not arrive centered on the target. A chicane consisting of two dipoles was installed to posi-

tion the beam so that it arrives centered on the target with the same incidence as the longitudinal target configuration.

Since a majority of the beam does not scatter or barely scatters at very small angles and momentum transfers, the standard Hall C beam dump pipe needed to be modified as well to accommodate the transverse field deflection. Just after the target a large helium bag was installed with an extension arm to reach the target vacuum chamber. This was needed to avoid activating the existing beam pipe and limit contamination in the hall.

Beam Current Monitors

Two specially selected beam current monitors (BCMs) were used for the experiment due to the relatively low beam current required for operating the polarized target. These monitors were constructed from cylindrical resonant cavities that matched the beam frequency in a non-destructive resonance mode. The BCMs were calibrated against Faraday cup current measurements done at the injector. The BCM outputs were fed to a voltage-to-frequency converter which was then recorded by a scaler. Additionally, each BCM had a pair of helicity gated scalers which only counted when the electron beam was of a given helicity. These signals are determined by the sign of the voltage applied to the Pockel cells at the accelerator injector.

Beam Raster

The beam is typically delivered with a spread on the order of $100 \mu\text{m}$. This very small size can induce local heating damage on the various windows and targets of the beamline. Therefore, a fast raster system, consisting of two magnets far upstream spreads the beam to an area of $2 \times 2 \text{ mm}^2$ [54]. The voltages across these magnets were fed into the event data stream as ADC channels. These provided access to the raster beam position event by event.

Similarly, the polarized ammonia target is currently limited and can experience large depolarizations due to the beam. In order to increase the running luminosity, a slow raster was developed [55]. Unlike the fast raster, it rotated the beam inward in a spiral pattern of 1 cm maximum radius, with a 30 Hz repetition rate, matching both the beam pipe and target cell geometries. A diameter of roughly 2 cm reduced the local heating load on the polarized target and allowed for operation with beam currents near 100 nA.

4.2 Polarized Target

The experiment used polarized ammonia (NH_3) as an effective polarized proton target. It was operated by the University of Virginia target group. The target consisted of a superconducting magnet which produced a 5.1 T magnetic field for polarizing the target material which is cooled to roughly 1K. Through the technique of dynamic nuclear polarization (DNP) the target is capable of achieving polarizations upwards of 90%, however, due to beam depolarization effects, the average polarization for this experiment was roughly 68%. The target polarization for each run is shown in Figure 4.6.

Early on in the experiment the target magnet experienced a series of destructive quenches requiring serious repair [56]. The magnet troubles caused major delay in experimental run time and severely limited the detector commissioning and calibration periods. Thanks to the efforts of the Hall C technicians and target group the magnet was able to be repaired enough to finish the experiment.

The basic polarization mechanism is as follows. The strong magnetic field causes a Zeeman splitting of the electronic (EPR) and nuclear (NMR) spins leaving four possible configurations of the electron-proton spins. A spin-spin interaction between the electron and proton spins allows for one of the double spin flip transitions to be driven by saturating the target with microwaves. Then by exploiting the roughly 4 orders of magnitude larger relaxation time of the

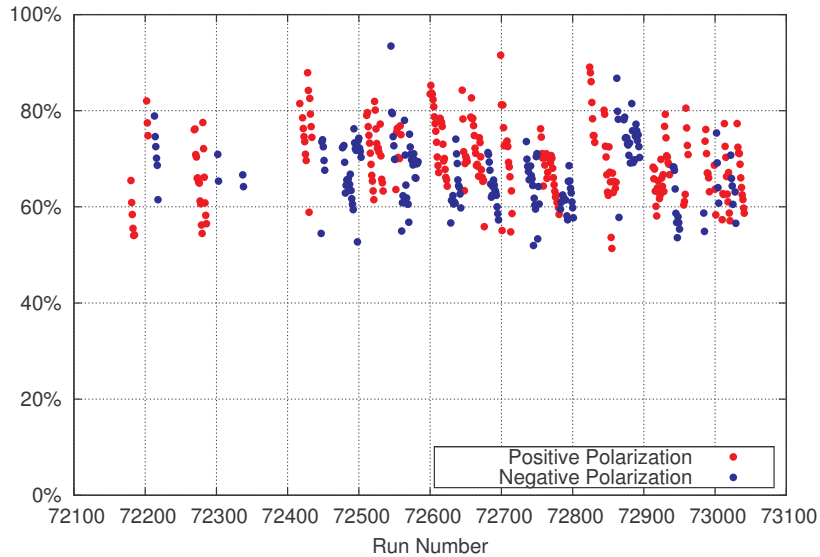


Figure 4.6.: Target polarization by run number.

proton, the microwave frequency can be chosen to drive the proton polarization into either direction.

The polarization was determined by measuring the magnetic susceptibility over a range of frequencies spanning the Larmor frequency for the proton. This was accomplished by using a Q-meter to measure the frequency response of a coil which surrounded the ammonia target material. This NMR coil drives the proton into the metastable state, or if the microwaves are pumping the metastable state, it stimulates photon emission to the stable state. These two states are referred to as the positive and negative polarization states respectively.

An NMR resonance curve was obtained by sweeping the coil frequency, however, this signal was only proportional to the polarization. A thermal equilibrium (TE) measurement was used to provide a proportionality constant needed to get an absolute polarization from the NMR curves. By turning off the microwave pumping, the polarization settles at the known thermal equilibrium value of

$$P_{\text{TE}} = \tanh \frac{\mu B}{kT}. \quad (4.3)$$

The NMR curve at thermal equilibrium provided an absolute calibration for the NMR system. The polarization while pumping is then calculated as

$$\frac{P_{\text{DNP}}}{P_{\text{TE}}} = \frac{A_{\text{DNP}} G_{\text{DNP}}}{A_{\text{TE}} G_{\text{TE}}} \quad (4.4)$$

where A_{DNP} and A_{TE} are the areas under each NMR curve while pumping (DNP) and while at thermal equilibrium (TE), and where G is the gain settings of the amplifiers for each of the two measurements.

A drawing of the target system is shown in figure 4.7. The target used liquid helium to cool both the magnet and the target cell.

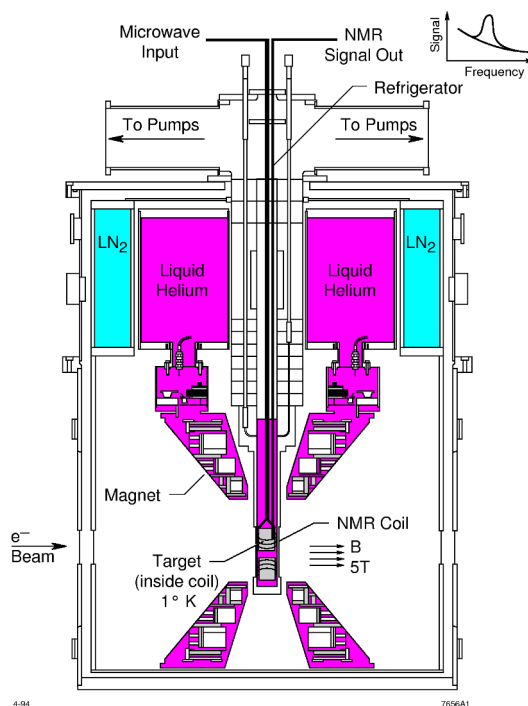


Figure 4.7.: Drawing of the target vacuum chamber and magnet systems.

A more in depth description and analysis of the SANE polarized target can be found in chapter 4 of James Maxwell's thesis [56]. More details on general design and operation of solid polarized targets can be found in [57], [58], and [59].

4.3 BETA

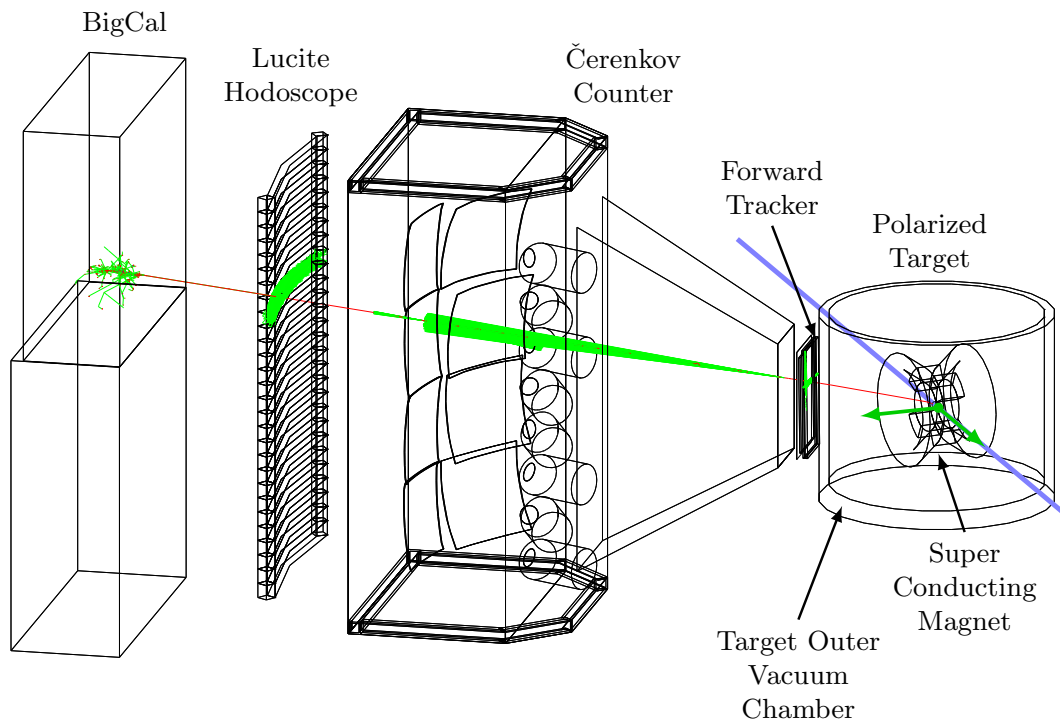


Figure 4.8.: BETA detectors with simulated event.

The Big Electron Telescope Array, BETA, was the primary detector package for the experiment. It differed from traditional DIS experiments by making use of a large acceptance electromagnetic calorimeter and detectors placed in an open configuration where typically a magnetic spectrometer with a limited acceptance. BETA comprises four detectors, a forward tracker placed as close to the target as possible, followed by a threshold gas Čerenkov counter, a Lucite hodoscope and a large electromagnetic calorimeter dubbed BigCal.

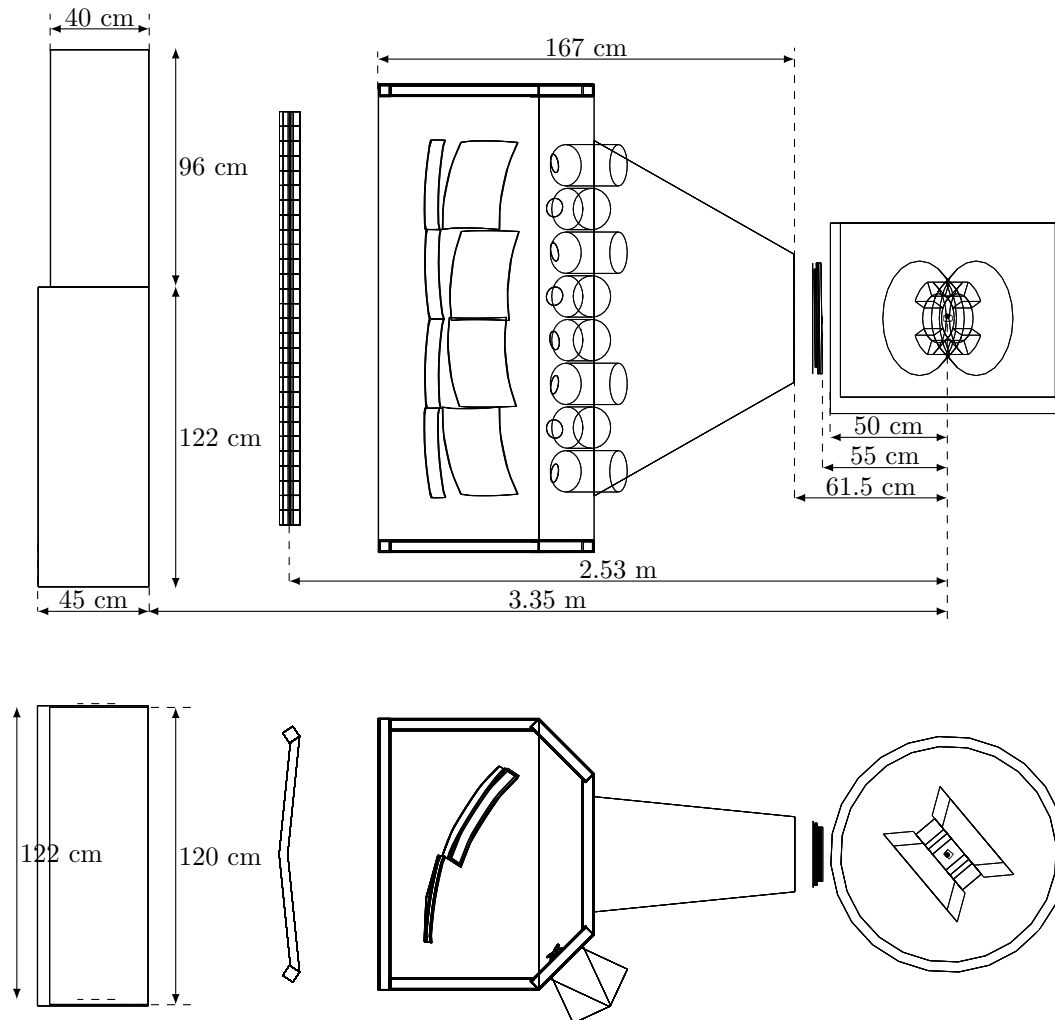


Figure 4.9.: BETA dimensions with side view (upper figure) and a top view (lower figure). Shown from left to right are the calorimeter, hodoscope, Čerenkov counter, forward tracker and polarized target.

4.3.1 BigCal

The BigCal electromagnetic calorimeter provided position and energy measurements of the scattered electrons and photons. It consisted of 1744 lead glass blocks and was divided into two sections.

The upper section (RCS) was from the Yerevan Physics Institute and was previously used during the RCS experiment [60]. Consisting of $4 \times 4 \times 40 \text{ cm}^3$ lead-

glass blocks, the RCS blocks were arranged in a 30×24 array. The lower section (Protvino) was from Institute for High Energy Physics in Protvino, Russia, and it consists of $3.8 \times 3.8 \times 45 \text{ cm}^3$ lead-glass blocks arranged in 32×32 array.

Each block had a PMT and a corresponding ADC readout for each triggered event. BigCal also was a primary component of the data acquisition triggers. In order to reduce complexity and background through correlation a summation scheme was implemented as shown in Figures 4.10 and 4.11. While each channel had an ADC, the smallest segment to have a TDC were groups of 8 (sometimes only 7 for RCS) blocks in the same row. These TDC groups, an example of which is designated by the small hatched area in Figure 4.10, formed 4 timing columns and were analog summed before a discriminated signal was fed to the TDC.

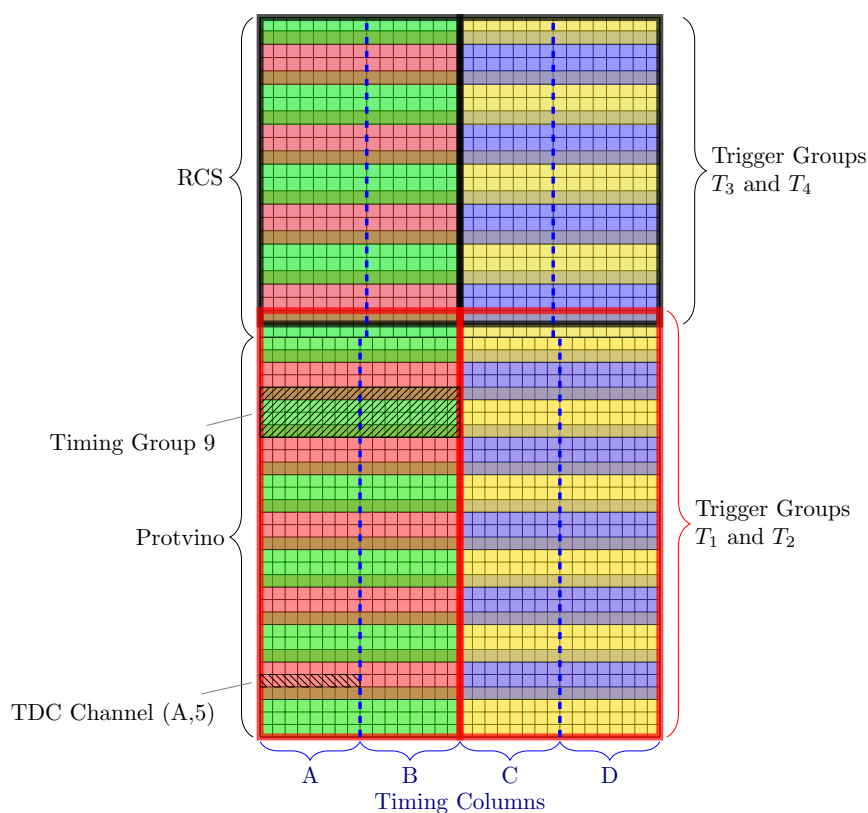


Figure 4.10.: BigCal timing groups and trigger summing scheme. Note that some blocks belong to more than one timing/trigger groups. See the text for more detail.

The analog sums of the TDC groups were split and then summed into larger timing groups of 64 blocks, which span half the width of the detector and 4 blocks vertically. The timing groups were overlapped in order to avoid missing a signal equally split between two groups and is illustrated by the alternating colors shown in Figure 4.10, where an example is shown by the large hatched area.

Finally, by summing the timing groups in each BigCal quadrant, four trigger groups (T_1 , T_2 , T_3 , and T_4) were constructed and used to form the main triggers for the data acquisition. Due to the overlapping of the timing groups, one row of blocks was shared between the RCS and Protvino trigger groups.

4.3.2 Gas Čerenkov

As can be seen in Figure 4.8, the front window of the Čerenkov counter was positioned just behind the forward tracker while BigCal was set at roughly 3.5m from the target. The dimensions and positions of the detectors and target are shown in Figure 4.9.

The gas Čerenkov counter was designed and constructed at Temple University. It was filled with nitrogen gas at atmospheric pressure and used 4 spherical and 4 toroidal mirrors to focus light to quartz window photomultiplier tubes. These three inch quartz window tubes were selected for their UV transparency which was complemented by the special mirror coating for high reflectivity far into the UV. The photomultiplier tubes were aligned in a single column on the side of the tank located at larger scattering angles (as shown in Figure 4.12) in order to reduce the background rates.

Figure 4.13 shows the ADC spectra for each type of mirror. The Čerenkov counter had a large signal of roughly 20 photo-electrons which allowed it to identify the double track peak. This double track peak was instrumental in removing a sizable background from pairs produced outside of the target. A

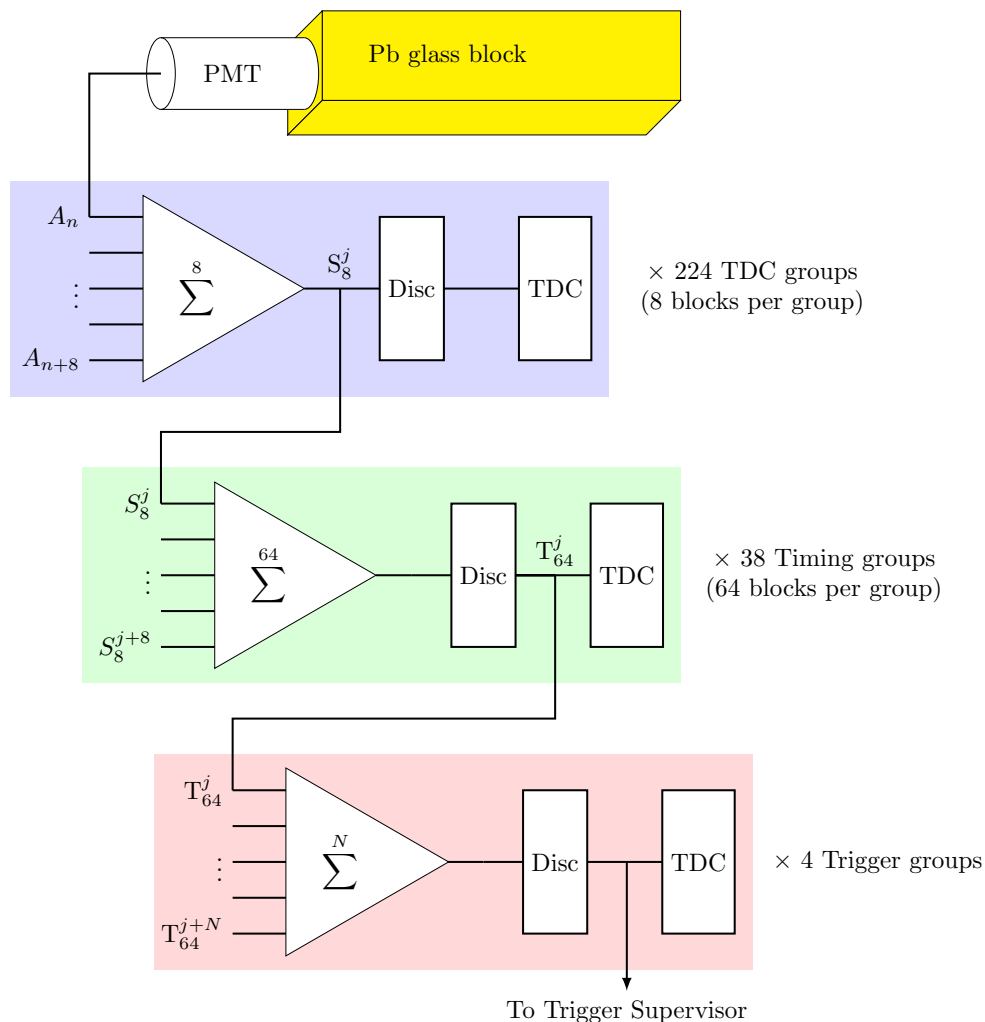


Figure 4.11.: A simplified diagram of the BigCal electronics.

detailed discussion of the design and performance of the SANE Gas Čerenkov can be found in [61].

4.3.3 Lucite Hodoscope

The Lucite hodoscope was built by the group at North Carolina A&T State University. It consisted of 28 curved Lucite bars with light guides mounted to edges cut at 45° as seen in Figure 4.14. Stacked vertically, each bar was 6 cm tall and 3.5 cm thick and provided a vertical position measurement. Photomultipliers

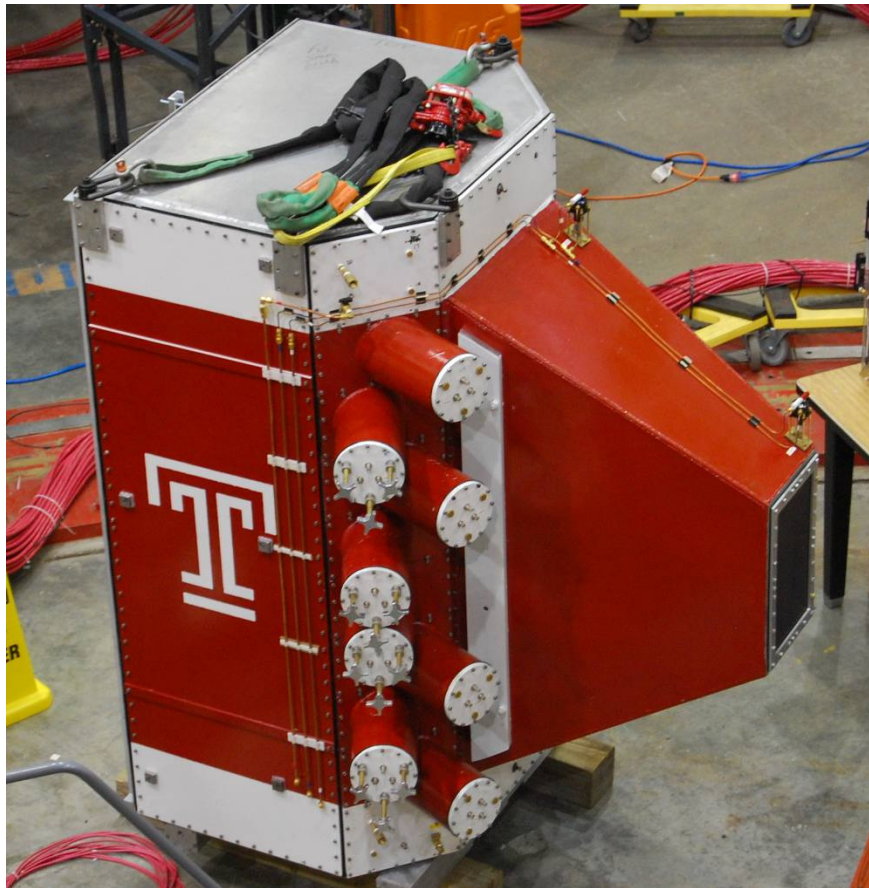


Figure 4.12.: The SANE Gas Čerenkov counter on floor in Hall C.

were connected at both ends of the bar and provided an additional horizontal position measurement by taking the time difference between the two discriminated PMTs signals.

4.3.4 Forward Tracker

The forward tracker used wavelength shifting fibers glued to Bicron plastic scintillator to detect the scattered particles as close to the target as possible. It was built by collaborators at the Norfolk State University and the University of Regina. It used two layers of $3\text{ mm} \times 3\text{ mm} \times 22\text{ cm}$ scintillators, stacked vertically and offset by 1.5 mm, along with a layer of $3\text{ mm} \times 3\text{ mm} \times 40\text{ cm}$ scintillators

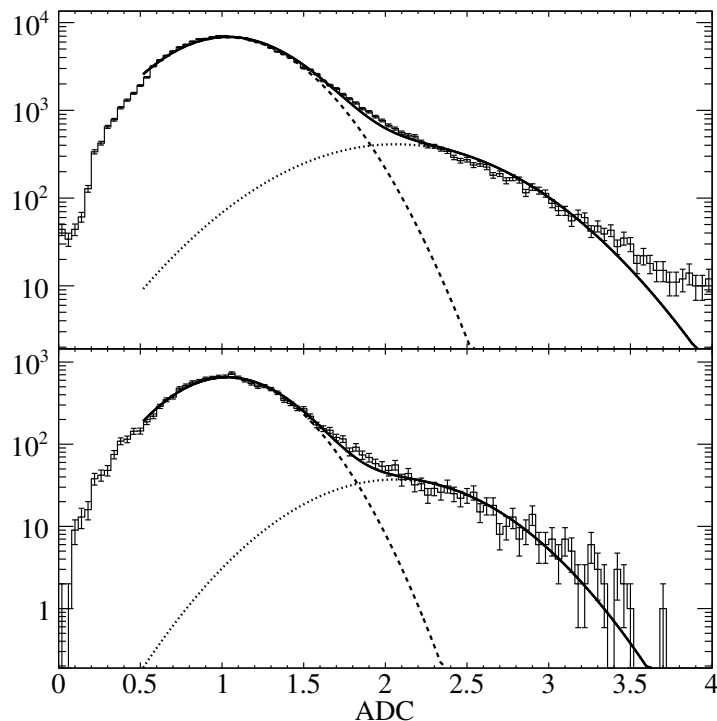


Figure 4.13.: Čerenkov counter ADC spectrum for all the toroidal mirrors (top) and spherical mirrors (bottom).

grouped horizontally to provide a position measurement with a resolution sufficient to distinguish between electron and positron trajectories of momenta, below 1 GeV/c. Due to a truncated commissioning period and higher than expected background rates, the forward tracker was unable to cleanly separate by charge the low energy pair symmetric background.

4.4 Data Acquisition

SANE used the CODA data acquisition system [62] to record event and slow control data. It was controlled by the trigger supervisor (TS) which used a distributed system of read out controllers (ROCs) that each ran a real-time operating system on a single board computer. Typically each electronic crate had a ROC. The event data consisted of all the detector ADC and TDC readouts.

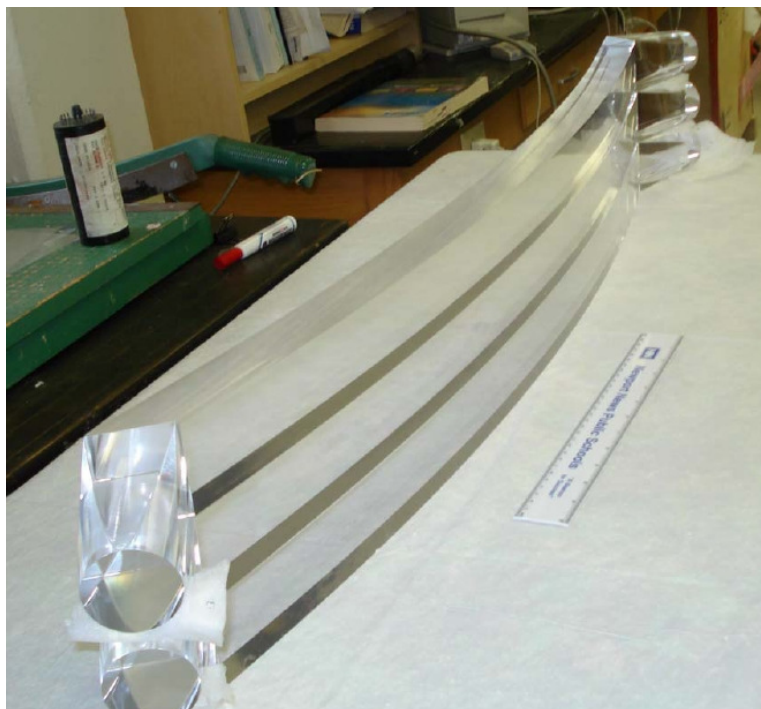


Figure 4.14.: Photograph of three bars before mounting PMTs and wrapping.

Table 4.1.: SANE triggers defined for TS and their nominal prescale factors.

Name	Prescale	Description
PEDESTAL	1	Random gating of ADC for the first 1000 events of each run.
BETA2	1	The main trigger requiring a Čerenkov and BigCal hit.
BETA1	9999	An alternate trigger between BigCal and Čerenkov .
PIO	1	The π^0 trigger requiring two BigCal quadrants to have hits.
COIN	1	The coincidence trigger between BETA and the HMS.
HMS1	1	HMS trigger for electrons
HMS2	1	HMS trigger for hadrons

Many discriminator outputs were counted with scaler modules which provided the important ability to measure the computer dead-time of the DAQ system. The scalers were readout every two seconds. These “scaler events” were placed in sync with the event data. The slow control data (EPICS [63]) was read out every 2 and 30 seconds and was written to a separate data file.

The electronics for BETA were placed in the hall in concrete shielded hut, while most of the (existing) HMS electronics are in the HMS hut or in the counting house. A list of triggers for SANE are given in table 4.1 and a diagram of the main triggers is shown in Figure 4.15.

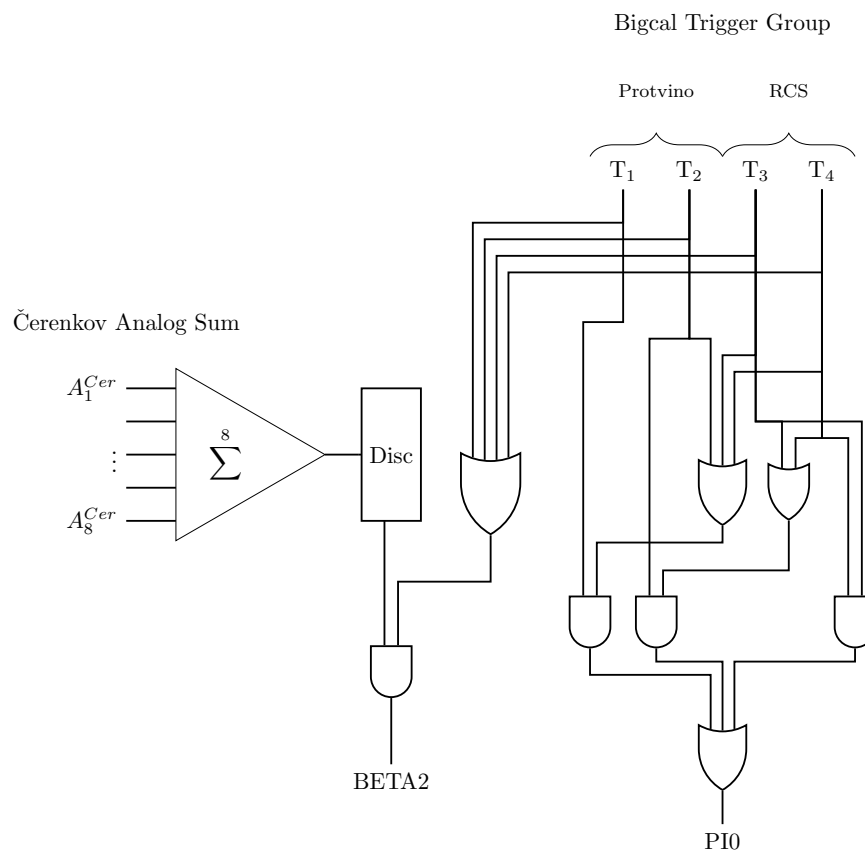


Figure 4.15.: Definitions of the two main triggers, BETA2 and PI0.

CHAPTER 5

DATA ANALYSIS

This chapter describes each step in the detector analysis and the reconstruction of the physics events used to form the asymmetries. We begin with the calorimeter clustering and calibration since it forms the starting point of any track reconstructed by BETA. After the detector calibrations, the method of event reconstruction and selection is presented. The chapter concludes with the calculation of the measured asymmetries and the corrections need to arrive at the asymmetries of physical interest.

5.1 Analysis Overview

The software for the analysis of BETA was written from scratch in C++ making use of the ROOT [64] libraries. The code developed is part of a new larger library called InSANE [65]. The raw data recorded by CODA was extracted using the Hall C ENGINE where the output HBOOK files were directly converted into ROOT files. The scaler events were also incorporated into this new analysis code base. A GEANT4 [66] simulation called BETAG4 [67] was developed as well.

One challenge was collecting and organizing the many disparate data sources needed for the analysis. Therefore a run database, implemented in MySQL, was the primary source for run information. This database was synchronized with a run object stored in each ROOT file. The run object and database were updated for each analysis pass described below.

The analysis was partitioned into a series of passes as outlined in table 5.1. Each pass had a list of corrections and calculations that were performed at the event level. All the corrections, e.g. ADC pedestal subtraction, were performed

before processing the calculations, e.g. converting an ADC value into an energy. This allowed for a systematic and incremental approach to constructing the analysis.

At the scaler event level, each analysis pass contained a list of scaler calculations and filters which were processed for each scaler event. Because the scalers were synchronized with detector events, the filters performed calculations for the interval of detector events by looking to the next scaler event. In a very general way this allowed for data quality checks to be automatically performed by raising flags or skipping bad periods of an otherwise good run. For example, a beam current filter was written to monitor for beam current issues like beam trips. Below a threshold of 70 nA, it raised a warning flag (which was recorded in a run database), but when the beam current fell below 60 nA it recorded a beam trip and skips the events between scaler reads until a proper beam current is restored. The beam trip information (run number, starting time, duration, threshold value) were also recorded in a run database.

5.2 Clustering

Clustering is a large field of data analysis and has many uses. For present purposes we refer to clustering as partitional clustering, as opposed to a hierarchical clustering. For each event that triggers either the BETA2 or PI0 triggers, it is likely that a shower spread across a few blocks and should be grouped into a cluster. We must determine the number of clusters and determine which blocks are associated with each cluster.

This may seem straightforward, however, operating in an open configuration increases the amount of background and clustering should be done carefully to avoid noisy blocks and overlapping showers.

Table 5.1.: An outline of tasks for each analysis pass.

Pass	Description
-2	<ul style="list-style-type: none"> • Raw data extracted • HBOOK files converted into ROOT files. • Epics data filled in a database.
-1	<ul style="list-style-type: none"> • Raw data ntuples converted into InSANE analysis trees. • Scalers converted into InSANE scaler tree. • Fits ADC pedestals • Finds timing peaks • Calorimeter clustering
0	<ul style="list-style-type: none"> • Subtracts ADC pedestals • Performs time-walk corrections • Calculates accumulated charge • Calculates calibrated results (e.g. block energies, Čerenkov photoelectrons ...)
1	<ul style="list-style-type: none"> • Performs hit position reconstruction • Cluster correlations with other detectors • Neural Network corrections • Simple track reconstruction
2	<ul style="list-style-type: none"> • Detailed track reconstruction • Vertex reconstruction • Backward track propagation and tracking

5.2.1 Clustering Algorithm

There are variety of techniques for clustering which require the number of clusters to be determined ahead of time. Determining the number of clusters can be simple or complicated. For BigCal, we expected only a few clusters per event, however, the maximum number of clusters was not fixed in order to avoid missing events and to provide the possibility of rejecting events with too many clusters. Initially, a k-means clustering algorithm was implemented but this required a fixed number of clusters and it was computationally slow for our purposes. Instead, a simple algorithm for determining the number of clusters and associated blocks was developed as follows.

First, from a two dimensional histogram of the event, the calorimeter block with the largest energy is selected as the cluster center. A 5×5 group of blocks is formed around this centroid as shown in Figure 5.2a. If the blocks on the perimeter of this group are detached, they are not included in the cluster. The clusters shown in Figure 5.2 show some examples of clusters. Blocks with non-zero energy that are included in the cluster are shown in red, while detached blocks are shown in green.

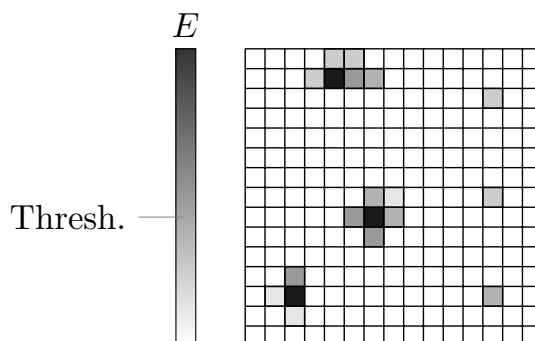


Figure 5.1.: Diagram demonstrating the clustering energy threshold.

Once the detached blocks are removed from the cluster group, those blocks remaining form a cluster and their values are set to zero in the search histogram. Then the next highest energy block forms the seed of the next cluster and so on.

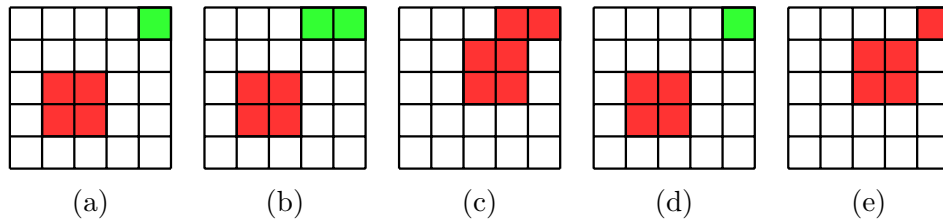


Figure 5.2.: Various classes of clusters. See text for details.

This continues until there are no more blocks with energy above a threshold (see Figure 5.1) of roughly 400 MeV, at which point the search ends.

5.2.2 Cluster Characterization

Once the number of cluster centroids and their corresponding blocks have been determined, various moments characterizing the cluster are calculated and stored. They will be used as inputs for the artificial neural network corrections in appendix C.

The first moment gives the cluster's x and y position

$$\begin{aligned}\mu_x &= \sum_{i,j} x_{ij} \frac{E_{ij}}{E_T} \\ \mu_y &= \sum_{i,j} y_{ij} \frac{E_{ij}}{E_T}\end{aligned}\tag{5.1}$$

where the total cluster energy is $E_T = \sum E_{ij}$, $x_{ij}(y_{ij})$ is the x(y) position of the block (i,j) in BigCal column/row coordinates. The second moment gives the standard deviations

$$\begin{aligned}\sigma_x &= \sqrt{\sum_{i,j} (x_{ij} - \mu_x)^2 \frac{E_{ij}}{E_T}} \\ \sigma_y &= \sqrt{\sum_{i,j} (y_{ij} - \mu_y)^2 \frac{E_{ij}}{E_T}}\end{aligned}\tag{5.2}$$

which indicate the shower size and spread. The skewness is calculated as

$$\begin{aligned}\gamma_1^x &= \sum_{i,j} (x_{ij} - \mu_x)^3 \frac{E_{ij}}{E_T} \\ \gamma_1^y &= \sum_{i,j} (y_{ij} - \mu_y)^3 \frac{E_{ij}}{E_T}\end{aligned}\tag{5.3}$$

which indicates the symmetry of the clusters profiles. A negative(positive) skewness means it is leaning towards larger(smaller) values. The final statistical measure used in characterizing a cluster is the kurtosis which gives a measure of the peakedness. Specifically, we calculate the excess kurtosis as

$$\begin{aligned}\gamma_2^x &= \left(\sum_{i,j} (x_{ij} - \mu_x)^4 \frac{E_{ij}}{E_T} \right) - 3 \\ \gamma_2^y &= \left(\sum_{i,j} (y_{ij} - \mu_y)^4 \frac{E_{ij}}{E_T} \right) - 3.\end{aligned}\tag{5.4}$$

5.3 Detector Calibrations

5.3.1 BigCal Energy Calibration

Unfortunately due to limited experimental beam time and problems with the polarized target magnet, the planned elastic calibrations were not completed. Therefore, the primary energy calibration was achieved through the technique of reconstructing π^0 decays.

Of the many backgrounds are the decay products of the π^0 meson. Because the decay channel is through the strong force ($\tau \sim 10^{-27}$ s), the π^0 decays almost instantly. Therefore, we can safely assume the vertex for such a decay is located at the target. The most probable decay channel is through two photons with a branching ratio, $\Gamma_{\gamma\gamma}/\Gamma_{total} \simeq 0.99$. The next highest decay channel is $\pi^0 \rightarrow e^+e^-\gamma$ with a branching ratio of approximately one percent.

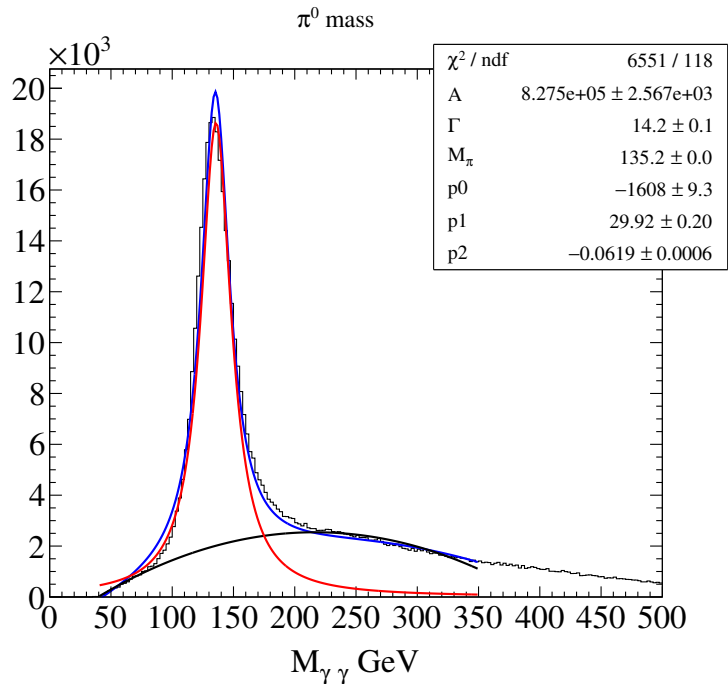


Figure 5.3.: A fit to the calibrated two photon invariant mass spectrum near the π^0 mass peak.

Two photons events were recorded by the P10 trigger. After clustering, the events were selected with an anti-Čerenkov cut on both clusters. The reconstructed mass is

$$M_{\gamma\gamma}^2 = 2\nu_1\nu_2(1 - \cos(\theta_{\gamma\gamma})) \quad (5.5)$$

where $\nu_{1,2}$ are the photon energies and $\theta_{\gamma\gamma}$ is the angle between them. The resulting mass spectrum after calibrating is shown in Figure 5.3. More details of the calibration method and procedure can be found in appendix D.

5.3.2 Gas Čerenkov

Number of Photoelectrons

During the experiment the gas Čerenkov high voltages were set to roughly 100 ADC channels per photo electron. The calibrated number of photoelectrons

for each PMT is shown in Figure 5.4. In order to provide a single variable for event selection, the ADC peaks are aligned as shown in Figure 5.5.

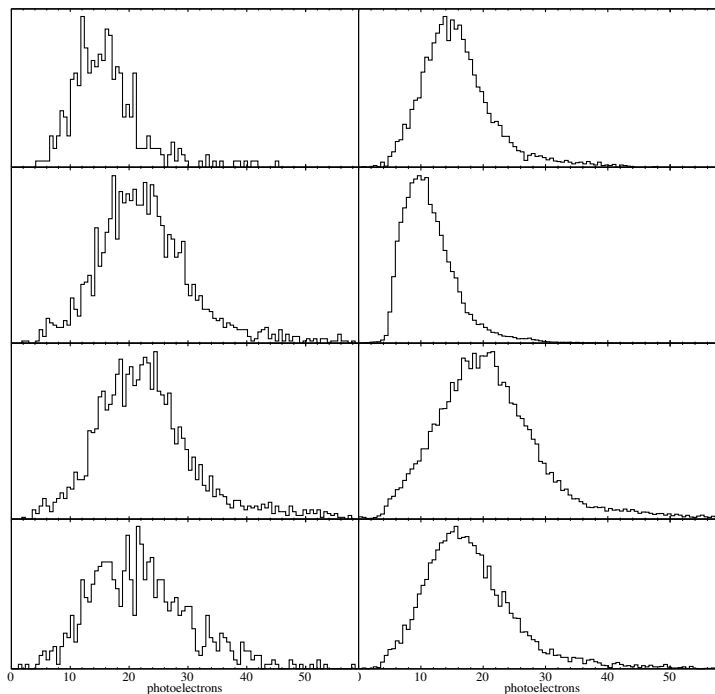


Figure 5.4.: Number of photoelectrons for each Čerenkov mirror.

Cluster Position Correlation

In order to determine the appropriate geometry cuts to place on clusters in BigCal, the Čerenkov mirror edges are found in the BigCal coordinate system by looking at clusters which have multiple TDC hits. The outlines of the mirrors become visible as shown in Figure 5.6. It is interesting that the size of the Čerenkov cone can be roughly estimated from the edge resolution of these hits.

From these mirror edge locations, the appropriate Čerenkov ADC sum can be calculated. For example if the clusters position is well within the center of a mirror, only that mirror is associated for the ADC and TDC. If it falls near a mirror edge, the primary mirror's TDC is used and the ADCs of both mirrors

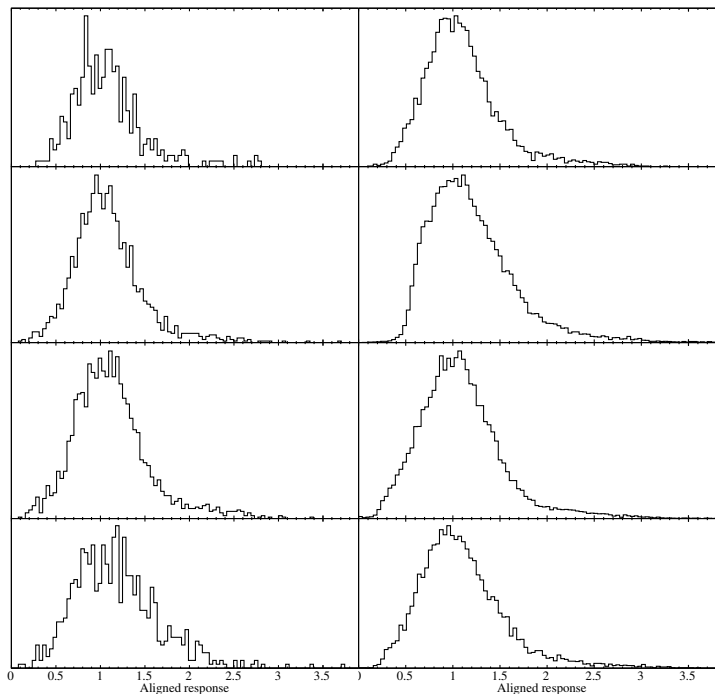


Figure 5.5.: ADC Aligned response for each Čerenkov mirror.

are summed. Similarly, for events in one of the central corners, all four mirrors are summed.

5.3.3 Lucite Hodoscope Calibration

Lucite Position

The Lucite hodoscope did not have any ADC data during the experiment. A multi-hit TDC gathered hits from PMTs mounted on both sides of each bar. In order to determine both x and y position, a TDC hit is required on both sides of the same bar. The timing difference form can then be mapped to a x-position in bigcal. From this and a survey of the detector position prior to the experiment, we can calculate a position at the face of hodoscope.

The index of refraction for Lucite is $n_{Lucite} = 1.495$ and the maximum angle of the Cherenkov light cone is $\cos^{-1}(1/n_{Lucite}) = 48$ degrees. Since the light

Cherenkov Mirror Edges

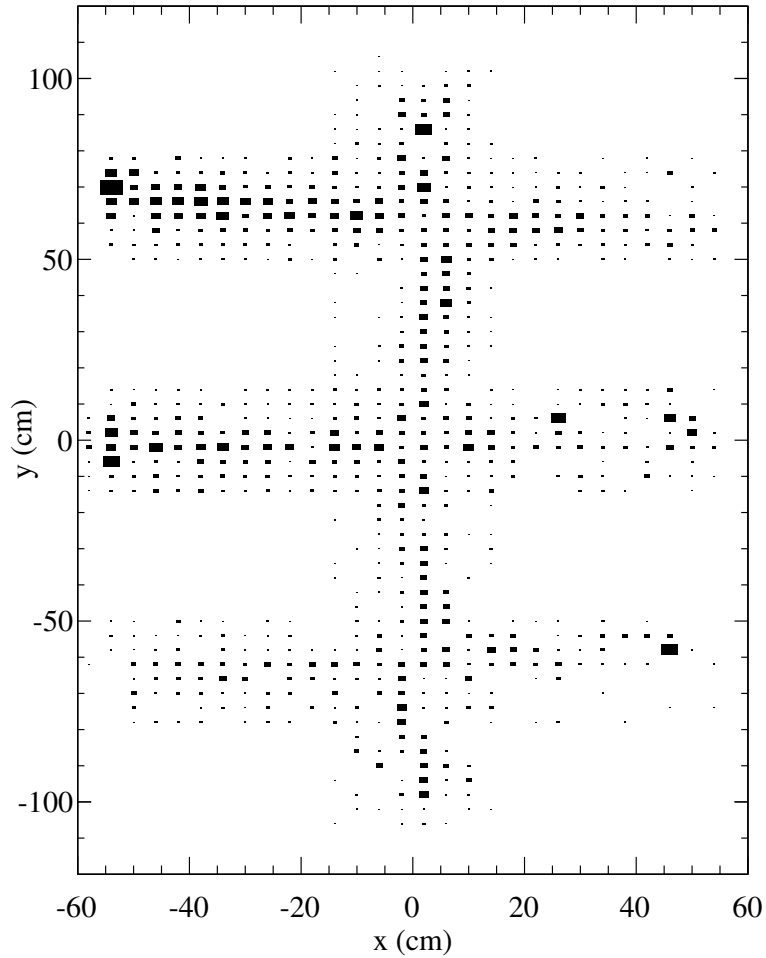


Figure 5.6.: A calibration of the mirror edges.

will propagate along the bar with reflections of about 45 degrees, a photon's path length to the PMT light guide will be about $\sqrt{2}$ larger than the direct length. Using this approximation and knowing that the Jlab F1TDC's have a time resolution of about 60 ps per channel, we can get the direct length from the TDC value as

$$x_{luc} = (TDC) \frac{(60ps)c}{\sqrt{2}n_{Lucite}} \simeq (TDC)(0.8505 \frac{cm}{chan}) \quad (5.6)$$

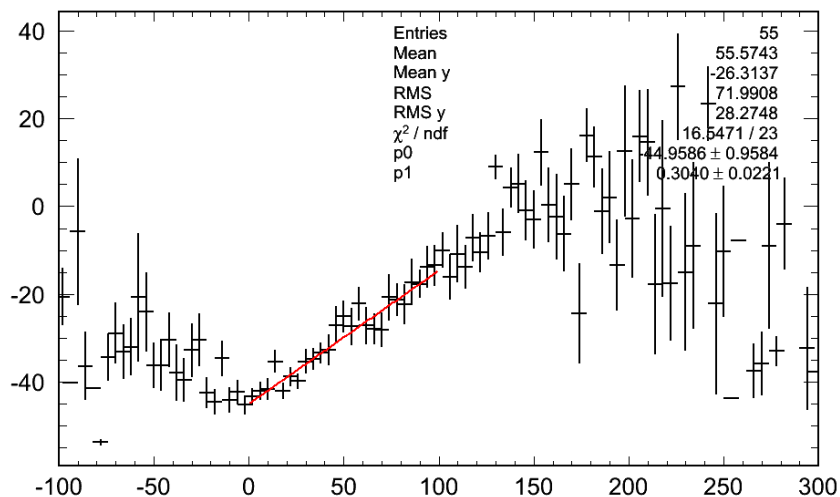


Figure 5.7.: An example of a Lucite Hodoscope X position calibration. Note the fit function gives the BigCal x-cluster position (vertical axis) as a function of the Lucite hodoscope bar TDC difference.

5.3.4 Forward Tracker Calibration

The forward tracker position reconstruction relied on accurate knowledge of each scintillator’s position. This required detailed construction and survey information.

5.4 Event Reconstruction and Selection

The values of the relevant physical quantities at the target were reconstructed using a two step sequence of neural networks. The primary reason for a two step process was to separate two unrelated corrections: the cluster position correction and the reconstruction of the scattering angles at the target.

The first network provided a position correction for the cluster due to varying angles of incidence. It calculated a cluster position correction to determine the

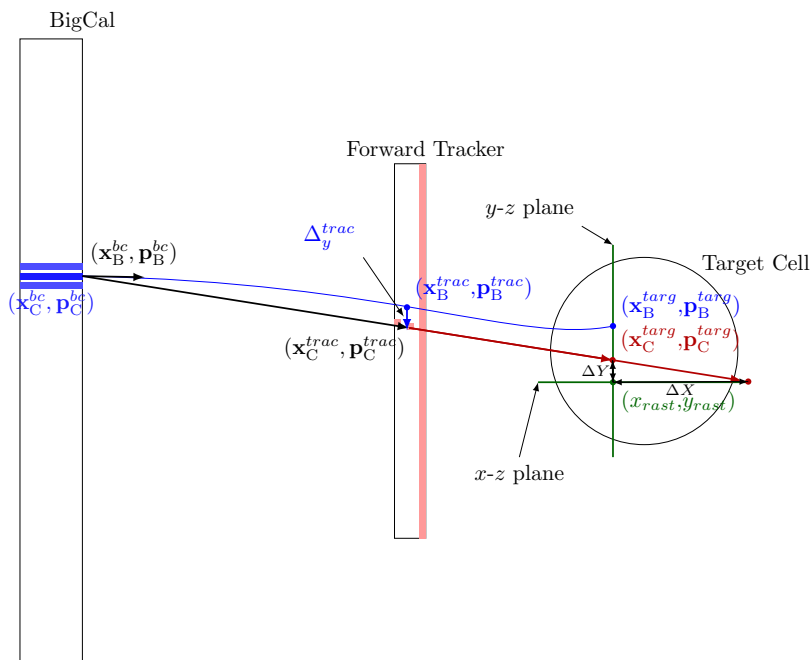


Figure 5.8.: Definition of BETA tracking positions.

track crossing position at the front face of the calorimeter, the BigCal plane, as shown in C.1. The improvement in the position resolution can be seen in Figure C.5 where the red curve shows the improved position resolution over the cluster position .

The second network provided corrections to the scattering angles that are naively calculated as straight lines from the target to the BigCal plane. It corrected for the bending of the tracks as it transitioned through the target volume of strong magnetic fields. This was also checked with two independent particle tracking codes. A detailed discussion of the neural networks is given in appendix C.

The Čerenkov counter identified scattered electrons in coincidence with a shower in BigCal. In order to reduce uncorrelated background, a timing cut was placed on the TDC spectrum as shown in Figure 5.10. In order to reduce the number of background events falling into this cut, the TDC peak was time-walk corrected. As the red curve shows, this correction was small due to the large

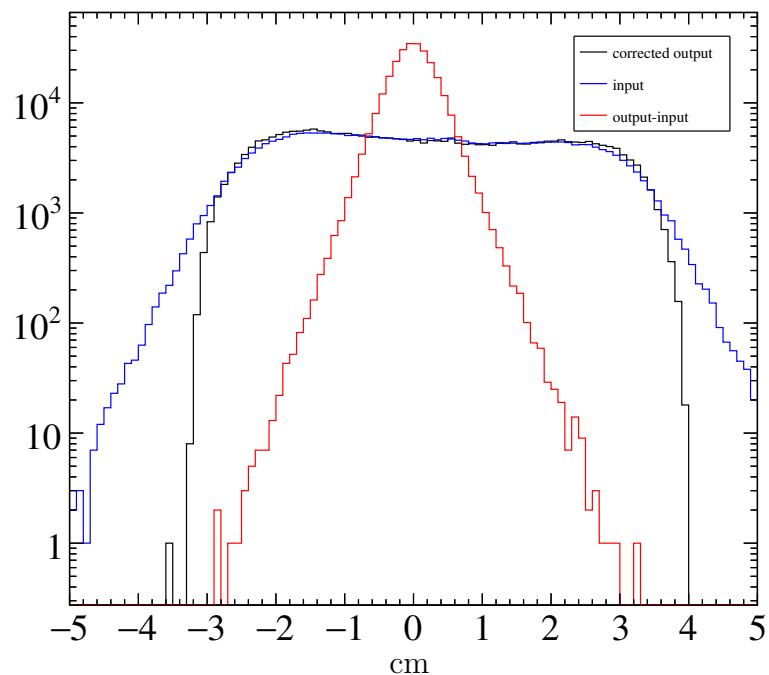


Figure 5.9.: Results of training for a position correction δ_x . The red histogram shows the difference between the network output (black) and the training data set (blue).

Čerenkov signal relative to the discriminator thresholds. That is only a small fraction of events had a signal small enough for the discriminator to be sensitive to its shape.

The track normalized Čerenkov ADC signal is shown in Figure 5.11 where the Čerenkov ADC window cut is defined by the events between the two vertical lines. The purpose of this cut is to remove the background of pairs produced by photons outside of the central region of the target magnetic field. Pairs were mostly produced in the forward tracker material which had a total radiation length comparable to the target.

In order to further reduce backgrounds a timed hit in the Lucite hodoscope with a vertical position roughly correlated with the cluster position.

The forward tracker was not used for the main event reconstruction.

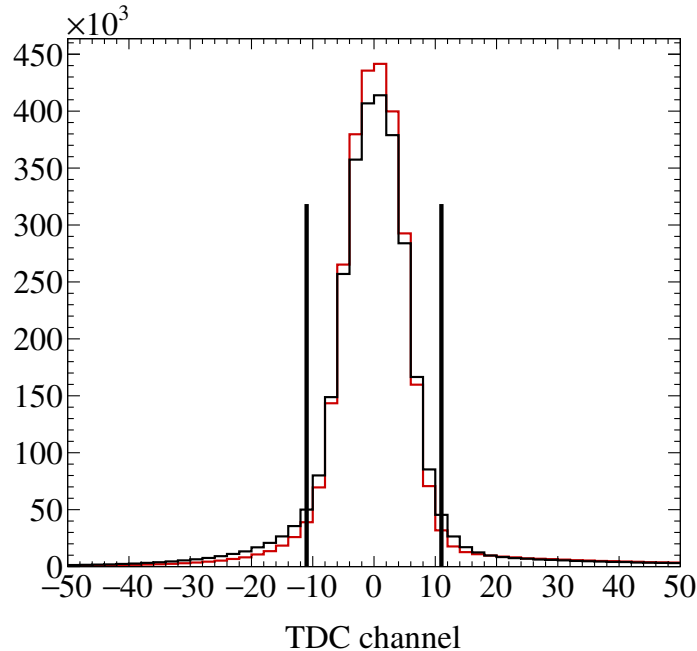


Figure 5.10.: The Čerenkov TDC peak without (black) and with (red) a time-walk correction. The Vertical lines define the TDC selection cut.

5.5 Asymmetry Measurements

SANE set out to measure the double spin cross section asymmetry formed by a polarized target and longitudinally polarized electron beam for two target configurations. The two measured asymmetries utilized a target polarization anti-parallel to the beam and a target polarization angle at 80 degrees. These asymmetries, A_{80} and A_{180} , are used to extract the proton's virtual Compton scattering asymmetries and spin structure functions.

The raw asymmetries must be corrected for a number of effects in order to arrive at the asymmetries one would measure under ideal experimental conditions. The ideal conditions would be a 100% polarized beam of nearly infinite current, an infinitely thin target made of a single layer of protons with 100% polarization, event selection cuts that provide 100% background rejection efficiency, zero window and detector material thicknesses precluding external radiative corrections,

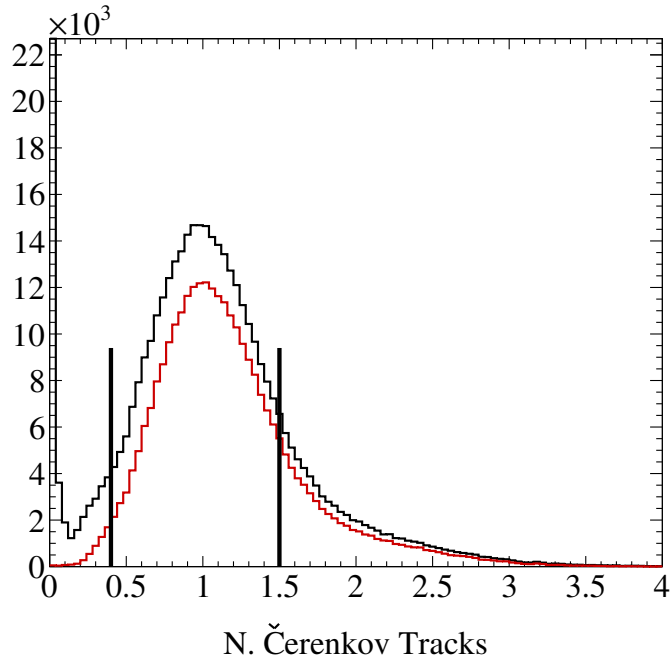


Figure 5.11.: The Čerenkov ADC spectrum without (black) and with (red) a TDC cut. The Čerenkov ADC window cut is defined by the vertical lines.

zero data acquisition dead-time, and perfect event reconstruction. Of course, this scenario is experimentally impossible so we must proceed with the following corrections.

5.5.1 Measured Asymmetry

The raw counting asymmetry was measured as

$$A_{raw} = \frac{n_+ - n_-}{n_+ + n_-} \quad (5.7)$$

where n_+ (n_-) is the number of events with positive (negative) beam helicity. These do not take into account a charge asymmetry, A_Q , or the computer dead-

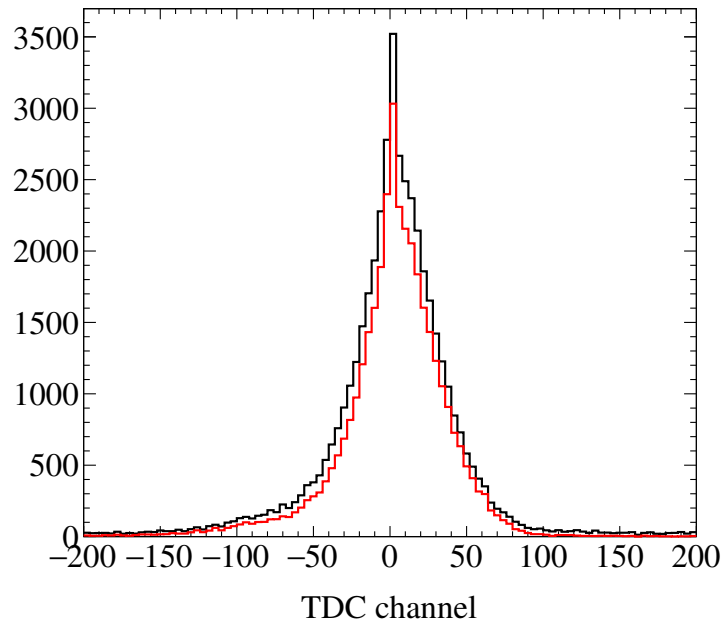


Figure 5.12.: The Lucite Hodoscope TDC spectrum without (black) and with (red) the Čerenkov TDC cut.

time. Instead of using the raw event counts, n , the charge and live-time corrected counts were used. The measured asymmetry becomes

$$A_m = \frac{N_+ - N_-}{N_+ + N_-} \quad (5.8)$$

where the corrected rates are

$$N_{\pm} = \frac{n_{\pm}}{Q_{\pm}L_{\pm}}, \quad (5.9)$$

n_{\pm} is the raw number of counts, Q_{\pm} is the accumulated charge for the given beam helicity over the counting period, and L_{\pm} is the live time for each helicity.

The charge asymmetry used for each run is shown in Figure 5.13.

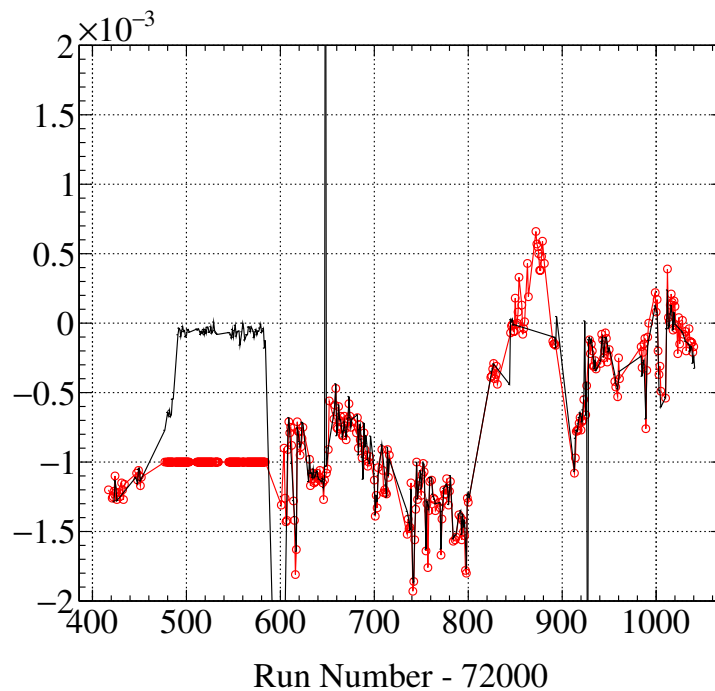


Figure 5.13.: The charge asymmetry vs run number.

Live Time

The live time is the fraction of time that the data acquisition is available for triggers and is related to the dead-time, $L = 1 - D$, where L is the live time and D is the dead time. The live time for each helicity was measured by the ratio of triggers to scalars, $L_{\pm} = n_{\pm}/s_{\pm}$. In this way the total counts for each helicity can be properly corrected if the live time asymmetry is large.

The BETA DAQ had only the positive helicity input trigger scaler due to a cabling problem. The live time was then calculated from a fit to the live time vs the number of triggers between scaler readouts. This assumes that the live times are proportional to the number of recorded triggers.

5.5.2 Corrected Asymmetry

The asymmetry is calculated as

$$A_{physics} = \frac{1}{df(W, Q^2) P_B P_T} \left(\frac{N_+ - N_-}{N_+ + N_-} \right) \quad (5.10)$$

where P_B and P_T are the beam and target polarizations which have been previously calculated in sections 4.1.1 and 4.2. The dilution factor, $df(W, Q^2)$, takes into account scattering from unpolarized nucleons in the target.

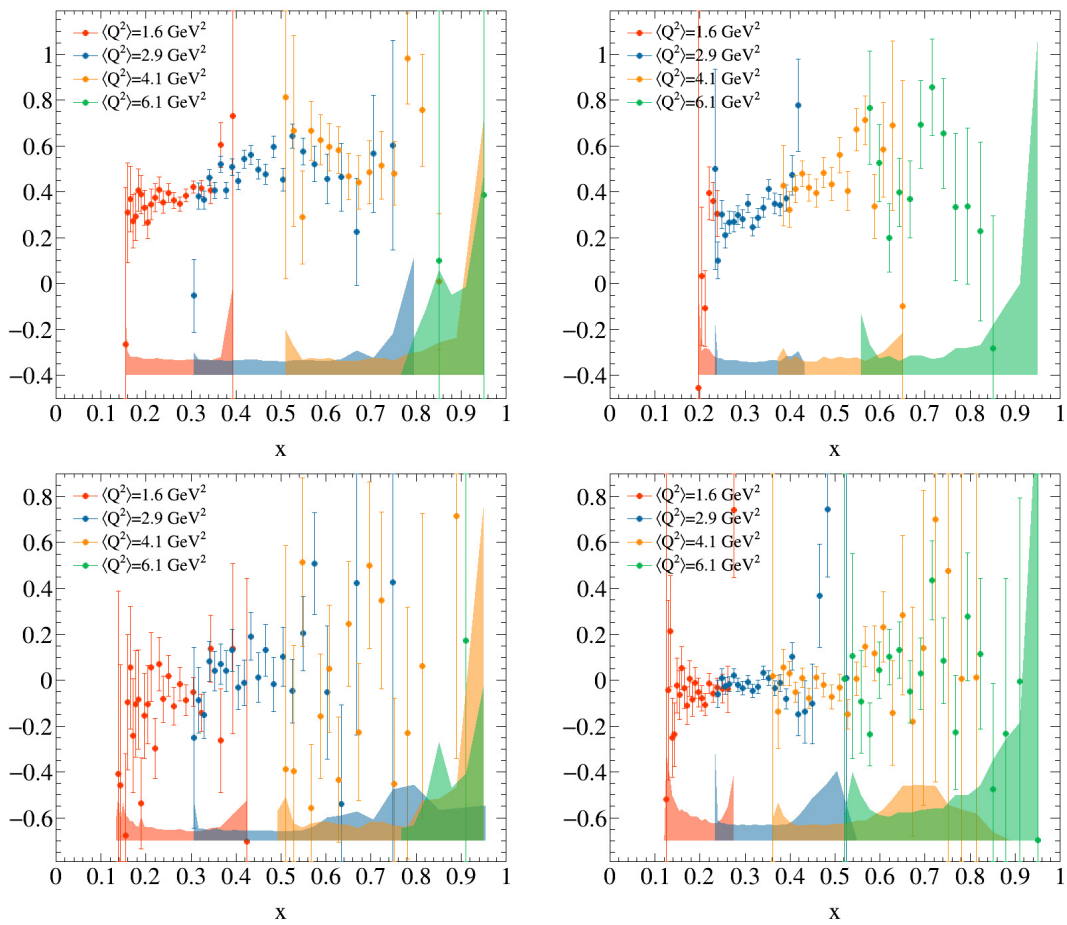


Figure 5.14.: Asymmetries after correcting for beam polarization, target polarization, and target dilution. The top plots show the anti-parallel configuration and the bottom show the perpendicular.

5.5.3 Dilution factor

The dilution factor was calculated for each run following

$$df(W, Q^2) = \frac{N_p \sigma_p(W, Q^2)}{N_p \sigma_p(W, Q^2) + \sum_i N_i \sigma_i(W, Q^2)} \quad (5.11)$$

where N_p is the number density of protons (in NH_3) and N_i is the density of all the other nuclei that make up the target. This includes contributions from the entrance and exit windows, liquid helium, NMR coil. All materials used to calculate the dilution can be found in table C.1 of [56].

The polarized target material was formed into solid ammonia beads and placed into a cup which was inserted into a bath of liquid helium. In order to determine the number density of polarized proton, the so called *packing fraction* is the ratio of bead material to liquid helium found within the volume of the target cell (see Figure 5.15).

The packing fraction were determined by comparing the yields measured by the High Momentum Spectrometer (HMS) to a simulation. A carbon target with an precisely known packing fraction was used to provide a baseline and calibration point for the simulation. For this reason carbon target runs were take throughout the experiment in order to eliminate possible systematic variations in the HMS yields over long periods of time. The packing fractions on average were around 60% and a detailed listing of each target cell load can found in Table 5.1 of [56].

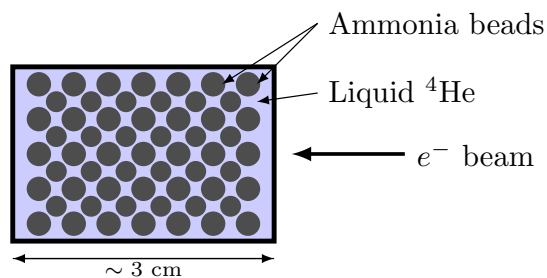


Figure 5.15.: A diagram of the target cup showing the packing fraction.

The cross sections in 5.11 were calculated from empirical fits to the structure functions and form factors. The cross sections included all radiative corrections calculated in appendix E. Their accurate calculation was instrumental in pushing the energy cut lower where the elastic and quasi-elastic radiative tails become significant. The growing contribution from the proton elastic radiative tail can be seen in the dilution factor shown in Figure 5.16.

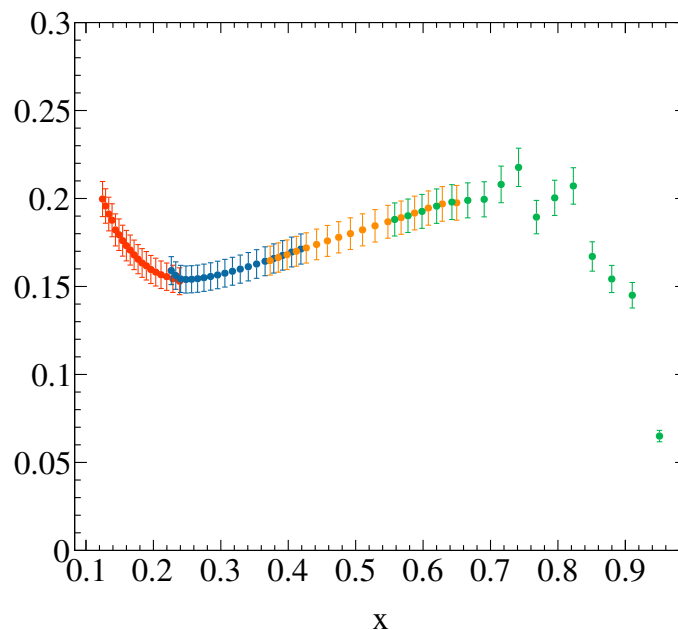


Figure 5.16.: The dilution factor calculated for run 72925 as a function of x , showing the increasing contribution from the elastic tails at lower energies (i.e. lower x).

5.6 Pair Symmetric Background

After correcting for polarization and target dilution, the background of positrons, almost entirely due to π^0 decays, was corrected for with a background dilution

term and a contamination term which was subtracted. The correction can be written

$$A_{cor} = C_{pair} A_{phys} \quad (5.12)$$

$$= \left(\frac{1}{f_{bg}} \right) A_{phys} - (C_{A_{bg}}) \quad (5.13)$$

where C_{bg} is a contamination due the asymmetry of the pair symmetric background and f_{bg} is a background dilution. The resulting asymmetry, A_{cor} , is the asymmetry after correcting for the background a is now only due to scattered electrons.

A fit of inclusive charged pion asymmetries was performed by Oscar Rondon [68] in order to estimate the size of the contamination term in 5.12. It was determined that for SANE the background asymmetry is $A_{bg} \simeq -0.022 \pm 0.002$.

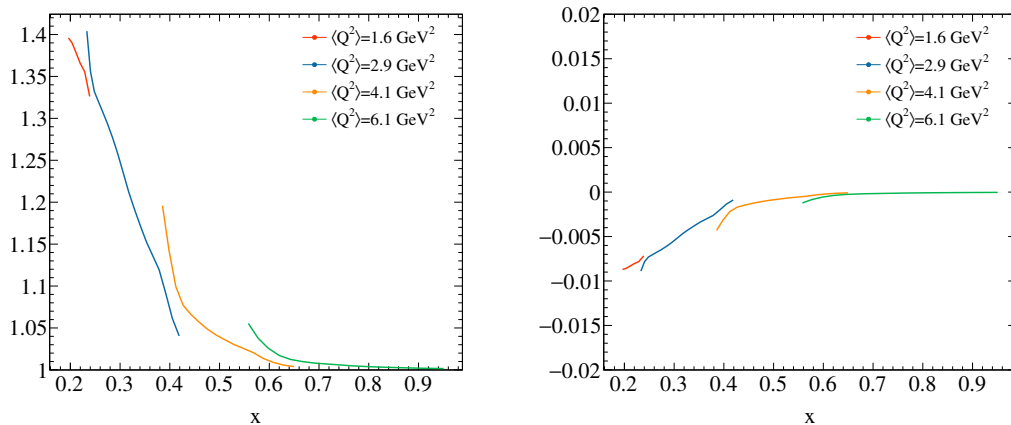


Figure 5.17.: The background dilution (left), $1/f_{bg}$, and background contamination (right), C_{bg} , terms calculated for the anti-parallel 5.9 GeV configuration.

5.7 Radiative Corrections

After correcting for the pair symmetric background the radiative corrections were applied following the standard formalism laid out by Mo and Tsai [69] as

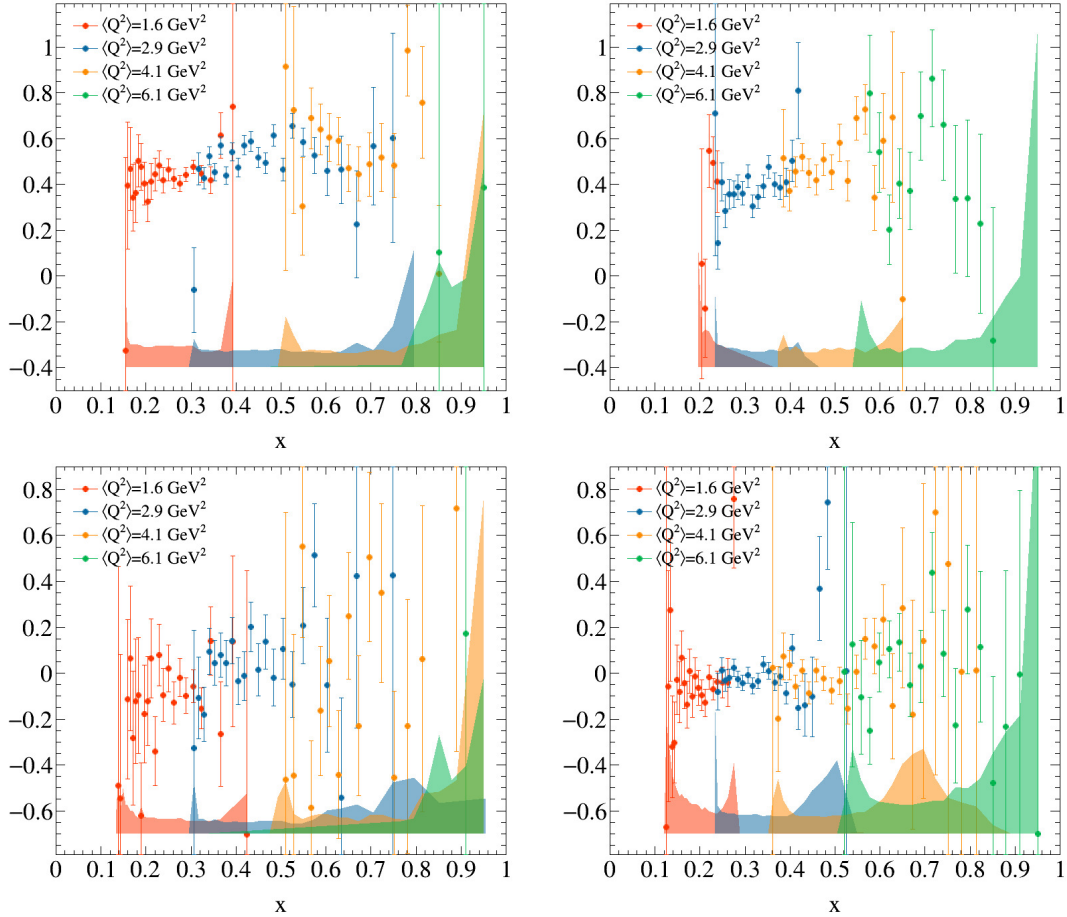


Figure 5.18.: Same as Figure 5.14 but with the asymmetries corrected for the pair symmetric background.

well as the polarization dependent treatment of Akushevich, et.al. [70]. Many details of the radiative corrections can be found in appendix E.

The elastic radiative tail was calculated from models of the proton form factor [71] and a detailed description of the target geometry. The asymmetry was corrected with an elastic dilution factor and contamination term. The total “radiated” asymmetry (corrected for pair symmetric background) is

$$\begin{aligned}
 A_{cor} &= \frac{\Delta_{r+t}^T}{\Sigma_{r+t}^T} \\
 &= \frac{\Delta_{r+t}^{in} + \Delta_{r+t}^{el}}{\Sigma_{r+t}^{in} + \Sigma_{r+t}^{el}}
 \end{aligned}
 \tag{5.14}$$

where Δ_{r+t} is the difference between radiated cross sections, and Σ_{r+t} is the cross section sum. The superscripts indicate the total, inelastic, and elastic cross sections should be used, respectively.

We are interested in obtaining the inelastic Born cross section asymmetry, A_0^{in} , and therefore must subtract the elastic tail contributions. Using 5.14, this asymmetry is

$$\begin{aligned} A_{in} &= \frac{\Delta_{r+t}^{in}}{\Sigma_{r+t}^{in}} \\ &= \frac{1}{f_{el}} A_{cor} - C_{el} \end{aligned} \quad (5.15)$$

where

$$\frac{1}{f_{el}} = \frac{\Sigma_{r+t}^T}{\Sigma_{r+t}^{in}} \quad (5.16)$$

and

$$C_{el} = \frac{\Delta_{r+t}^{el}}{\Sigma_{r+t}^{in}}. \quad (5.17)$$

It is clear from 5.16 and 5.17 that not only an accurate calculation of the elastic radiative tail is needed to subtract the elastic tail, but an accurate calculation of the inelastic radiative tail as well.

The dilution and contamination terms are shown in Figure 5.19. As expected the dilution term follows the shape of the elastic radiative tail (see E.1).

Typically after subtracting the elastic tail contributions the Born cross section is obtained by fitting the data in an iterative fashion. This assumes that there is a wide range of kinematics covered in scattered energy and incident energy as discussed in appendix E. Furthermore, since only an asymmetry was measured over limited kinematics an unfolding procedure becomes impossible. The correction to the asymmetry is calculated as a contamination

$$A_0^{in} = A_{in} - C_{in}. \quad (5.18)$$

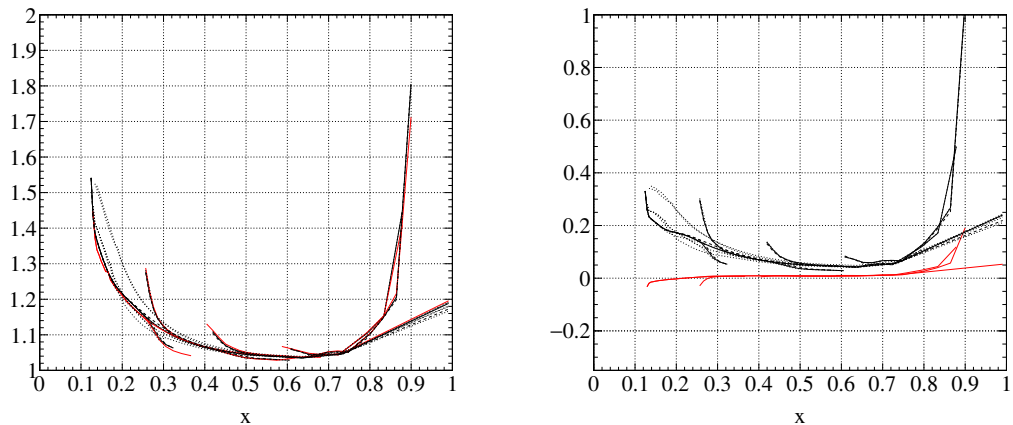


Figure 5.19.: Elastic radiative tail dilution $1/f_{el}$ (left), and contamination C_{el} (right) calculated for the parallel (black) and perpendicular (red) configurations for a 4.7 GeV incident beam energy.

Fortunately the correction for the inelastic radiative tail calculated from different models and fits is small. Using a variety of input models to understand the systematic error introduced, the inelastic

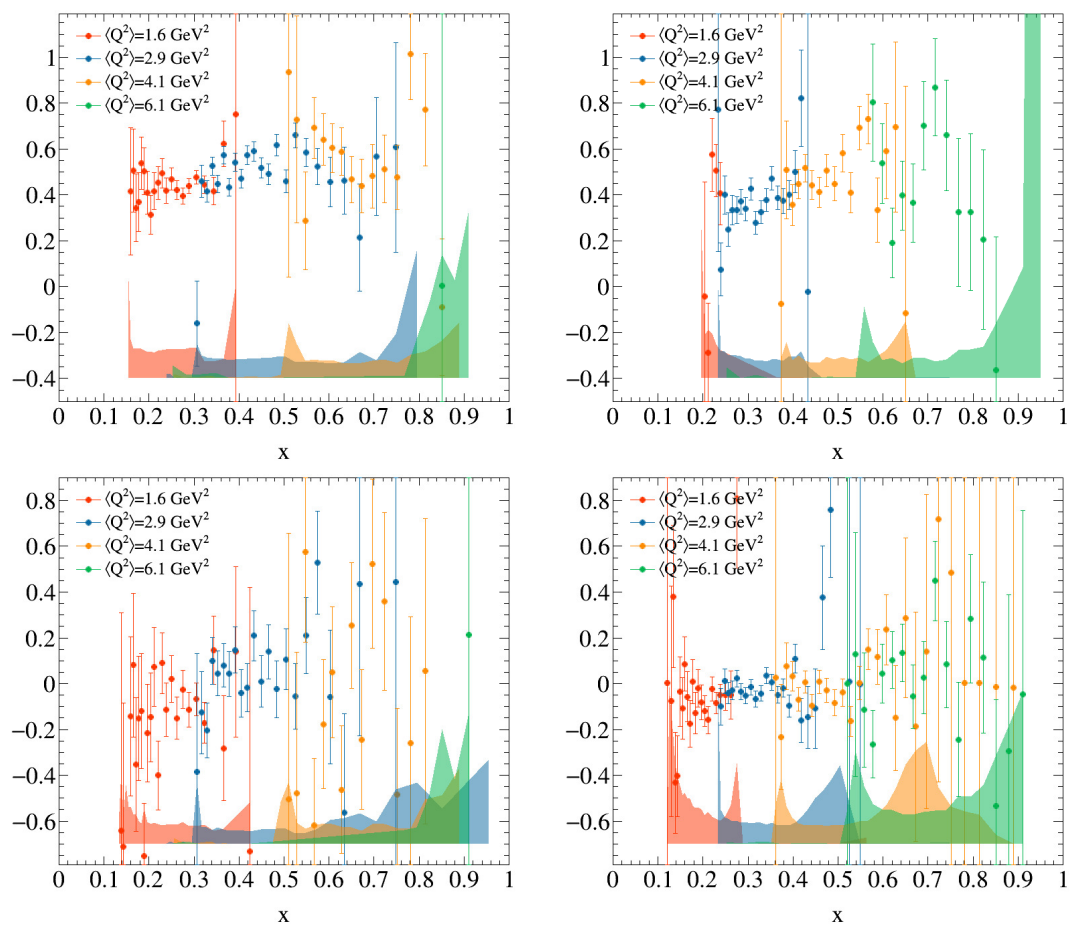


Figure 5.20.: Same as Figure 5.14 but with the elastic radiative tail subtracted.

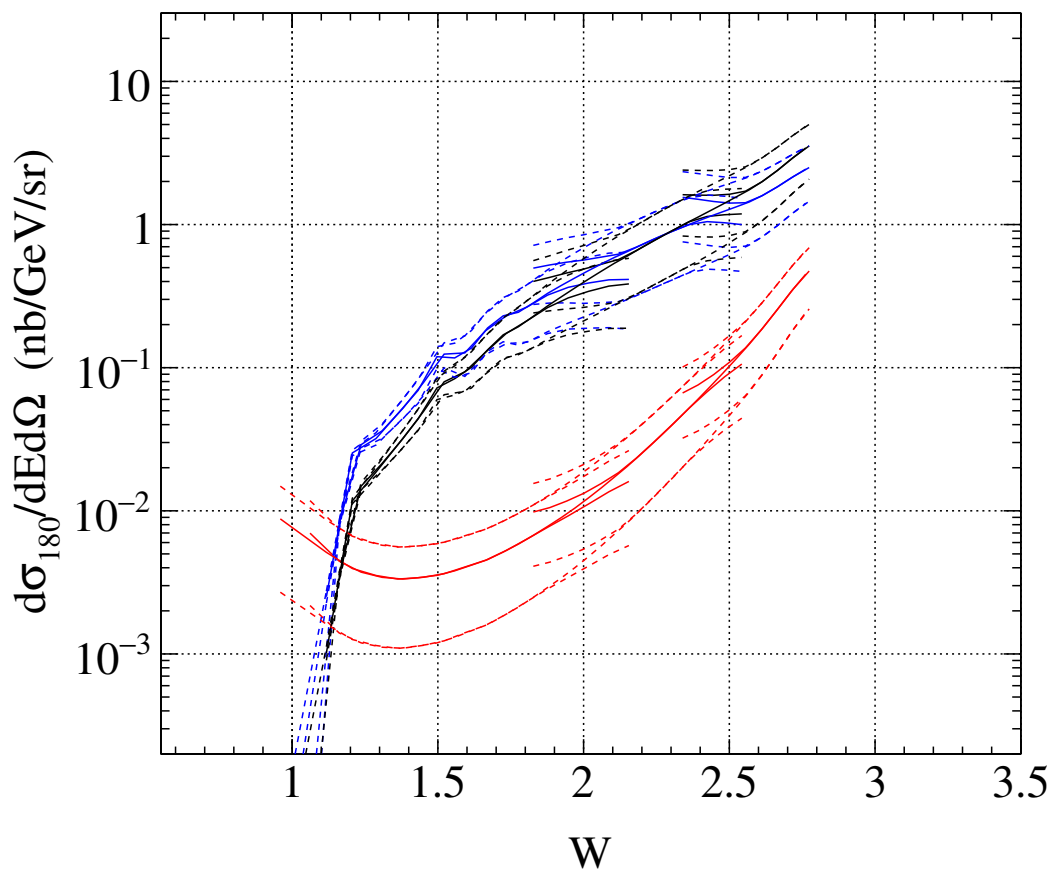


Figure 5.21.: The inelastic radiative tail (blue), elastic radiative tail (red), and inelastic Born (black) cross sections for the anti-parallel target configuration and 5.9 GeV incident beam energy. The dashed lines are the cross sections corresponding to the two beam helicity states.

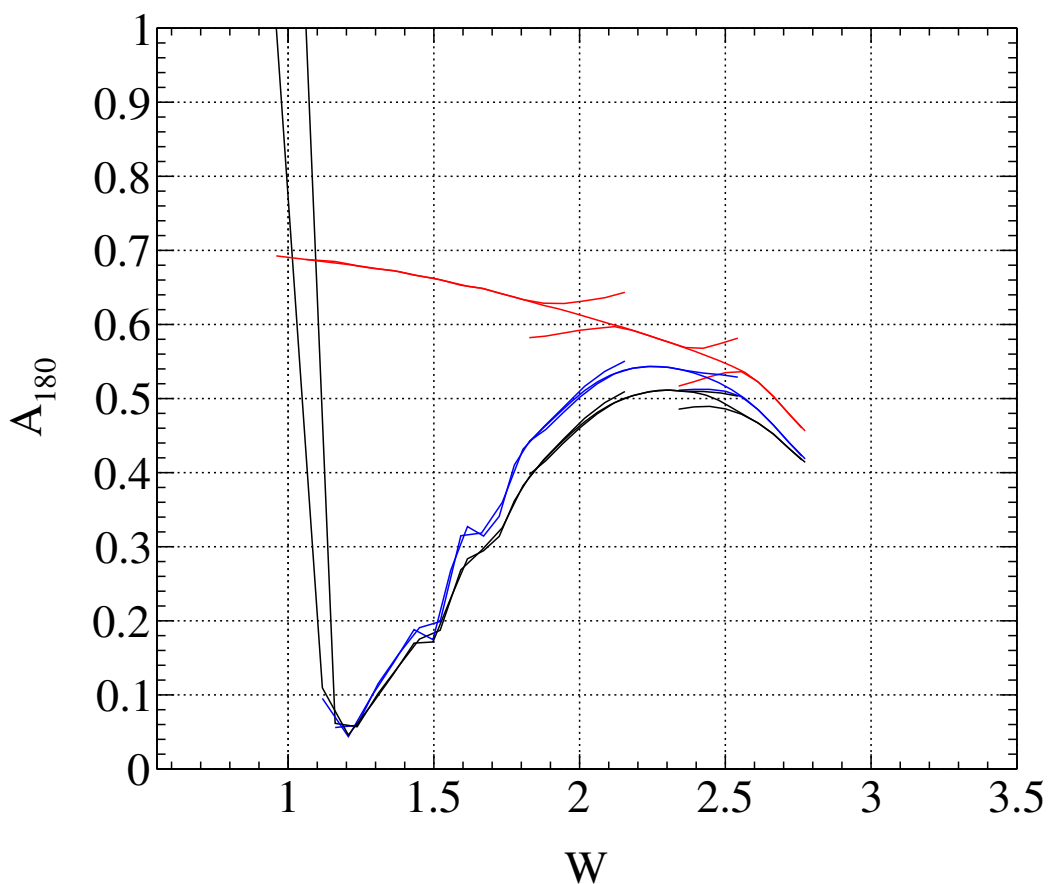


Figure 5.22.: The inelastic radiative tail (blue), elastic radiative tail (red), and inelastic Born (black) cross sections for the anti-parallel target configuration and 5.9 GeV incident beam energy. The dashed lines are the cross sections corresponding to the two beam helicity states.

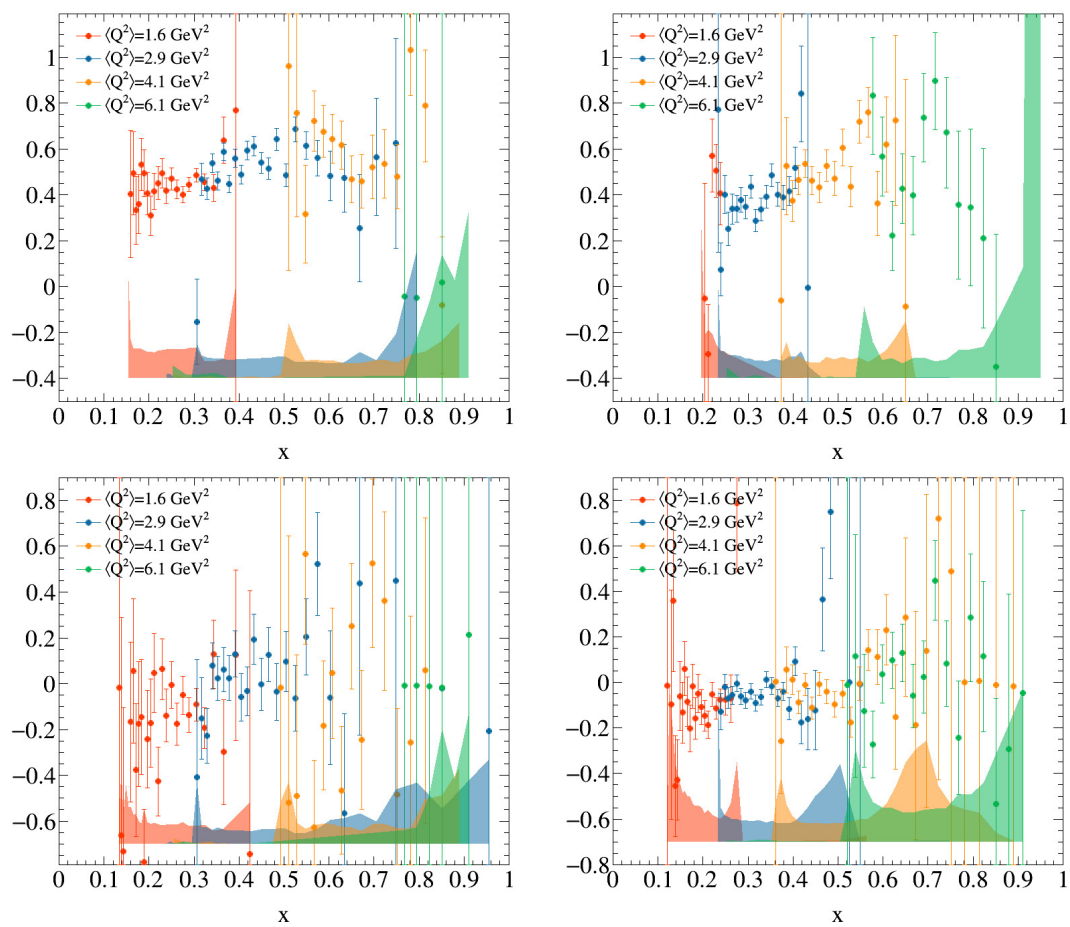


Figure 5.23.: Same as Figure 5.14 but with the inelastic radiative tail corrected.

CHAPTER 6

RESULTS

The final results of the experiment are presented here. Tables of results can be found appendix H. We begin by presenting the results for the virtual Compton asymmetries because they have the least model dependence in their extraction. The results of A_1 are compared to the world data, models, and predictions for high x . Then we will present the results for the spin structure functions g_1 and g_2 . From these results the dynamical twist-3 matrix element is determined. We will conclude with a discussion of the average color forces.

6.1 Virtual Compton Scattering Asymmetries

The corrected asymmetries found in Figure 5.23 are used to calculate A_1 and A_2 following equations A.20 and A.20. The SANE results are shown Figure against the world data for $8 > Q^2 > 1 \text{ GeV}^2$.

The behavior of A_1^p as $x \rightarrow 1$ is particularly interesting because there are a variety of model predictions. A recent calculation using the Dyson-Schwinger equation approach [72] provides a new and interesting test in addition to those of [73–76].

6.2 Spin Structure Functions

The spin structure functions were determined using equations A.16 and A.17 where an empirical fit was used for calculating F_1 [85, 86].

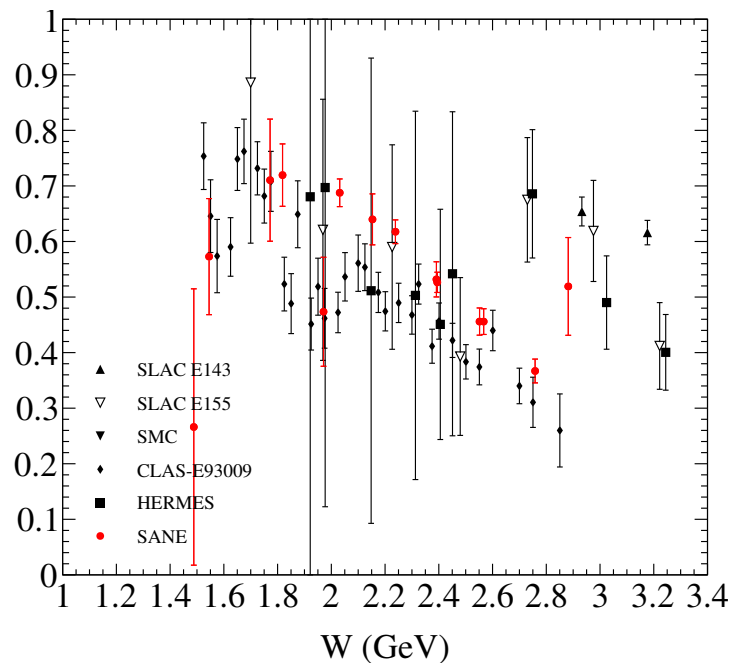


Figure 6.1.: The results for A_1^p . The data [77–82] shown is limited to the range $8 > Q^2 > 1 \text{ GeV}^2$.

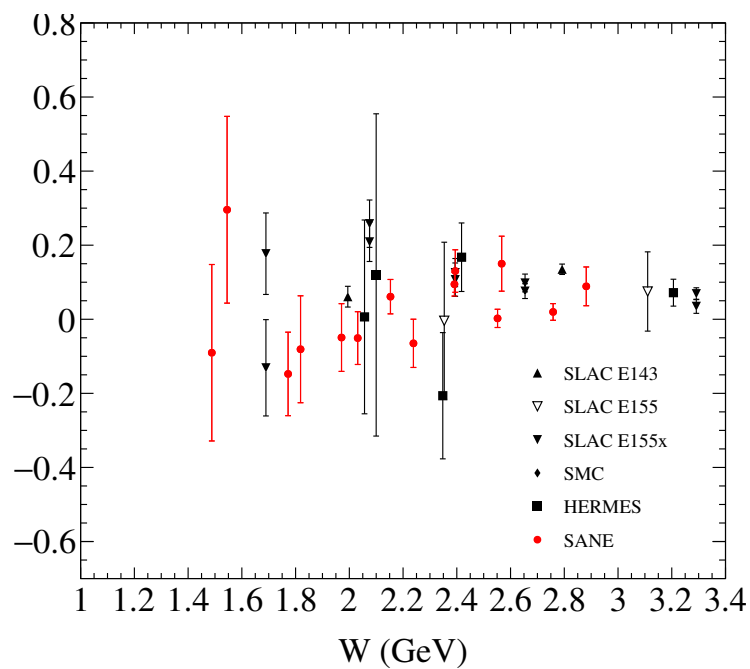


Figure 6.2.: The results for A_2^p . The data [43, 78, 80, 83, 84] shown is limited to the range $8 > Q^2 > 1 \text{ GeV}^2$.

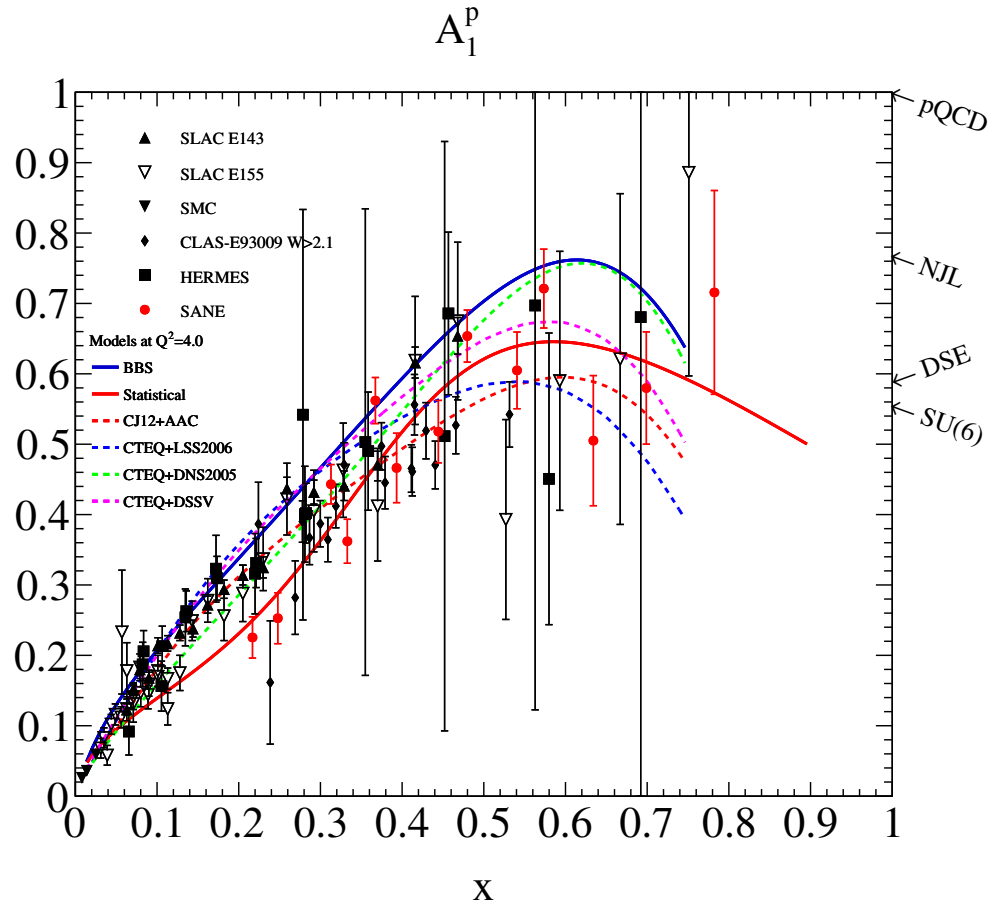


Figure 6.3.: The results for A_1^P vs Bjorken x with model predictions for $x \rightarrow 1$.

6.3 Twist-3 Matrix Element

The results for the Cornwall-Norton moment $I(Q^2) = \tilde{d}_2(Q^2) + \mathcal{O}(M^2/Q^2)$ are shown in Figure 6.6 along with a comparison to the existing measurements and lattice calculations. The results around $Q^2 = 5 \text{ GeV}^2$ are roughly in agreement with the lattice calculations [87]. It is an interesting feature that d_2 seems to be negative around $Q^2 \sim 3 \text{ GeV}^2$. This is also seen in the preliminary SANE analysis of the HMS [88].

A sizeable deviation from the pQCD calculation normalized to the SLAC data point with the elastic contribution added can be seen in Figure 6.6. However, at low Q^2 , target mass effects must be properly taken into account. This was done

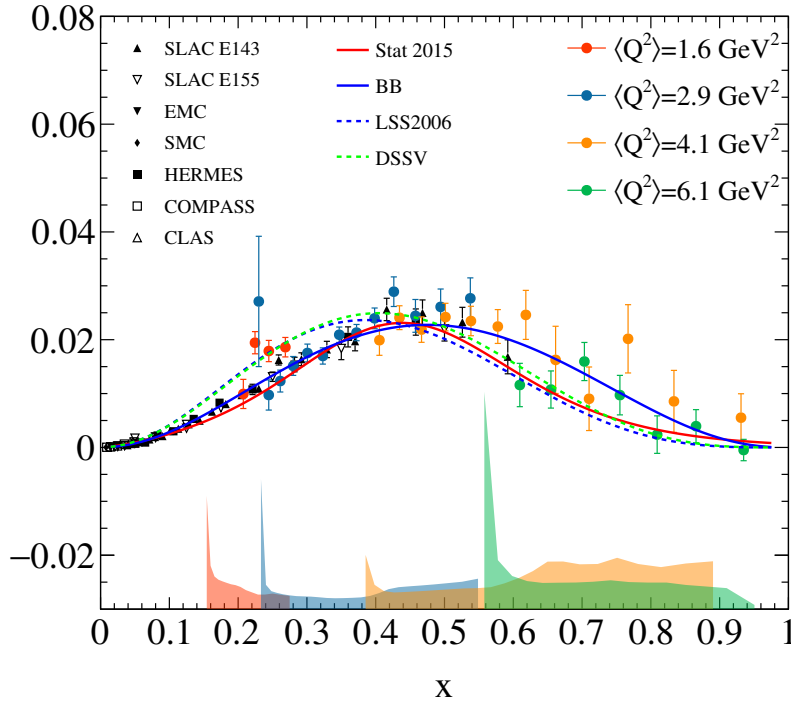


Figure 6.4.: The results for $x^2 g_1^p$.

by using Nachtmann moments (see appendix B.2.1). The Nachtmann moment extraction of $\tilde{d}_2(Q^2) = 2M_2^3(Q^2)$ is shown in Figure 6.7. While the improvement is consistent with numerical estimates of [89], there remains a notable difference that is consistent with a negative or zero value around $Q^2 = 3.0 \text{ GeV}^2$.

The statistical errors for the measured regions were conservatively calculated by summing the errors in quadrature. The unmeasured regions at low and high x were calculated from models. The uncertainties from these regions were added to the systematic uncertainty. Finally, the elastic contribution at $x = 1$ is calculated from models. It is rather model independent, but it worth noting that using the usual dipole form factors leads to an elastic contribution that remains positive for all Q^2 , while using empirical fits that include a two photon exchange correction [71] leads to a very slight negative value around $Q^2 \sim 3.5 \text{ GeV}^2$.

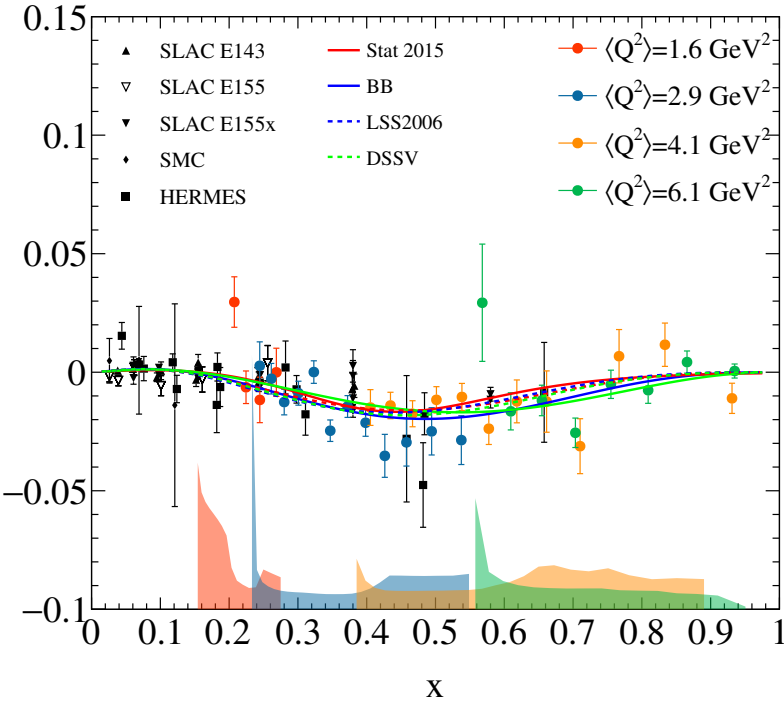


Figure 6.5.: The results for $x^2 g_2^p$.

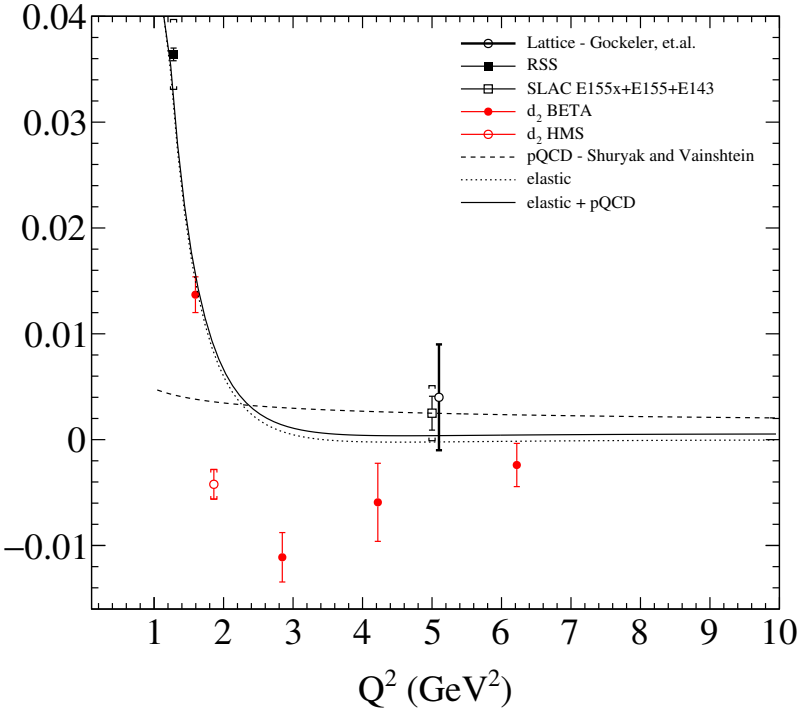


Figure 6.6.: The results for the CN moment extraction of $\tilde{d}_2^p = I(Q^2)$.

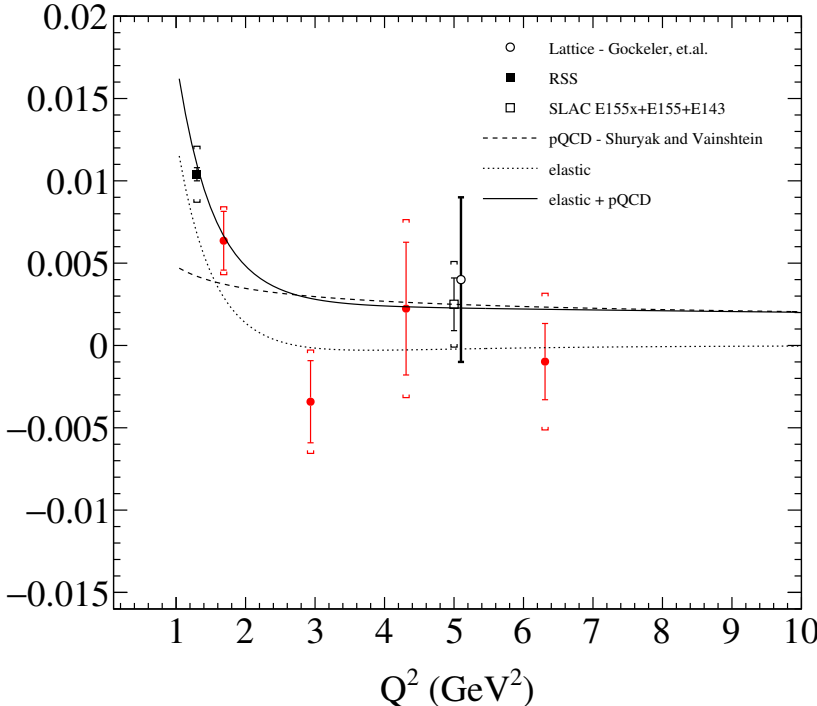


Figure 6.7.: The results of a Nachtmann moment extraction of $\tilde{d}_2^p = 2M_2^3$ shown against the existing data. [43, 44, 90]

CHAPTER 7

RECOMMENDATIONS

Precision measurements of d_2 on both the proton and neutron have the unique opportunity to study QCD confinement and color forces. However, there is a lack of high Q^2 data for g_1 and g_2 at high x . With the JLab 12 GeV program beginning, it is crucial that *precision* measurements, with both longitudinal *and transverse* target polarization, are conducted to map out the valence kinematics. A future electron-ion collider will also provide a great improvement at low x . Improving the quality of the low x data in the spin structure functions is important for managing the uncertainties of the first moments. This will enable a better separation of the average chromo electric and magnetic forces.

Lattice QCD calculations of d_2 have been neglected in recent years. Precise predictions of the Q^2 dependence of d_2 can provide a straightforward test of QCD.

REFERENCES CITED

- [1] E. Rutherford. The scattering of alpha and beta particles by matter and the structure of the atom. *Phil.Mag.*, 21:669–688, 1911.
- [2] J. Chadwick. Possible Existence of a Neutron. *Nature*, 129:312, 1932.
- [3] Luis W. Alvarez and F. Bloch. A Quantitative Determination of the Neutron Moment in Absolute Nuclear Magnetons. *Phys.Rev.*, 57:111–122, 1940.
- [4] Robert Hofstadter. Electron scattering and nuclear structure. *Rev.Mod.Phys.*, 28:214–254, 1956.
- [5] Murray Gell-Mann and Yuval Neemam. The Eightfold way: a review with a collection of reprints. 1964.
- [6] Richard E. Taylor. Inelastic electron - proton scattering in the deep continuum region. *Conf.Proc.*, C690914:251–260, 1969.
- [7] Elliott D. Bloom, D.H. Coward, H.C. DeStaebler, J. Drees, Guthrie Miller, et al. High-Energy Inelastic e p Scattering at 6-Degrees and 10-Degrees. *Phys.Rev.Lett.*, 23:930–934, 1969.
- [8] Richard E. Taylor. Deep inelastic scattering: The Early years. *Rev.Mod.Phys.*, 63:573–595, 1991.
- [9] Henry W. Kendall. Deep inelastic scattering: Experiments on the proton and the observation. *Rev.Mod.Phys.*, 63:597–614, 1991.
- [10] Jerome I. Friedman. Deep inelastic scattering: Comparisons with the quark model. *Rev.Mod.Phys.*, 63:615–629, 1991.
- [11] G. Zweig. An SU(3) model for strong interaction symmetry and its breaking. Version 1. 1964.
- [12] O.W. Greenberg. Spin and Unitary Spin Independence in a Paraquark Model of Baryons and Mesons. *Phys.Rev.Lett.*, 13:598–602, 1964.
- [13] H. Fritzsch, Murray Gell-Mann, and H. Leutwyler. Advantages of the Color Octet Gluon Picture. *Phys.Lett.*, B47:365–368, 1973.
- [14] David J. Gross and Frank Wilczek. Ultraviolet Behavior of Nonabelian Gauge Theories. *Phys.Rev.Lett.*, 30:1343–1346, 1973.
- [15] Jr. Callan, Curtis G. and David J. Gross. High-energy electroproduction and the constitution of the electric current. *Phys.Rev.Lett.*, 22:156–159, 1969.

- [16] R.P. Feynman. The behavior of hadron collisions at extreme energies. *Conf.Proc.*, C690905:237–258, 1969.
- [17] Richard P. Feynman. Very high-energy collisions of hadrons. *Phys.Rev.Lett.*, 23:1415–1417, 1969.
- [18] Matthias Burkardt. The $g(2)$ Structure Function. *AIP Conf.Proc.*, 1155:26–34, 2009.
- [19] A. Accardi, J.L. Albacete, M. Anselmino, N. Armesto, E.C. Aschenauer, et al. Electron Ion Collider: The Next QCD Frontier - Understanding the glue that binds us all. 2012.
- [20] N. F. Mott and H. S. W. Massey. *Theory of Atomic Collisions*. Oxford, 1965.
- [21] M.N. Rosenbluth. High Energy Elastic Scattering of Electrons on Protons. *Phys.Rev.*, 79:615–619, 1950.
- [22] K.A. Olive et al. Review of Particle Physics. *Chin.Phys.*, C38:090001, 2014.
- [23] M. Anselmino, A. Efremov, and E. Leader. The Theory and phenomenology of polarized deep inelastic scattering. *Phys.Rept.*, 261:1–124, 1995.
- [24] J.D. Bjorken and Emmanuel A. Paschos. Inelastic Electron Proton and gamma Proton Scattering, and the Structure of the Nucleon. *Phys.Rev.*, 185:1975–1982, 1969.
- [25] John R. Ellis and Robert L. Jaffe. A Sum Rule for Deep Inelastic Electroproduction from Polarized Protons. *Phys.Rev.*, D9:1444, 1974.
- [26] J. Ashman et al. A Measurement of the Spin Asymmetry and Determination of the Structure Function $g(1)$ in Deep Inelastic Muon-Proton Scattering. *Phys.Lett.*, B206:364, 1988.
- [27] Elliot Leader and Mauro Anselmino. A Crisis in the Parton Model: Where, Oh Where Is the Proton’s Spin? *Z.Phys.*, C41:239, 1988.
- [28] J.D. Bjorken. Applications of the Chiral $U(6) \times (6)$ Algebra of Current Densities. *Phys.Rev.*, 148:1467–1478, 1966.
- [29] J.D. Bjorken. Inelastic Scattering of Polarized Leptons from Polarized Nucleons. *Phys.Rev.*, D1:1376–1379, 1970.
- [30] V.N. Gribov and L.N. Lipatov. Deep inelastic $e p$ scattering in perturbation theory. *Sov.J.Nucl.Phys.*, 15:438–450, 1972.
- [31] Guido Altarelli and G. Parisi. Asymptotic Freedom in Parton Language. *Nucl.Phys.*, B126:298, 1977.
- [32] Yuri L. Dokshitzer. Calculation of the Structure Functions for Deep Inelastic Scattering and $e^+ e^-$ Annihilation by Perturbation Theory in Quantum Chromodynamics. *Sov.Phys.JETP*, 46:641–653, 1977.

- [33] F. Halzen and Alan D. Martin. QUARKS AND LEPTONS: AN INTRODUCTORY COURSE IN MODERN PARTICLE PHYSICS. 1984.
- [34] Johannes Blumlein. The Theory of Deeply Inelastic Scattering. *Prog.Part.Nucl.Phys.*, 69:28–84, 2013.
- [35] Claude Bourrely and Jacques Soffer. New developments in the statistical approach of parton distributions: tests and predictions up to LHC energies. 2015.
- [36] S.A. Larin, Paulo Nogueira, T. van Ritbergen, and J.A.M. Vermaseren. The Three loop QCD calculation of the moments of deep inelastic structure functions. *Nucl.Phys.*, B492:338–378, 1997.
- [37] Hugh Burkhardt and W.N. Cottingham. Sum rules for forward virtual Compton scattering. *Annals Phys.*, 56:453–463, 1970.
- [38] S. Wandzura and Frank Wilczek. Sum Rules for Spin Dependent Electroproduction: Test of Relativistic Constituent Quarks. *Phys.Lett.*, B72:195, 1977.
- [39] Johannes Blumlein and Avtandil Tkabladze. Target mass corrections for polarized structure functions and new sum rules. *Nucl.Phys.*, B553:427–464, 1999.
- [40] Alberto Accardi, Alessandro Bacchetta, W. Melnitchouk, and Marc Schlegel. What can break the Wandzura-Wilczek relation? *JHEP*, 0911:093, 2009.
- [41] Matthias Burkardt. Transverse Structure of Hadrons. pages 101–110, 2010.
- [42] Xiang-Dong Ji and W. Melnitchouk. Spin dependent twist four matrix elements from g1 data in the resonance region. *Phys.Rev.*, D56:1–5, 1997.
- [43] P.L. Anthony et al. Precision measurement of the proton and deuteron spin structure functions g(2) and asymmetries A(2). *Phys.Lett.*, B553:18–24, 2003.
- [44] Frank R. Wesselmann et al. Proton spin structure in the resonance region. *Phys.Rev.Lett.*, 98:132003, 2007.
- [45] K. Slifer et al. Probing Quark-Gluon Interactions with Transverse Polarized Scattering. *Phys.Rev.Lett.*, 105:101601, 2010.
- [46] M. Gockeler, R. Horsley, D. Pleiter, Paul E.L. Rakow, A. Schafer, et al. Investigation of the second moment of the nucleon’s g(1) and g(2) structure functions in two-flavor lattice QCD. *Phys.Rev.*, D72:054507, 2005.
- [47] C.W. Leemann, D.R. Douglas, and G.A. Krafft. The Continuous Electron Beam Accelerator Facility: CEBAF at the Jefferson Laboratory. *Ann.Rev.Nucl.Part.Sci.*, 51:413–450, 2001.
- [48] T.B. Humensky, R. Alley, A. Brachmann, M.J. Browne, J. Clendenin, et al. SLAC’s polarized electron source laser system and minimization of electron beam helicity correlations for the E-158 parity violation experiment. *Nucl.Instrum.Meth.*, A521:261–298, 2004.

- [49] T. Maruyama, A. Brachmann, J.E. Clendenin, T. Desikan, Edward L. Garwin, et al. A Very high charge, high polarization gradient doped strained GaAs photocathode. *Nucl.Instrum.Meth.*, A492:199–211, 2002.
- [50] C. Yan, P. Adderley, D. Barker, J. Beaufait, K. Capek, et al. Superharp: A Wire scanner with absolute position readout for beam energy measurement at CEBAF. *Nucl.Instrum.Meth.*, A365:261–267, 1995.
- [51] C. Yan, R. Carlini, and D. Neuffer. Beam energy measurement using the Hall C beamline. *Conf.Proc.*, C930517:2136–2138, 1993.
- [52] John Robert Arrington. Inclusive electron scattering from nuclei at $x \lesssim 1$ and high 4-momentum. 1998.
- [53] M. Hauger, A. Honegger, J. Jourdan, G. Kubon, T. Petitjean, et al. A High precision polarimeter. *Nucl.Instrum.Meth.*, A462:382–392, 2001.
- [54] C. Yan, P. Adderley, R. Carlini, C. Cuevas, W. Vulcan, et al. Target raster system at CEBAF. *Nucl.Instrum.Meth.*, A365:46–48, 1995.
- [55] Chen Yan. Hall c user howto: Slow raster system for polarized target experiments, 2008.
- [56] James Maxwell. Probing Proton Spin Structure: A Measurement of $g(2)$ at Four-momentum Transfer of 2 to 6 GeV^2 . 2011.
- [57] D.G. Crabb and W. Meyer. Solid polarized targets for nuclear and particle physics experiments. *Ann.Rev.Nucl.Part.Sci.*, 47:67–109, 1997.
- [58] T.D. Averett, D.G. Crabb, D.B. Day, T.J. Liu, J.S. McCarthy, et al. A Solid polarized target for high luminosity experiments. *Nucl.Instrum.Meth.*, A427:440–454, 1999.
- [59] Joshua Pierce, James Maxwell, Toby Badman, James Brock, Christopher Carlin, et al. Dynamically polarized target for the g_2^p and G_E^p experiments at Jefferson Lab. *Nucl.Instrum.Meth.*, A738:54–60, 2014.
- [60] D.J. Hamilton et al. Polarization transfer in proton Compton scattering at high momentum transfer. *Phys.Rev.Lett.*, 94:242001, 2005.
- [61] Whitney R. Armstrong, Seonho Choi, Ed Kaczanowicz, Alexander Lukhanin, Zein-Eddine Meziani, et al. A Threshold Gas Čerenkov Detector for the Spin Asymmetries of the Nucleon Experiment. 2015.
- [62] P. Banta, J. Chen, W.G. Heyes, E. Jastrzembski, C. Timmer, et al. The Front end readout control software for the CODA data acquisition toolkit. 1997.
- [63] M. Knott, D. Gurd, S. Lewis, and M. Thuot. EPICS: A Control system software codevelopment success story. *Nucl.Instrum.Meth.*, A352:486–491, 1994.
- [64] R. Brun and F. Rademakers. ROOT: An object oriented data analysis framework. *Nucl.Instrum.Meth.*, A389:81–86, 1997.

- [65] W.R. Armstrong. Insane. <http://quarks.temple.edu/~whit/code/InSANE++/html/>, June 2011. SANE.
- [66] S. Agostinelli et al. GEANT4: A Simulation toolkit. *Nucl.Instrum.Meth.*, A506:250–303, 2003.
- [67] W.R. Armstrong. Betag4. <http://quarks.temple.edu/~whit/code/BETAG4/html/>, June 2011. Geant-4 Simulation.
- [68] Oscar Rondon. Inclusive Photo- and Electro-production of Pions on Nuclei. 2015.
- [69] Luke W. Mo and Yung-Su Tsai. Radiative Corrections to Elastic and Inelastic $e p$ and μp Scattering. *Rev.Mod.Phys.*, 41:205–235, 1969.
- [70] I.V. Akushevich and N.M. Shumeiko. Radiative effects in deep inelastic scattering of polarized leptons by polarized light nuclei. *J.Phys.*, G20:513–530, 1994.
- [71] J. Arrington, W. Melnitchouk, and J.A. Tjon. Global analysis of proton elastic form factor data with two-photon exchange corrections. *Phys.Rev.*, C76:035205, 2007.
- [72] Craig D. Roberts, Roy J. Holt, and Sebastian M. Schmidt. Nucleon spin structure at very high x . *Phys.Lett.*, B727:249–254, 2013.
- [73] Frank E. Close and Anthony William Thomas. The Spin and Flavor Dependence of Parton Distribution Functions. *Phys.Lett.*, B212:227, 1988.
- [74] E.W. Hughes and R. Voss. Spin structure functions. *Ann.Rev.Nucl.Part.Sci.*, 49:303–339, 1999.
- [75] Nathan Isgur. Valence quark spin distribution functions. *Phys.Rev.*, D59:034013, 1999.
- [76] Stanley J. Brodsky, Matthias Burkardt, and Ivan Schmidt. Perturbative QCD constraints on the shape of polarized quark and gluon distributions. *Nucl.Phys.*, B441:197–214, 1995.
- [77] K.V. Dharmawardane et al. Measurement of the x - and Q^{*2} -dependence of the asymmetry $A(1)$ on the nucleon. *Phys.Lett.*, B641:11–17, 2006.
- [78] P.L. Anthony et al. Measurements of the Q^{*2} dependence of the proton and neutron spin structure functions $g(1)^{*p}$ and $g(1)^{*n}$. *Phys.Lett.*, B493:19–28, 2000.
- [79] A. Airapetian et al. Precise determination of the spin structure function $g(1)$ of the proton, deuteron and neutron. *Phys.Rev.*, D75:012007, 2007.
- [80] K. Abe et al. Measurements of the proton and deuteron spin structure functions $g(1)$ and $g(2)$. *Phys.Rev.*, D58:112003, 1998.
- [81] B. Adeva et al. The Spin dependent structure function $g(1)(x)$ of the proton from polarized deep inelastic muon scattering. *Phys.Lett.*, B412:414–424, 1997.

- [82] J. Ashman et al. An Investigation of the Spin Structure of the Proton in Deep Inelastic Scattering of Polarized Muons on Polarized Protons. *Nucl.Phys.*, B328:1, 1989.
- [83] D. Adams et al. Spin structure of the proton from polarized inclusive deep inelastic muon - proton scattering. *Phys.Rev.*, D56:5330–5358, 1997.
- [84] A. Airapetian et al. Measurement of the virtual-photon asymmetry A_2 and the spin-structure function g_2 of the proton. *Eur.Phys.J.*, C72:1921, 2012.
- [85] M.E. Christy and Peter E. Bosted. Empirical fit to precision inclusive electron-proton cross- sections in the resonance region. *Phys.Rev.*, C81:055213, 2010.
- [86] P.E. Bosted and M.E. Christy. Empirical fit to inelastic electron-deuteron and electron-neutron resonance region transverse cross-sections. *Phys.Rev.*, C77:065206, 2008.
- [87] M. Gockeler, R. Horsley, W. Kurzinger, H. Oelrich, D. Pleiter, et al. A Lattice calculation of the nucleon’s spin dependent structure function $g(2)$ revisited. *Phys.Rev.*, D63:074506, 2001.
- [88] Hoyoung Kang. *Proton spin asymmetries and d_2 from SANE-HMS data*. PhD thesis, Seoul National University, Seoul, Korea, 2014.
- [89] Y.B. Dong. Twist-3 effects and target mass corrections. *Phys.Rev.*, C77:015201, 2008.
- [90] M. Osipenko, S. Simula, W. Melnitchouk, Peter E. Bosted, V. Burkert, et al. Global analysis of data on the proton structure function $g(1)$ and extraction of its moments. *Phys.Rev.*, D71:054007, 2005.
- [91] L.N. Hand. Experimental investigation of pion electroproduction. *Phys.Rev.*, 129:1834–1846, 1963.
- [92] Jacques Soffer and O.V. Teryaev. Positivity constraints and flavor dependence of higher twists. *Phys.Lett.*, B490:106–110, 2000.
- [93] Kenneth G. Wilson. Nonlagrangian models of current algebra. *Phys.Rev.*, 179:1499–1512, 1969.
- [94] Richard A. Brandt and Giuliano Preparata. Operator product expansions near the light cone. *Nucl.Phys.*, B27:541–567, 1972.
- [95] Norman H. Christ, B. Hasslacher, and Alfred H. Mueller. Light cone behavior of perturbation theory. *Phys.Rev.*, D6:3543, 1972.
- [96] David J. Gross and S.B. Treiman. Light cone structure of current commutators in the gluon quark model. *Phys.Rev.*, D4:1059–1072, 1971.
- [97] Jiro Kodaira, Satoshi Matsuda, Ken Sasaki, and T. Uematsu. QCD Higher Order Effects in Spin Dependent Deep Inelastic Electroproduction. *Nucl.Phys.*, B159:99, 1979.
- [98] J. Kodaira, S. Matsuda, T. Muta, K. Sasaki, and T. Uematsu. QCD Effects in Polarized Electroproduction. *Phys.Rev.*, D20:627, 1979.

- [99] Satoshi Matsuda and Tsuneo Uematsu. Target Mass Effects in Polarized Electroproduction. *Nucl.Phys.*, B168:181, 1980.
- [100] Andrea Piccione and Giovanni Ridolfi. Target mass effects in polarized deep inelastic scattering. *Nucl.Phys.*, B513:301–316, 1998.
- [101] R.L. Jaffe. $G(2)$: The Nucleon’s Other Spin Dependent Structure Function. *Comments Nucl.Part.Phys.*, 19:239, 1990.
- [102] Ingo Schienbein, Voica A. Radescu, G.P. Zeller, M. Eric Christy, C.E. Keppel, et al. A Review of Target Mass Corrections. *J.Phys.*, G35:053101, 2008.
- [103] Vladimir M. Braun, G.P. Korchemsky, and A.N. Manashov. Evolution equation for the structure function $g(2)(x, Q^{*2})$. *Nucl.Phys.*, B603:69–124, 2001.
- [104] R. Byrd, P. Lu, J. Nocedal, and C. Zhu. A limited memory algorithm for bound constrained optimization. *SIAM Journal on Scientific Computing*, 16(5):1190–1208, 1995.
- [105] R.T. Jones, M. Kornicer, A. Dzierba, J.L. Gunter, R. Lindenbusch, et al. A bootstrap method for gain calibration and resolution determination of a lead-glass calorimeter. *Nucl.Instrum.Meth.*, A566:366–374, 2006.
- [106] Anusha Liyanage. Elastic events / asymmetry. SANE Wiki, March 2011. wiki.
- [107] Hovhannes Baghdasaryan. Corrections and results, 2012.
- [108] Yung-Su Tsai. RADIATIVE CORRECTIONS TO ELECTRON SCATTERINGS. 1971.
- [109] S. Stein, W.B. Atwood, Elliott D. Bloom, R. Leslie Cottrell, H.C. DeStaebler, et al. Electron Scattering at 4-Degrees with Energies of 4.5-GeV - 20-GeV. *Phys.Rev.*, D12:1884, 1975.
- [110] C. Maieron, T.W. Donnelly, and Ingo Sick. Extended superscaling of electron scattering from nuclei. *Phys.Rev.*, C65:025502, 2002.
- [111] T.V. Kukhto and N.M. Shumeiko. RADIATIVE EFFECTS IN DEEP INELASTIC SCATTERING OF POLARIZED LEPTONS BY POLARIZED NUCLEONS. *Nucl.Phys.*, B219:412–436, 1983.
- [112] N.M. Shumeiko and S.I. Timoshin. The Lowest order total electromagnetic correction to the deep inelastic scattering of polarized leptons on polarized nucleons. *J.Phys.*, G17:1145–1157, 1991.
- [113] I. Akushevich, A. Ilyichev, N. Shumeiko, A. Soroko, and A. Tolkachev. POLARD 2.0 FORTRAN code for the radiative corrections calculation to deep inelastic scattering of polarized particles. *Comput.Phys.Commun.*, 104:201–244, 1997.
- [114] Haakon Olsen and L.C. Maximon. Photon and Electron Polarization in High-Energy Bremsstrahlung and Pair Production with Screening. *Phys.Rev.*, 114:887–904, 1959.

- [115] Roy Whitney. Radcor fortran code. Private Communnication.
- [116] Karl Slifer. nradcor.
- [117] David Flay. Radcor run for sane kinematics. Private Communnication.

APPENDIX A

VIRTUAL COMPTON SCATTERING ASYMMETRIES

Within the one photon exchange approximation, the electron momenta (k and k') define a virtual photon which is absorbed by the struck parton. Using the optical theorem the hadronic tensor can be related to the absorptive part of the forward virtual Compton scattering amplitude by

$$W_{\mu\nu}(\nu, Q^2) = \frac{1}{2\pi M} \text{Im} T_{\mu\nu}(\nu, Q^2). \quad (\text{A.1})$$

The four possible amplitudes for a photons with transverse and longitudinal polarizations scattering from a spin 1/2 target are written as in terms of their initial and final state photon (λ and λ') and target (S and S') polarizations as $\mathcal{M}(\lambda', S \rightarrow \lambda, S')$. They are defined with respect to the virtual photon cross sections

$$\frac{4\pi^2\alpha}{K} \mathcal{M}(1, -\frac{1}{2} \rightarrow 1, -\frac{1}{2}) \sim \sigma_{1/2}^T = \frac{4\pi^2\alpha}{K} \frac{1}{M} (F_1 + g_1 - \gamma^2 g_2) \quad (\text{A.2})$$

$$\frac{4\pi^2\alpha}{K} \mathcal{M}(1, \frac{1}{2} \rightarrow 1, \frac{1}{2}) \sim \sigma_{3/2}^T = \frac{4\pi^2\alpha}{K} \frac{1}{M} (F_1 - g_1 + \gamma^2 g_2) \quad (\text{A.3})$$

$$\frac{4\pi^2\alpha}{K} \mathcal{M}(1, -\frac{1}{2} \rightarrow 0, \frac{1}{2}) \sim \sigma_{1/2}^{TL} = \sigma'_{LT} = \frac{4\pi^2\alpha}{K} \frac{\gamma}{M} (g_1 + g_2) \quad (\text{A.4})$$

$$\frac{4\pi^2\alpha}{K} \mathcal{M}(0, \frac{1}{2} \rightarrow 0, \frac{1}{2}) \sim \sigma_{1/2}^L = \frac{4\pi^2\alpha}{K} \frac{1}{M\nu} \left(M \left(1 + \frac{1}{\gamma^2} \right) F_2 - \nu F_1 \right) \quad (\text{A.5})$$

where the first amplitude corresponds to the photon flipping the target spin when absorbed and then flipping back when emitting the final state photon. Similarly, the second amplitude describes an intermediate state with spin 3/2

and is therefore suppressed compared to the previous. The last two involve a longitudinally polarized photon.

Following the Hand convention [91], the virtual photon flux is

$$\Gamma = \frac{\alpha}{2\pi} \frac{E'}{E} \frac{K}{Q^2} \frac{1}{1 - \epsilon} \quad (\text{A.6})$$

where $K = \nu - Q^2/2M$. The electron scattering cross section is then

$$\frac{d\sigma}{d\Omega dE'} = \Gamma \left(\sigma_T + \epsilon\sigma_L + \lambda P_{\perp} \sqrt{2\epsilon(1 - \epsilon)} \sigma'_{LT} + \lambda P_{\parallel} \sqrt{1 - \epsilon^2} \sigma'_{TT} \right). \quad (\text{A.7})$$

where ϵ is the longitudinal polarization of the virtual photon given by 2.9. The total photo absorption cross sections are

$$\sigma_L \equiv \sigma_{1/2}^L \quad (\text{A.8})$$

for incident longitudinal photons, and

$$\sigma_T = \frac{1}{2} (\sigma_{1/2}^T + \sigma_{3/2}^T) \quad (\text{A.9})$$

$$= \frac{4\pi^2\alpha}{K} \frac{F_1}{M} \quad (\text{A.10})$$

for transverse photons. The following cross section difference is called the transverse-transverse cross section

$$\sigma'_{TT} = \frac{1}{2} (\sigma_{1/2}^T - \sigma_{3/2}^T) \quad (\text{A.11})$$

$$= \frac{4\pi^2\alpha}{K} \frac{g_1 - \gamma^2 g_2}{2M} \quad (\text{A.12})$$

even though it is a difference, however, due to the amplitude arguments outlined above, it should always be positive, therefore calling it a cross section is somewhat justified. The ratio of the longitudinal to transverse cross section is

$$R \equiv \frac{\sigma_L}{\sigma_T} = \frac{F_L}{2xF_1} = \frac{F_2}{2xF_1} \left(1 + \frac{4M^2x^2}{Q^2} \right) - 1. \quad (\text{A.13})$$

Finally, the virtual photon scattering Compton asymmetries are defined as

$$A_1 = \frac{\sigma_{1/2}^T - \sigma_{3/2}^T}{\sigma_{1/2}^T + \sigma_{3/2}^T} \quad (\text{A.14})$$

and

$$A_2 = \frac{\sigma_{1/2}^{TL}}{\sigma_{1/2}^T + \sigma_{3/2}^T}. \quad (\text{A.15})$$

They are given in terms of the structure functions as

$$A_1 = \frac{1}{F_1} (g_1 - \gamma^2 g_2) \quad (\text{A.16})$$

and

$$\begin{aligned} A_2 &= \frac{\gamma}{F_1} (g_1 + g_2) \\ &= \frac{\gamma}{F_1} g_T \end{aligned} \quad (\text{A.17})$$

where we have introduced the transverse spin structure function $g_T = g_1 + g_2$.

$$R \equiv \frac{\sigma_L}{\sigma_T} = \frac{F_2}{2xF_1} \left(1 + \frac{4M^2x^2}{Q^2} \right) - 1 \quad (\text{A.18})$$

A.1 Extracting Virtual Compton Scattering Asymmetries

This experiment measured A_{80} and A_{180} . Ideally we would want to measure $A_{90} = A_{\perp}$ instead of A_{80} but the experimental apparatus makes this prohibitively difficult. The virtual Compton Scattering asymmetries can be expressed as

$$A_1 = \left(\frac{1}{1 + \eta\xi} \right) \left[A_{180} \left(\frac{\xi - \cot(\alpha)\chi}{D} \right) + A_{\alpha} \left(\frac{\csc(\alpha)\chi}{D} \right) \right] \quad (\text{A.19})$$

and

$$A_2 = \left(\frac{1}{1 + \eta\xi} \right) \left[A_{180} \left(\frac{\xi - \cot(\alpha)\chi/\eta}{D} \right) + A_{\alpha} \left(\frac{\xi - \cot(\alpha)\chi/\eta}{D(\cos(\alpha) - \sin(\alpha) \cos^2(\phi)\chi)} \right) \right] \quad (\text{A.20})$$

where

$$D = \frac{E - \epsilon E'}{E(1 + \epsilon R)} \quad (\text{A.21})$$

$$\eta = \frac{\epsilon \sqrt{Q^2}}{E - \epsilon E'} \quad (\text{A.22})$$

$$\xi = \eta \frac{1 + \epsilon}{2\epsilon} \quad (\text{A.23})$$

$$\chi = \frac{E' \sin(\theta) \sec(\phi)}{E - E' \cos(\theta)} \quad (\text{A.24})$$

and the angles are as defined in Figure 2.7. As expected, for $\alpha = 90^\circ$ these equations reduce to

$$A_1 = \frac{1}{1 + \eta\xi} \left(\frac{A_{\parallel}}{D} - \frac{\eta A_{\perp}}{d} \right) \quad (\text{A.25})$$

$$A_2 = \frac{1}{1 + \eta\xi} \left(\frac{\xi A_{\parallel}}{D} + \frac{A_{\perp}}{d} \right) \quad (\text{A.26})$$

which are equivalent to equations 2.46 and 2.47.

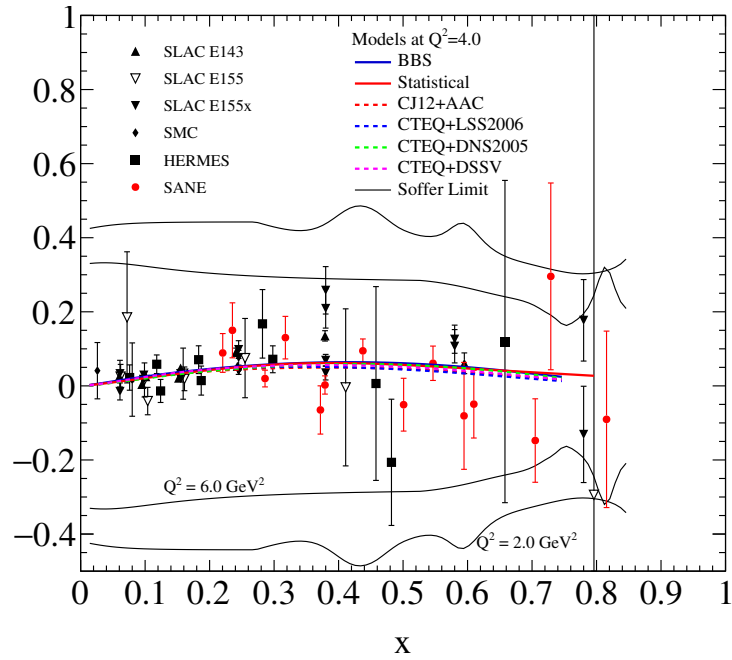


Figure A.1.: The results for A_2^p . The data [43, 78, 80, 83, 84] shown is limited to the range $8 > Q^2 > 1 \text{ GeV}^2$. Also shown is the Soffer limit [92] for two $Q^2 = 2$ and 6 GeV^2 .

APPENDIX B

OPERATOR PRODUCT EXPANSION

The structure functions are related to the absorptive part of the forward virtual Compton scattering amplitude (see A),

$$T_{\mu\nu}(q; P, S) = i \int d^4x e^{iq \cdot x} \langle P, S | T[J_\mu(x), J_\nu(0)] | P, S \rangle. \quad (\text{B.1})$$

Within the light cone expansion [93–95], and in the Bjorken limit, the time ordered product of non-local operators can be expressed as a sum of local operators

$$\lim_{\text{Bjorken}} T[J(x), J(0)] \sim \sum_{i, N, \tau} C_{i, \tau}^N q_{\mu_1} \dots q_{\mu_N} O_{i, \tau}^{\mu_1, \dots, \mu_N} \quad (\text{B.2})$$

where q_μ are general currents, $C_{i, \tau}^N$ are the Wilson coefficients, $O_{i, \tau}^{\mu_1, \dots, \mu_N}$ are local operators, i is a flavor index, and τ is the twist. Near the light cone the importance of an operator is determined by their *twist* [96] which is the dimension minus the spin of an operator.

Expanding in terms of the local operators, $R_{(1,2),i}(0)$, and in inverse powers of Q^2 , the antisymmetric part of equation B.1 becomes [23]

$$\begin{aligned} i \int d^4x e^{iq \cdot x} T[J_\mu(x) J_\nu(0)] &= -i \sum_{n=1} \left(\frac{1 - (-1)^n}{2} \right) \times \left(\frac{2}{Q^2} \right)^n q_{\mu_1} \dots q_{\mu_{n-2}} \sum_i \delta_i \\ &\times \left[\varepsilon_{\mu\nu\lambda\sigma} q^\lambda q_{\mu_{n-1}} E_{1,i}^n(Q^2, g) R_{1,i}^{\sigma\mu_1 \dots \mu_{n-1}} \right. \\ &\quad \left. + (\varepsilon_{\mu\rho\lambda\sigma} q_\nu q_\rho - \varepsilon_{\mu\rho\lambda\sigma} q_\mu q_\rho - q^2 \varepsilon_{\mu\rho\lambda\sigma}) \right. \\ &\quad \left. \frac{n-1}{n} E_{2,i}^n(Q^2, g) R_{2,i}^{\lambda\sigma\mu_1 \dots \mu_{n-2}} \right] \end{aligned} \quad (\text{B.3})$$

where $E_{1,2}$ are the Wilson coefficient functions and $R_{1,2}$ are the composite local operators. For electromagnetic currents

$$\begin{aligned}
\delta_1 &= \frac{1}{3} \\
\delta_8 &= \frac{1}{3\sqrt{3}} \\
\delta_\psi &= \frac{2}{9} \\
\delta_G &= \frac{2}{9} \\
\delta_{2,\dots,7} &= 0
\end{aligned} \tag{B.4}$$

which reflect the charge and isospin structure of the currents. The coefficient functions come from pQCD and local operators contain quark and gluon fields which we are interested in studying. More details of this operator product expansion can be found in [23, 34, 97–99].

B.1 Nucleon Matrix Elements

The irreducible Lorentz operators appearing in equation B.3 come in the form of flavor singlets and non-singlets. The R_1 operators are the leading twist ($\tau = 2$) operators and R_2 are the twist three operators. The proton matrix elements of these operators are

$$\langle P, S | R_{1,i}^{\sigma\mu_1 \dots \mu_{n-1}} | P, S \rangle = -2M a_n^i [S^\sigma P^{\mu_1} \dots P^{\mu_{n-1}}]_s \tag{B.5}$$

and

$$\langle P, S | R_{2,i}^{\lambda\sigma\mu_1 \dots \mu_{n-2}} | P, S \rangle = M d_n^i [(S^\sigma P^\lambda - S^\lambda P^\sigma) P^{\mu_1} \dots P^{\mu_{n-2}}]_{ms} \tag{B.6}$$

where we have introduced the reduced matrix elements a_n^i and d_n^i , and the index $i = 1, \dots, 8$ indicates the flavor non-singlet operators and $i = \psi, G$ the flavor singlet operators (see [23] for more discussion of these operators). The s in B.5

denotes symmetrization of the Lorentz indices and division by n while the ms in B.6 means a mixed symmetry where the tensor should be antisymmetric in (λ, σ) , but symmetric in all other indices [100].

The reduced matrix elements encapsulate the unknown non-perturbative dynamics we wish to better understand.

B.2 Moments

Applying the operator product expansion leads to an infinite set of sum rules for the spin structure functions. The Mellin moments of the spin structure functions are related to the reduced matrix elements [97] by

$$\int_0^1 dx x^{n-1} g_1(x, Q^2) = a_n E_1^n(Q^2) \quad n=1,3,5,\dots \quad (\text{B.7})$$

and

$$\int_0^1 dx x^{n-1} g_2(x, Q^2) = -\frac{n-1}{n} [a_n E_1^n(Q^2) - d_n E_2^n(Q^2)] \quad n=3,5,7,\dots \quad (\text{B.8})$$

where we have summed over all flavor combinations.

Combining the equations above for $n \geq 3$ and n odd, we have

$$\int_0^1 dx x^{n-1} \left\{ g_1 + \frac{n}{n-1} g_2 \right\} = \frac{1}{2} d_n E_2^n(Q^2) . \quad (\text{B.9})$$

For $n = 3$ the result is

$$\begin{aligned} I(Q^2) &\equiv \int_0^1 dx x^2 [2g_1(x, Q^2) + 3g_2(x, Q^2)] \\ &= 2d_3 + \mathcal{O}(M^2/Q^2) \\ &= \tilde{d}_2 + \mathcal{O}(M^2/Q^2) \end{aligned} \quad (\text{B.10})$$

where \tilde{d}_2 is the twist-3 matrix element. It should be noted that we are using the notation of Piccione and Ridolfi [100] whereas the matrix elements are sometimes [101] written as $a'_{n-1} = \tilde{a}_n$ and $d'_{n-1} = \tilde{d}_n$ (i.e. without the prime) which can cause some confusion.

B.2.1 Target Mass Corrections

At large Q^2 the leading term in the twist expansion (equation 3.20) as a good approximation, but at lower values terms of order $\mathcal{O}(M^2/Q^2)$ become increasingly important. It is common, even at only moderate values of momentum transfer such as $Q^2 \sim 5 \text{ GeV}^2$, to let $M \rightarrow 0$. In this case the parton distributions have a clean interpretation (as it always is in the Bjorken limit) and the moments are calculated as Cornwall-Norton (CN) moments, which are just the moments integrated over the Bjorken x variable, as done in the previous section. At lower scales the target mass cannot be neglected and therefore target mass corrections (TMCs) are needed. For the unpolarized structure functions an extensive review of TMCs can be found in [102].

At low Q^2 , Nachtmann moments should be used instead of the CN moments. The Nachtmann moments are [99, 100]

$$\begin{aligned} M_1^{(n)} &\equiv \frac{1}{2} \tilde{a}_{n-1} \\ &= \int_0^1 dx \frac{\xi^{n+1}}{x^2} \left(\left[\frac{x}{\xi} - \frac{n^2}{(n+2)^2} y^2 x \xi \right] g_1(x, Q^2) - y^2 x^2 \frac{4n}{n+2} g_2(x, Q^2) \right) \end{aligned} \quad (\text{B.11})$$

and

$$\begin{aligned} M_2^{(n)} &\equiv \frac{1}{2} \tilde{d}_{n-1} \\ &= \int_0^1 dx \frac{\xi^{n+1}}{x^2} \left(\frac{x}{\xi} g_1(x, Q^2) + \left[\frac{n}{n-1} \frac{x^2}{\xi^2} - \frac{n}{n+1} y^2 x^2 \right] g_2(x, Q^2) \right). \end{aligned} \quad (\text{B.12})$$

When the target mass is neglected, i.e. $M \rightarrow 0$, then these equations reduce to $M_1^1 = \Gamma_1$ and $I = 2M_2^3$.

While the Nachtmann moments treat target mass effects at the level of the moments, the x dependence of the twist-3 contribution to g_1 [39] shows up as a target mass correction through equation 3.29.

B.2.2 Twist-3 Evolution Equations

From the work of Braun, et.al. [103], we have the (approximate) evolution of g_2

$$g_2^{\tau-3}(x, Q^2) = \frac{1}{2} \sum_q e_q^2 \int_x^1 \frac{dy}{y} [\Delta q_T(y) + \Delta \bar{q}_T(-y)] \quad (\text{B.13})$$

$$+ (Evolution)(x, Q^2) \quad (\text{B.14})$$

In the previous two equations we have simplified their form which is actually the DGLAP equations (which also involve the gluon distributions). In [103] they also show that g_2 can be evolved as a non-singlet distribution due to the very small gluon contribution in the large N_c approximation.

$$\frac{d}{d \ln Q^2} g_2^{NS}(x, Q^2) = \frac{\alpha_s(Q^2)}{4\pi} \left(\int_x^1 \frac{dz}{z} P^{NS}(x/z) g_2^{NS}(z, Q^2) \right) \quad (\text{B.15})$$

Ignoring contributions beyond twist-3 effects, we see that $g_1(x)$ and $g_2(x)$ are defined when Δq and Δq_T are defined at an input scale Q_0^2 .

$$g_2^{\tau-3}(x, Q^2) = g_2^{exp}(x, Q^2) - g_2^{\tau-2}(x, Q^2) \quad (\text{B.16})$$

$\text{TMC}(x,^2)$ represents the target mass corrections which in the massless limit only contribute to g_2 [39]

APPENDIX C

ARTIFICIAL NEURAL NETWORKS

C.1 Network Training

Training a *good* artificial neural networks can be quite difficult and hazardous if care is not taken. The quality of the network depends on the quality of the training data set, the selected input neurons, the number of hidden layers, the number of hidden neurons, the number of training iterations, the size of the training data set, the neuron activation function, and training method used. There is no straightforward procedure to construct and train networks, however, for our purposes we follow a few good rules of thumb.

- In feed forward networks extra hidden layers are equivalent to adding more neurons in a single layer. Therefore, we use only one single layer and vary the number of hidden neurons.
- The proper number of hidden layer neurons is determined by a series of trials. The number of neurons is determined when the network output no longer varies with a small change in this number.
- Input neurons which have little impact on the output are removed.
- Several trainings are performed in order to avoid the possibility of arriving at local minima.

We use the Broyden, Fletcher, Goldfarb, Shanno (BFGS) [104] training method throughout with a sigmoid activation function for all neurons. The resulting network is considered stable when varying the network structure does not change the outcome.

The training datasets for the neural networks is from a GEANT4 [66] developed for the experiment. It included all detectors, magnetic field, and target materials [67].

C.2 Overview of Networks

This analysis made use of a few types of neural networks in order to reconstruct tracks. A neural network was trained for each relevant particle type and to provide one specific piece of the event reconstruction. Three types of neural networks were constructed for this analysis. This compartmentalization of the neural networks permits a better and more intuitive understanding of their behavior and quality than a one-shot approach in reconstruction.

The first network provided a position correction for the cluster's X-Y position such that the corrected position was the location in the front plane that the track entered the calorimeter. This was followed by a network that calculates a correction to the scattering angle due to a deflection of the track as it left the target's strong magnetic field. A third type of network, used primarily for tracking analysis, provided a correction to naive momentum vector at the face of the calorimeter, which again, was a result of a deflection in the target's field. The following sections provide the details of how each network was implemented and used.

C.3 Position Correction at BigCal

In order to better determine the particle's position, a neural network was developed to give a correction to the cluster position which is given by 5.1. The

position corrections provide the location where the track crossed the plane formed by the face of BigCal as shown in Figure C.1. The corrections are defined as

$$\delta_x = x_{BC} - x_{cluster} \quad (\text{C.1})$$

$$\delta_y = y_{BC} - y_{cluster} \quad (\text{C.2})$$

where x_{BC} and y_{BC} are the positions in the plane obtained from simulation.

The need for such a correction becomes clear, for example, when considering the difference between a shower produced at the top the calorimeter. The large angle of incidence and longitudinal size of the shower makes the vertical position larger than the actual location it entered the calorimeter.

Therefore, quantities characterizing the cluster, such as the standard deviation, skewness, and kurtosis were used as input neurons. See section 5.2.2 for their definitions. Alternatively, each block in the cluster could have been selected as an input neuron instead of these quantities. However, as we will see, understanding the resulting network's behavior becomes much easier when using quantities with well defined meanings.

C.3.1 Photon Position Correction

The position correction for a photon was calculated first because this correction was used with clusters when calibrating BigCal with photons from the $\pi^0 \rightarrow \gamma\gamma$ decay (see appendix D). For both target field configurations a sample of 1M simulated photon events, thrown uniformly in solid angle and energy, were used to train each neural net. As expected, the networks produced were very similar because the target field does not directly affect the photon's electromagnetic shower development. The results of one network training are shown in Figure C.2.

In order to understand the results small changes in the input variables are made for each test dataset and the magnitude of the difference this change has

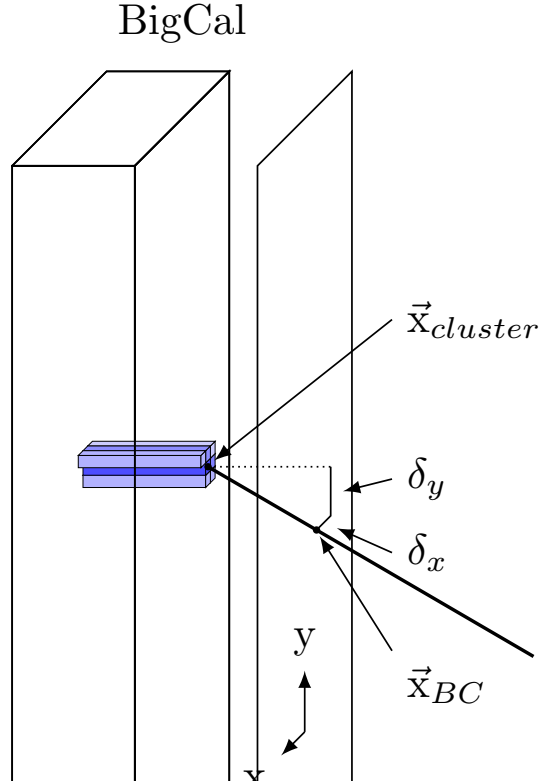


Figure C.1.: A blown up view of the BigCal plane where the cluster position is corrected. Note the BigCal plane is actually flush with the front face of the calorimeter.

is plotted for each input as shown in Figure C.3. This figure shows the input variable impact for the y correction, δ_y and can be easily understood as follows.

The vertical position (green) has the largest impact not only because it determines the block size, i.e., which section the cluster occurred in, but also the angle of incidence of the shower which is larger further from the center. Similarly, the next largest impact comes from the vertical skewness of the cluster (cyan) which is expected to get larger with angle of incidence. Next, the vertical kurtosis (violet) and vertical width (yellow) have a sizable impact because they are both indications of the vertical spread of the shower among the cluster blocks.

The x correction network can be similarly understood in terms of the horizontal input variables. The impact of small variations of the inputs is shown in

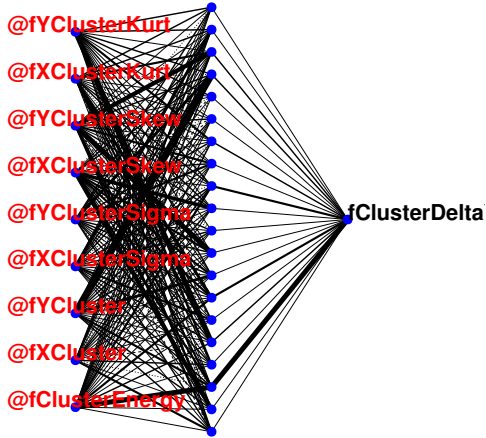


Figure C.2.: An example of the y position correction network for photons. The thickness of the line indicates the trained neuron's output weight for the neurons in the following layer.

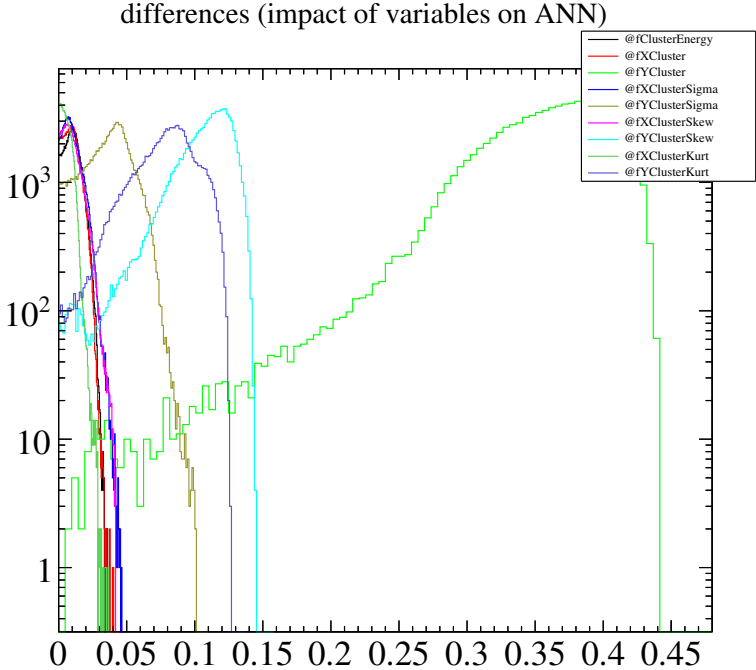


Figure C.3.: Histogram show the size of the impact on the y position correction caused by a small change in the input variables of the test dataset.

Figure C.4. Just like the y correction, the horizontal variables have the same ordering in their impact—position, skewness, kurtosis, and standard deviation — with one exception, the vertical position. Because the blocks change size going from top to bottom, the vertical position (green) has a large impact on the x-correction as it indicates the block size. This impact is narrowly peaked at some mean value due to the predictable nature of the block size given a vertical position.

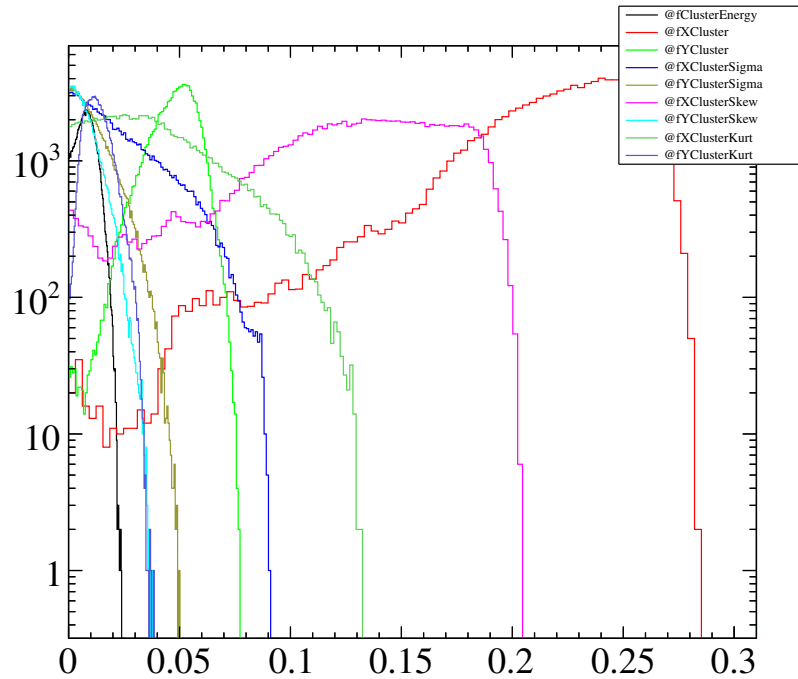


Figure C.4.: Same as Figure C.4 but for the x position correction.

C.3.2 Electron and Positron Corrections

Similar neural networks were constructed for electrons and positrons. Again, networks were constructed for each target configuration. The resulting networks were very similar because the electromagnetic showers did not vary much between electrons, positrons, and photons. However, the networks were kept separate in

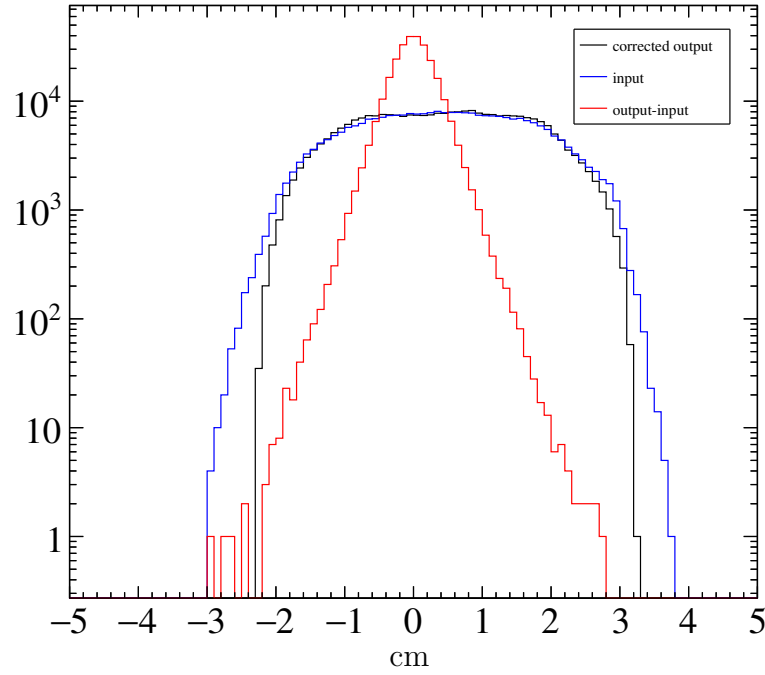


Figure C.5.: Results of training for the photon's correction δ_x . The red histogram shows the difference between the network output (black) and the training data set (blue).

order to isolate any subliminal patterns unique to the particle or target configuration.

C.4 Reconstructing Scattering Angles

After reconstructing the event to the BigCal plane, the next neural network calculated corrections to the scattering angles

$$\delta\theta = \theta_0 - \theta_{BC} \quad (\text{C.3})$$

$$\delta\phi = \phi_0 - \phi_{BC} \quad (\text{C.4})$$

where θ_0 and ϕ_0 are the angles from the simulation thrown at the target target position. The angles θ_{BC} and ϕ_{BC} are the naive track reconstructed as a straight

line from BigCal to the target. For this reason, photons do not require this correction and networks were only constructed only for electrons and positrons.

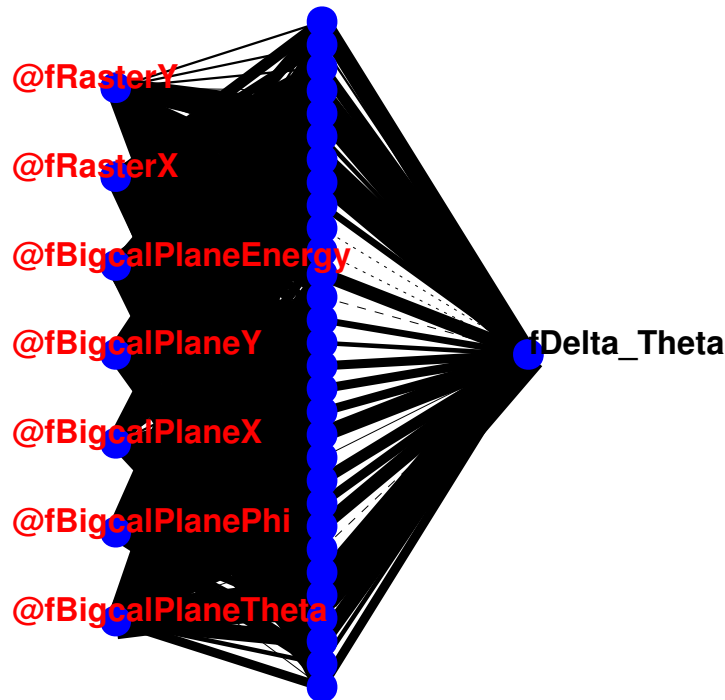


Figure C.6.: An Electron angle correction neural network.

The training dataset consisted of 1M detected events generated from events thrown uniformly in angle and energy. The vertex of the thrown events was uniformly sampled from a target volume defined by the target materials and a simulated slow rastered beam.

The input neurons for these networks, as shown in Figure C.6 were the beam x and y raster positions, particle energy, BigCal plane position (which is output from the previous network), and the naive angles calculated by a straight line from BigCal to the target. The raster position is included because an event on the far side of the target cell will travel through a larger volume of strong magnetic field than an event on the near side. This can be seen in input neuron impacts for $\delta\theta$ shown in Figure C.7. As expected, the x raster position has a

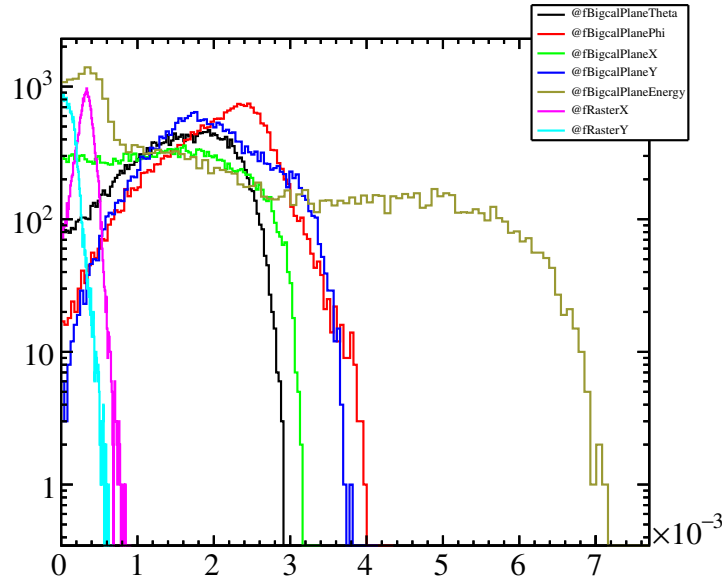


Figure C.7.: Histograms showing the impact of the inputs, shown in Figure C.6, on the angle correction, $\delta\theta$.

larger impact than the y-raster position. The impact of the inputs for $\delta\phi$ are shown in Figure C.8. It is clear here that the energy has the largest impact which is easily understood because low momentum particles are bent more in the magnetic field.

C.5 Momentum Direction at BigCal

In order to check the previous neural network's reconstruction, a track propagator was implemented to determine the correct scattering angles. This method was computationally more expensive so it could not be easily used for every event. The input to the backwards track propagator was only the momentum vector at BigCal. Instead of just using a simple momentum vector formed by a line between the target and cluster position, a neural network was built to provide a correction to these angles. This provided a more accurate starting point to provide a more accurate starting point for the track propagator.

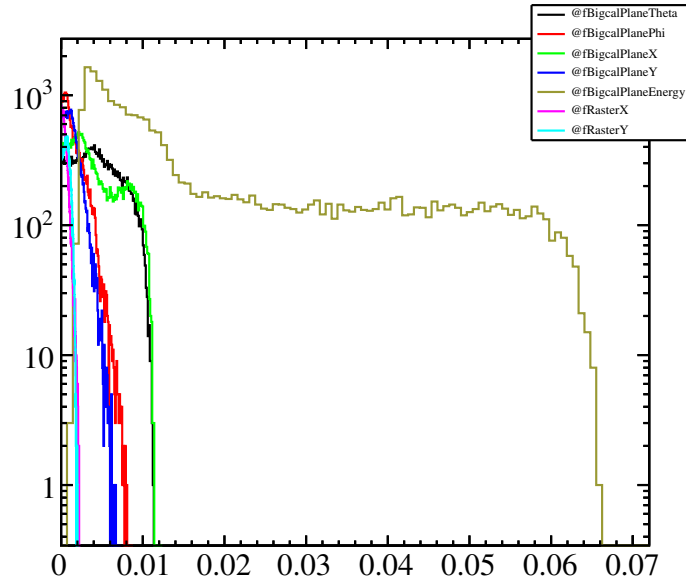


Figure C.8.: Same as Figure C.7 but for the angle correction $\delta\phi$.

Trained in a similar fashion to the angle corrections, the training dataset inputs were similar except the angles were the corrections to the momentum vector at the face of the calorimeter. This network was also useful for doing tracking studies and vertex reconstruction.

APPENDIX D

BIGCAL CALIBRATION

As mentioned in section 5.3.1 the BigCal electromagnetic calorimeter was calibrated with photons from π^0 decays. The correct invariant mass obtained by adjusting the calibration coefficients for each calorimeter block.

The SANE experiment used a large acceptance detector package, the Big Electron Telescope Array (BETA), to detect inclusive electron scattering events. Of the many backgrounds are the decay products of the π^0 meson. Because the decay channel is through the strong force ($\tau \sim 10^{-27}$), the π^0 decays almost instantly. Therefore, we can assume the vertex for such a decay is located at the target. Furthermore, the most probable decay channel is two photons with a branching ratio, $\Gamma_{\gamma\gamma}/\Gamma_{total}$, just below 0.99. The next highest decay channel is $\pi^0 \rightarrow e^+e^-\gamma$ with a branching ratio just above one percent.

D.1 Event Selection

The events were selected by the π^0 trigger which requires at least two quadrants of BigCal to have a hit. Electrons and positrons were removed by an anti-Čerenkov cut placed on both clusters. The pion mass is reconstructed as

$$m_{\pi^0}^2 = 2\nu_1\nu_2(1 - \cos(\theta_{\gamma\gamma})) \quad (\text{D.1})$$

where $\nu_{1,2}$ are the photon energies and $\theta_{\gamma\gamma}$ is the angle between them. The mass reconstruction is not only sensitive to the energy reconstruction of the photons, but also the position reconstruction. Therefore the cluster positions are corrected using the neural networks position corrections described in section C.3.

D.1.1 Kinematics and Geometry

The trigger layout of BigCal is shown in Figure 4.10. The thick red and black boxes highlight the trigger quadrants of the PI0 trigger. Because the threshold for each quadrant was roughly 500 MeV the reach of the calibration into the corners was limited. That is, the corners of the calorimeter had a much more restricted phase space of events that were able to fire the trigger.

Furthermore, since the few events in the corner come from triggers that are very near threshold, the signal to noise ratio is much higher. This not only affects the corners blocks but the entire detector because the background events can poison a calibration in that region. This region is then used for events spanning a larger part of the detector. Therefore it spreads to the whole detector. This was the case with the original calibration which was off as much as 20%.

To avoid this problem, a procedure was developed which systematically calibrates regions of the detector. The procedure exploits the trigger geometry to ensure complete coverage of good π^0 events.

D.2 Calibration Method

Following the iterative method in [105], each block's calibration coefficient is calculated by inverting an $N_b \times N_b$ matrix. The goal is to find the minimum of

$$F = \sum_{i=1}^N (m_i^2 - m_0^2)^2 + 2\lambda \sum_i (m_i^2 - m_0^2) \quad (\text{D.2})$$

where N is the number of events, m_i is the reconstructed mass for the i th event, m_0 is the known mass, and λ is a Lagrange multiplier. The invariant mass of the two photon system is given by

$$m_i^2 = 2\nu_1\nu_2(1 - \cos\theta_i) \quad (\text{D.3})$$

where ν_1 and ν_2 are the photon energies, and θ_i is the angle between the two momentum vectors.

When reconstructing the angle between the two momentum vectors, each cluster's position is corrected to the BigCal plane with an artificial neural network. This takes care of correcting for angular effects in the shower's shape. The energy of each shower, with index $j = 1, 2$, is calculated simply as the sum over the blocks, with index k , that contribute to the cluster. It is given by

$$\begin{aligned}\nu_j^{(i)} &= \sum_{k \in j} C_k A_k \\ &= \sum_{k \in j} E_k\end{aligned}\tag{D.4}$$

where C_k is the block calibration coefficient, A_k is the ADC signal, and E_k is the energy deposited in the block.

In order to proceed with minimization, the following substitution is made

$$E_k \rightarrow E'_k = (1 + \epsilon_k)E_k\tag{D.5}$$

where ϵ_k is a small correction to the block's energy. The goal is to calculate these corrections by minimizing equation D.2. The solution is simplified by the following approximate derivatives

$$\frac{\partial \nu'_j}{\partial \epsilon_k} \simeq E_k\tag{D.6}$$

$$\frac{\partial m_i'^2}{\partial \epsilon_k} \simeq m_i^2 \frac{E_k}{\nu_j}\tag{D.7}$$

With these approximations the solution to D.2 is written in matrix form

$$\epsilon_k = [C^{-1}]_{kk'} (D - \lambda L)_{k'}\tag{D.8}$$

where

$$C_{kk'} = \sum_i = 1^N \left(\frac{\partial m_i'^2}{\partial \epsilon_k} \frac{\partial m_i'^2}{\partial \epsilon_{k'}} \right), \quad (\text{D.9})$$

$$D_k = - \sum_i = 1^N \left((m_i^2 - m_0^2) \frac{\partial m_i'^2}{\partial \epsilon_k} \right), \quad (\text{D.10})$$

$$L_k = \sum_i = 1^N \frac{\partial m_i'^2}{\partial \epsilon_k}, \quad (\text{D.11})$$

$$\lambda = \frac{B + L^T C^{-1} D}{L^T C^{-1} L}, \quad (\text{D.12})$$

$$B = \sum_i = 1^N (m_i^2 - m_0^2), \quad (\text{D.13})$$

and C is an $N_b \times N_b$ matrix. After a few iterations the energy corrections should converge towards zero.

The numerical difficulty arises from calculating the inverse of the C matrix, which might not exist if there are not enough events covering all the blocks. Furthermore, with 1724 blocks to calibrate, this inversion is computationally expensive. Instead an eigenvalue decomposition leads to the solution for the inverse as

$$[C^{-1}]_{kk'} = \sum_{\alpha} \frac{1}{c(\alpha)} e_k(\alpha) e_{k'}(\alpha) \quad (\text{D.14})$$

where the sum is over the eigenvalues, $c(\alpha)$, and eigenvectors $e(\alpha)$. Small eigenvalues consistent with zero and their corresponding eigenvectors are removed from the sum. This avoids the singularities that otherwise plague such a large calorimeter.

Another problem arises when at each iteration the full value of ϵ_k is applied. This causes an over correction and iteration oscillate about the correct value of ϵ_k . This is not surprising because the approximations of the derivatives in the solution above were assuming ϵ was small. To mitigate this problem, only a small fraction of the correction is applied. While this increases the number of iterations needed, it guarantees a smooth convergence.

D.3 Calibration Procedure

Software was developed following the general method outlined above allowing for arbitrary and disjoint sections of the calorimeter to be calibrated simultaneously. Some blocks can be activated to participate in the reconstruction but their calibration constants are held fixed and are thus not part of the matrix inversion.

Furthermore, at each iteration the mass cut around the π^0 mass peak was made tighter. This allowed for an inclusive start but then limits the background events seen at each iteration which can spoil the calibration. Similarly, a fixed number of the roughly 8M $\text{PI}0$ events were used for each iteration. This guaranteed that each iteration sees a completely different set of events which avoids the problem of a few background events causing a few coefficients to slowly diverge due the method trying to accommodate the same background event.

Finally, as mentioned above, a procedure was developed to incrementally calibrate the whole detector. This avoids trying to include areas of the detector that have very little probability of good events. Groups of calorimeter blocks were organized into “sectors” as shown in Figures D.1 (a-f), which make up the basic sequence of calibration. The distribution of energy is consistent with the $\text{PI}0$ trigger quadrants used for each sector.

The first sector (a) used only the lower quadrants, while (b) used only the upper quadrants. Sectors (c) and (d) used only the left and right, respectively. Sector (e) used all four quadrants, and as expected, the central blocks of this sector are the most populated as they have the highest probability to participate in the $\text{PI}0$ trigger.

The sectors (a-e) covered all the blocks in BigCal except for the corners which make up sector (f). When calibrating this sector, all calorimeter blocks were made active, that is, they participated in the reconstruction but did not get calibrated themselves. This made use of the previously calibrated sectors and the distribution of clusters is shown in Figure D.1(g). This allowed the corners

to be calibrated while preventing these few events from contaminating the rest of the calorimeter.

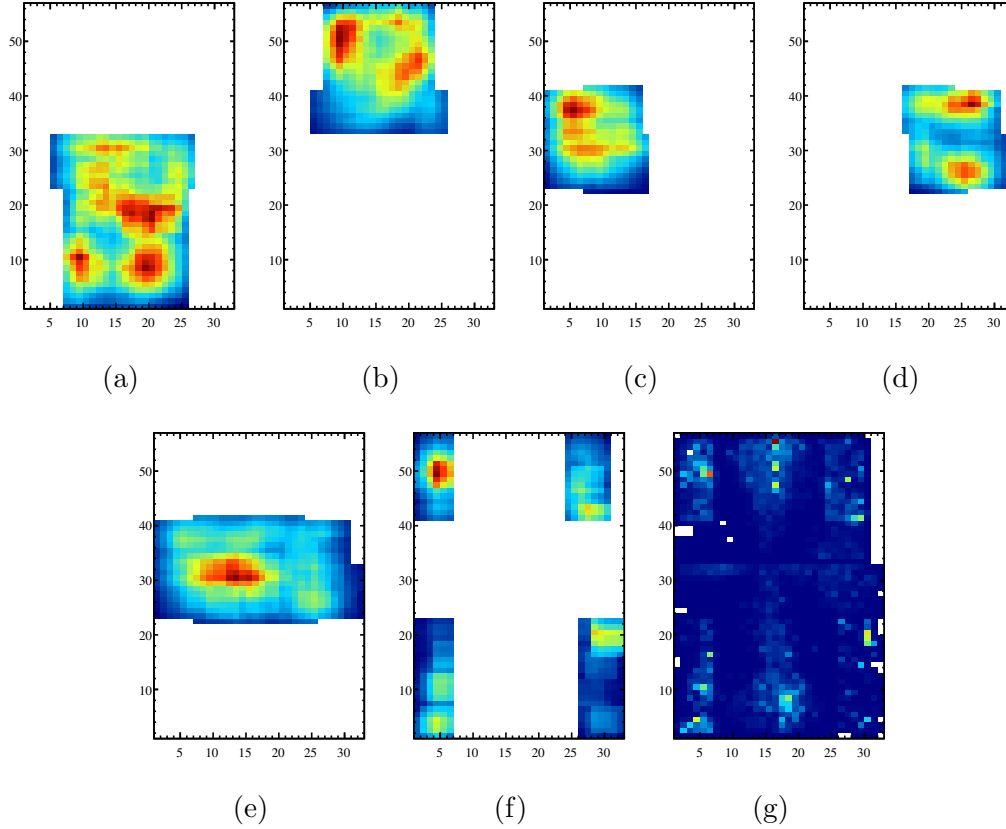


Figure D.1.: The BigCal calibration sectors are shown in Figures (a-f). All active blocks participating in calibrating sector (f) are shown in (g).

D.3.1 Previous method

Initially, the calibration was done with an energy correction from the simulation already applied. That is, the simulation determined how much energy was missed by the calorimeter. This led to large differences between the Protvino and RCS calorimeter sections. The reconstructed energy for electrons and photons was

$$E_{e,\gamma} = E_{cluster}^{data} + \delta E \quad (\text{D.15})$$

where $E_{cluster}$ is the calibrated cluster energy and δE is a correction that comes from simulation. This correction calculated as

$$\delta E_{e,\gamma} = E_{thrown} - E_{cluster}^{sim} \quad (D.16)$$

This method relies on an accurate simulation of $E_{cluster}^{sim}$ that matches exactly $E_{cluster}^{data}$. However, this is rather difficult for two reasons. The simulation is an over idealized scenario where the energy deposited in the cluster is turned into an ADC value by using some set of calibration coefficients (determined from π^0 calibrations). Secondly, both the photon and electron reconstruction follows the same way.

D.3.2 New Method

Instead of letting the simulation dictate the size of the energy correction to the photons which is subsequently used in optimizing the calibration coefficients, we let the calibration coefficients absorb the energy correction, as is the purpose of the calibration. This has the advantage that we are now not directly using the simulation's treatment of the energy deposited.

$$\delta E_{e,\gamma} = a E_{cluster}^{sim} \quad (D.17)$$

where $a = E_{thrown}/E_{cluster}^{sim}$.

D.4 Independent Checks

The calorimeter energy reconstruction was crucial to the success of the experiment due to the lack of a redundant momentum measurement. Therefore, an independent check was performed using elastic events that were recorded in coincidence with the HMS. Due to the kinematics the rates for these events were

very low, so they were summed over the whole experiment. The HMS detected a proton and reconstructed the electron energy, E_{el} , from the overdetermined kinematics. The difference between this energy and the energy reconstructed by BETA should be center at around zero. However, the analysis was plagued nearly the entire time by a large difference (of about ~ 400 MeV) that could not be explained. Additionally confusing was the need for different sets of calibration coefficients for the two target configurations.

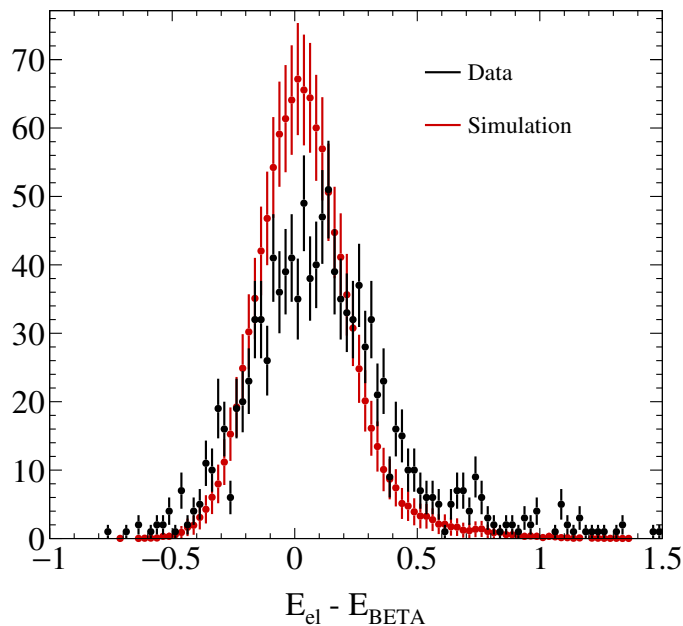


Figure D.2.: The elastic events energy difference checking the energy reconstruction of BigCal [106].

The big improvement came when the calibration coefficients were reset to their roughly gain matched values and recalibrated from scratch following the procedure above. The resulting energy difference with this calibration is shown in Figure D.2. Clearly there was dramatic improvement! It appears that the old calibration [107] had been worked into a local minimum, likely caused by

background events. By careful event selection and incrementally calibrating areas in a systematic and thoughtful way, the local minima is avoided.

APPENDIX E

RADIATIVE CORRECTIONS

Radiative effects are fundamental to quantum field theories like QED and QCD. As discussed in Section 3.2.2, QCD radiative effects play a central role in understanding the partonic structure of the nucleon. Radiative corrections have a long history of providing calculations for precision tests of QED. However, the radiative corrections discussed here are of a more utilitarian nature as they merely a consequence of the realization of the experiment. Although they are not directly related to the motivating physics of this work, radiative corrections are interesting and important for all electron scattering experiments. The formalism of Mo and Tsai [69, 108, 109] is mainly used throughout this section. Additionally, a polarization dependent treatment [70] is studied.

There are two classes of radiative corrections: internal and external. The internal radiative corrections are theoretical in origin and take into account higher order QED effects such as vacuum polarization, vertex corrections, self energies, and bremsstrahlung. External radiative corrections have their origins in the experimental apparatus. They are a result of the finite material thicknesses that the incident and scattered electron must cross, causing radiative energy losses.

Each type of scattering has a certain kinematic behaviour which necessitates separate treatments. For example, the inclusive elastic scattering cross section in the presence of radiative effects, internal and external, develops a tail that falls off as the kinematics move away from the elastic peak. However, very far away from the peak the tail begins to grow dramatically.

An unfolding procedure is required for experiments measuring crossing absolute cross sections that want to determine the Born level cross section in a

model independent way. Also, as emphasized in [69], for a fixed scattering angle the cross section needs to be measured over nearly the full range in scattered *and* incident beam energies. Since we did not measure cross sections, our concern is primarily with the radiative effects on the asymmetries. In lieu of an unfolding procedure, the radiated cross section is calculated using empirical fits to data [85, 86, 110] and models where necessary.

E.1 The Elastic Radiative Tail

The radiative corrections to the elastic scattering cross section produce a tail that spans the whole spectrum of energies. Conceptually the process can be simplified by only considering two cases: energy loss before and energy loss after the elastic scattering.

First, when near the elastic peak and the incident beam loses energy before scattering, the cross section is enhanced because the elastic cross section is larger for lower incident beam energies. This can be seen by comparing the solid curve to the dashed curve in Figure E.1. In the case where the scattered electron loses a energy after scattering, the cross section does not have this enhancement. However, energy losses after scattering smear the elastic peak, an effect that also increases at lower energies.

Further from the elastic peak the tail begins to increase because the incoming beam radiates a significant amount energy, thus effectively becoming a beam of lower energy electrons. The elastic scattering cross section is much larger for lower incident energies, therefore, the tail begins to increase. An example of the elastic tail is shown as the black curve in Figure E.1. The decreasing probability of the incident beam losing a large fraction of its energy is apparently compensated by the increasing elastic cross section.

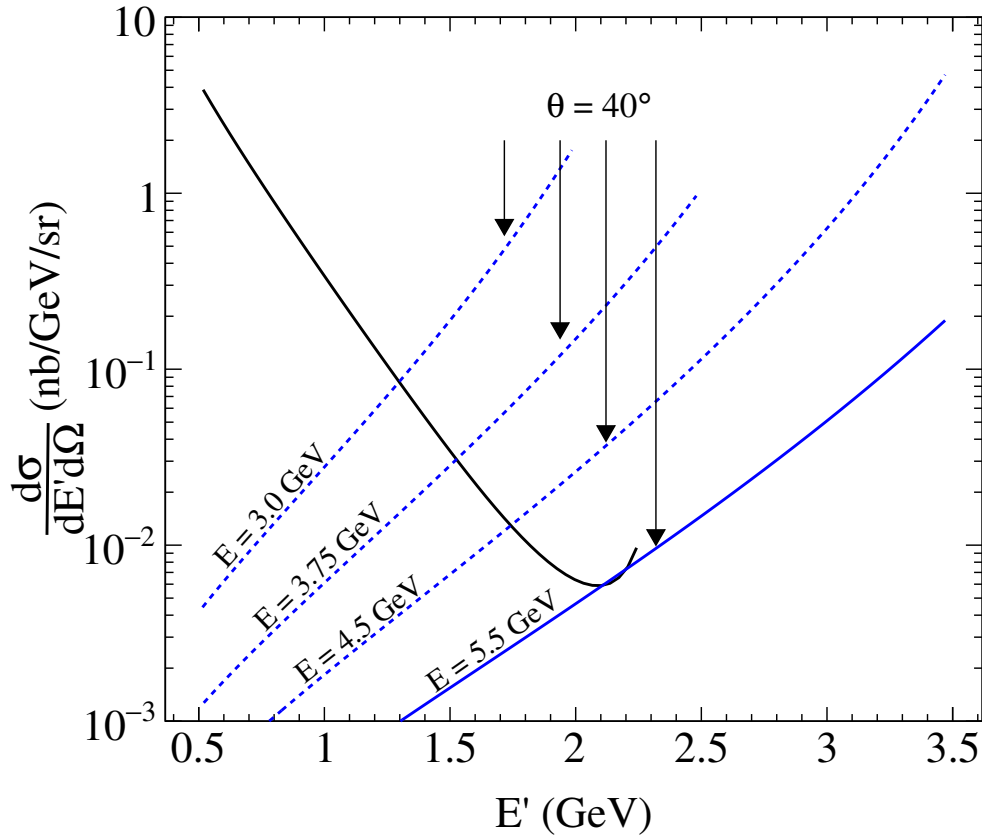


Figure E.1.: Elastic radiative tail (black) for 5.5 GeV incident electrons scattered at 40° . The elastic cross section is shown in blue (solid) for the incident beam energy. It is also shown for lower incident energies (dashed). The arrows point to the location of the elastic peak for scattering at 40° .

For elastic scattering the internal and external contributions can be separated and written as

$$\frac{d\sigma^{ERT}}{dE_p d\Omega}(E_s, E_p, T) = \frac{d\sigma^{ERT}}{dE_p d\Omega_t}(E_s, E_p, T) + \frac{d\sigma^{ERT}}{dE_p d\Omega_r}(E_s, E_p). \quad (\text{E.1})$$

where the E_s is the incident beam energy, E_p is the scattered electron energy, T is the target thickness in radiation lengths, ' t ' indicates the cross section corrected

for (external) target effects, and ‘ r ’ indicates the (internal) radiative corrected cross section.

E.1.1 Corrections to the Elastic Peak

Before calculating elastic radiative tail, the elastic peak was corrected for contributions like those shown in Figure E.2. The Born level cross section (a) was corrected yielding the internally radiated cross section

$$\left(\frac{d\sigma}{d\Omega}\right)_r = (1 + \delta) \left(\frac{d\sigma}{d\Omega}\right)_{Born} \quad (\text{E.2})$$

where δ is the sum of all contributions (b-i) shown in Figure E.2. Specifically, the contributions are the vertex correction (b), the vacuum polarization (c), the self energy (d-e), bremsstrahlung (f-g), and two photon exchange (h-g). Not shown are the similar hadronic corrections. In total, these are the internal radiative corrections to the elastic peak.

The cross section E.2 is experimentally inaccessible because it will always receive external radiative corrections, but it does provide a point of reference when considering the specific treatment of the internal radiative corrections. An additional correction, δ_t , for external effects due to ionization and bremsstrahlung in the target material can be calculated following [108].

E.1.2 Internal Elastic Radiative Tail Corrections

With the corrected elastic cross section the internal radiative corrections can be calculated. Two separate treatments were investigated. The first was the standard Mo and Tsai treatment. In this treatment the elastic radiative tail can be calculated exactly following equation B.5 of [69] or use an equivalent radiator approximation. The latter method simply adds two radiator thickness, one before and one after scattering, which are equivalent to the internal radiative

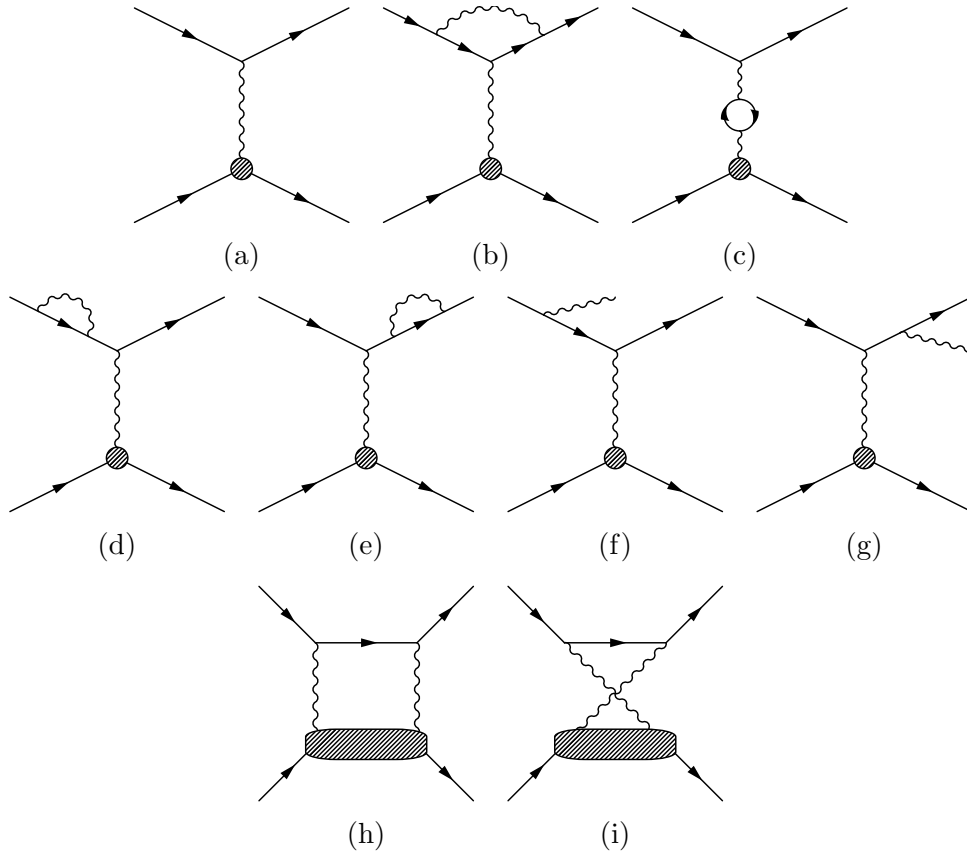


Figure E.2.: Feynman diagrams for calculating radiative corrections.

effects. This is used with the energy peaking approximation method described below.

The second treatment [70,111,112] includes polarization effects but only considers the internal radiative corrections. The polarized elastic radiative tail, σ_r^{ERT} was calculated using the existing POLRAD code [113]. Additionally, new code was also developed [65] following this treatment as well and produced identical results for the elastic radiative tail.

Figure E.3 shows the difference between these two treatments of the elastic radiative tail. Using the same model inputs, the asymmetries were calculated and their difference was found to be less than 0.5%. This indicates that any polarization effects neglected in the Mo and Tsai treatment are negligible.

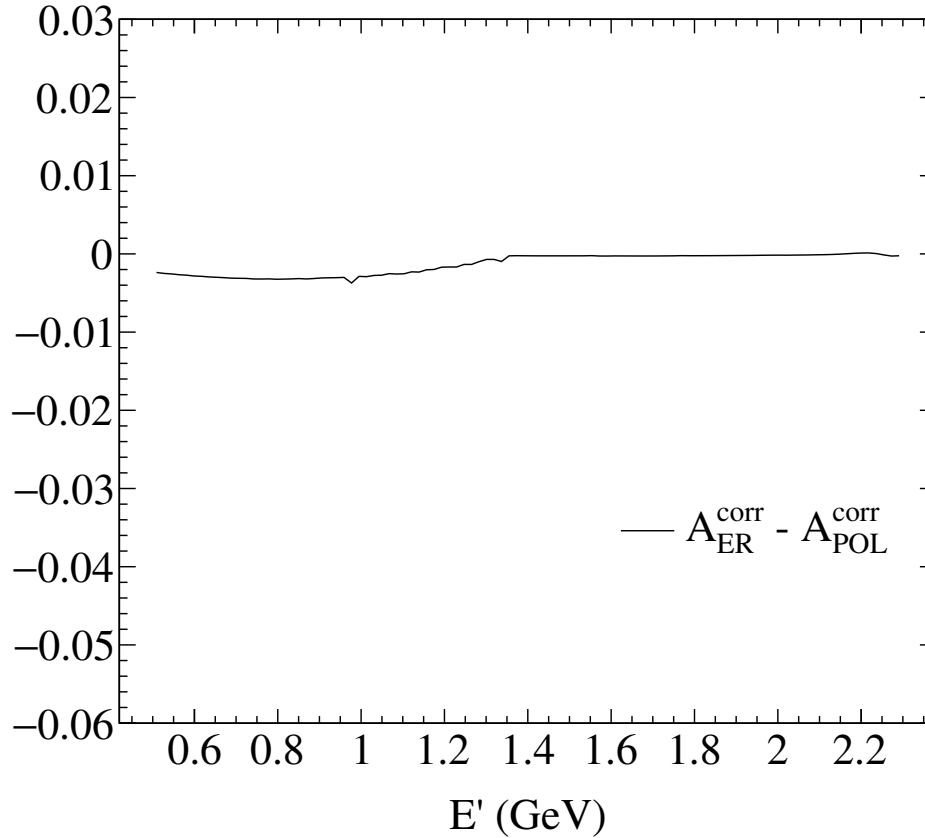


Figure E.3.: The difference between asymmetries of the elastic radiative tail calculated from the same input model using the two methods described in the text.

E.1.3 External Corrections

After calculating the radiative tail due to the elastic peak, the external radiative effects were calculated following the exact and approximate methods of [69]. There was little difference between the exact and approximate in this case. The approximate method that was used is discussed further in Section E.2.2.

E.2 The Inelastic Radiative Tail

E.2.1 Internal Corrections

It was found that there are not any noticeable differences between the standard treatment [69] and the polarized treatment [111]. Furthermore, the *equivalent radiator* method, which approximates the internal radiative effects by adding some radiators (see equation 2.7 of [108]) to the target radiation length, works quite well as shown by Figure E.4.

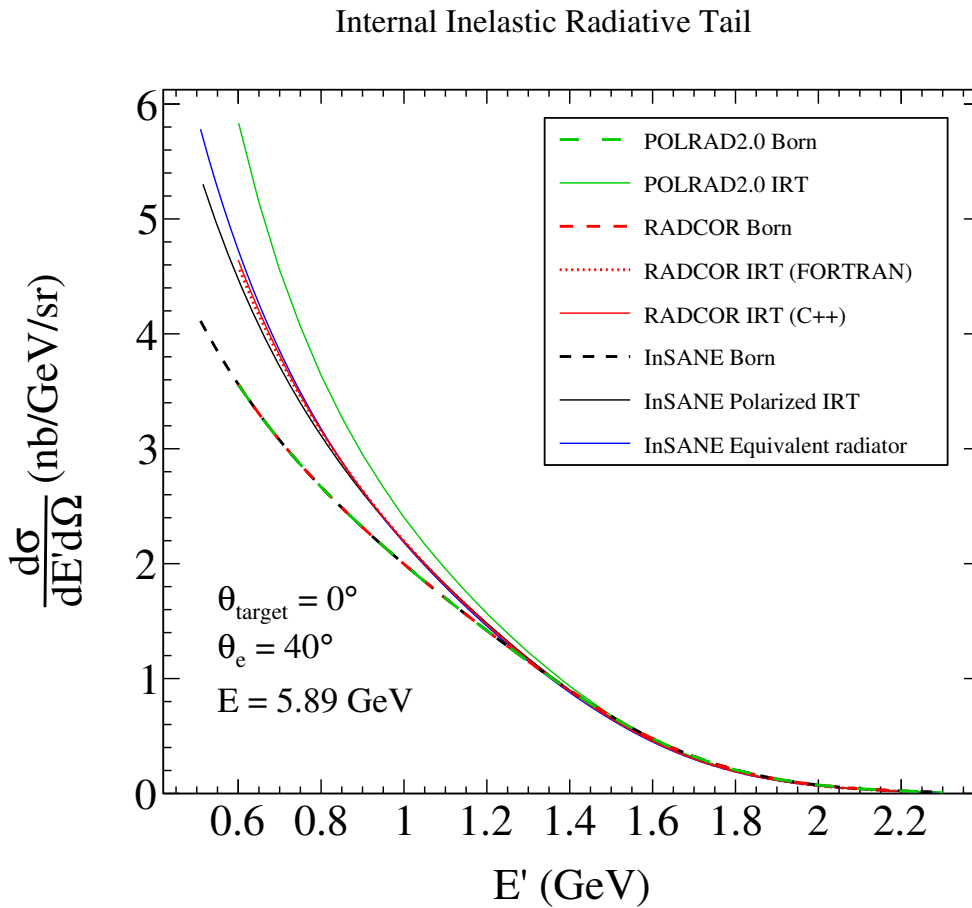


Figure E.4.: Comparisons between different codes and methods for calculating the internal contribution to the inelastic radiative tail

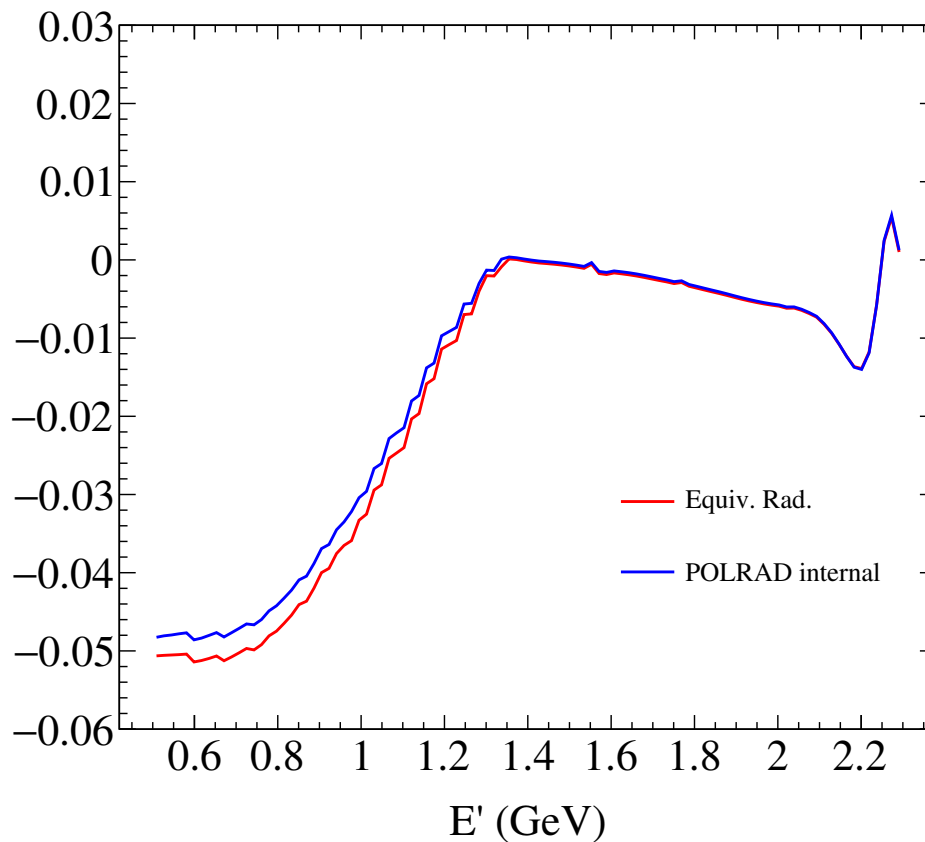


Figure E.5.: The inelastic asymmetry correction (equation 5.18) calculated from the same input model using two different internal radiative correction methods: the equivalent radiator (red) and the polarized treatment (blue).

E.2.2 Energy Peaking Approximation

Following equation A.22 of Mo and Tsai [69, 108], the inelastic external radiative corrections to the internally radiated cross section can be written using

the energy peaking approximation. The energy peaking approximation for the inelastic radiative can be modified to include beam depolarization effects

$$\begin{aligned}
 \sigma_{t+r}(E_s, E_p, T) &= e^{\delta_s + \delta_p} \sigma_r(E_s, E_p, T) \\
 &+ e^{\delta_s/2} \int_{E_{s\min}(E_p)}^{E_s - \Delta} [1 - D(E_s, E'_s, Z)] I_e(E_s, E'_s, T) \sigma_r(E'_s, E_p, T) dE'_s \\
 &+ e^{\delta_p/2} \int_{E_p + \Delta}^{E_{p\max}(E_s)} I_e(E'_p, E_p, T) \sigma_r(E_s, E'_p, T) dE'_p .
 \end{aligned}
 \tag{E.3}$$

where D is the beam depolarization factor calculated following [114]. In general the size of the depolarization is very small.

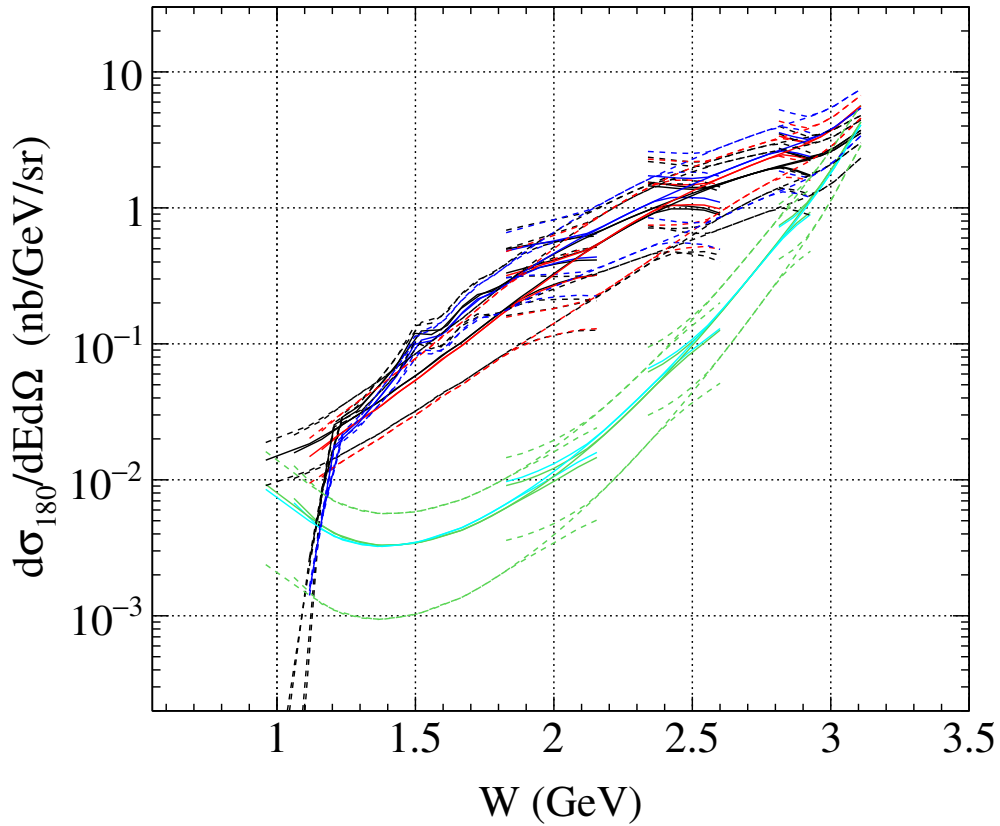


Figure E.6.: A comparison of the inelastic radiative tail for different cross models.

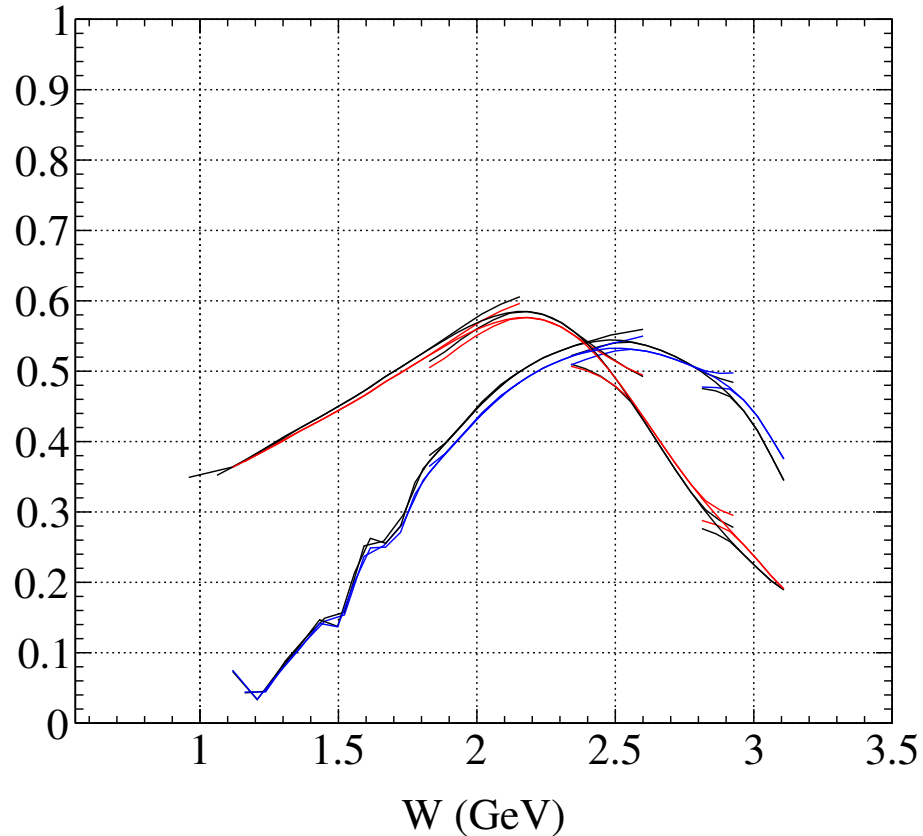


Figure E.7.: The asymmetries of the inelastic cross sections shown in Figure E.6.

E.3 Comparing Codes

A comparison between the various codes and approximations are shown in Figure E.4 where the input Born cross sections (dashed) are identical and used to calculate the internal inelastic radiative tail. The existing Fortran codes `RADCOR` [115–117] and `POLRAD` [113] are shown in addition to a C++ implementation of `RADCOR` [117] and the newly developed radiative corrections code which is part of the `InSANE` [65] C++ libraries. All the codes are in agreement except the `POLRAD`.

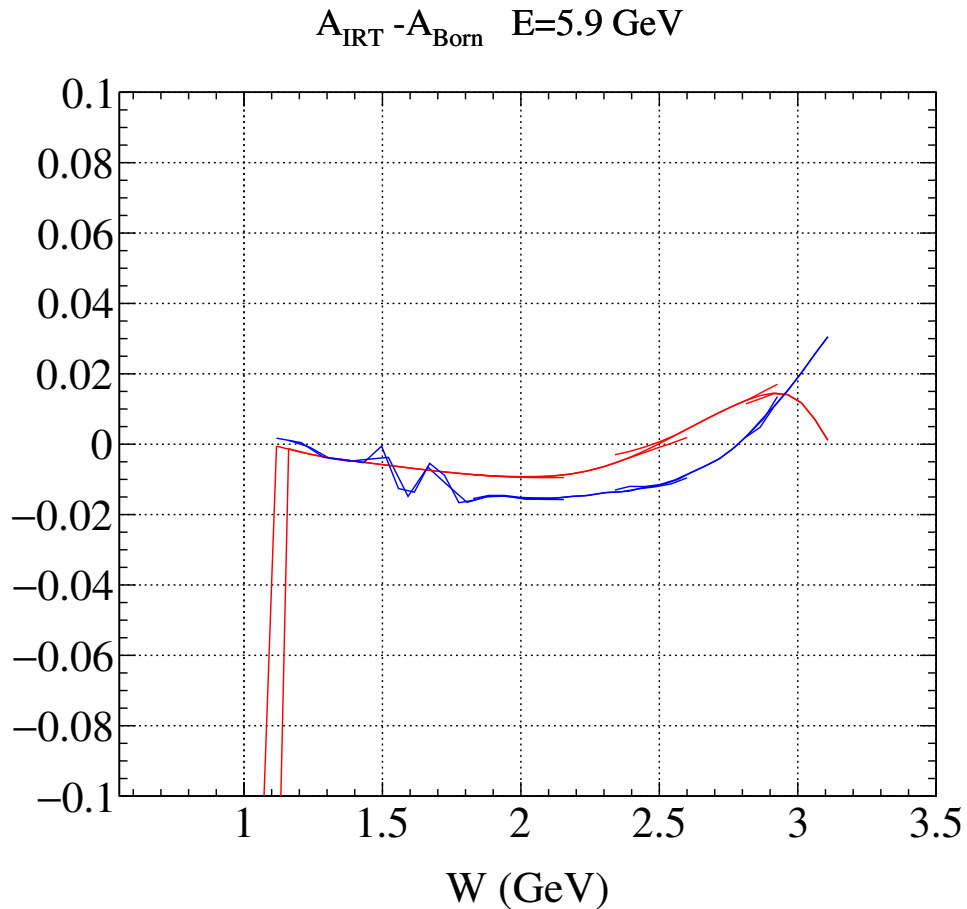


Figure E.8.: The inelastic asymmetry correction calculated using two very different cross section models.

E.3.1 POLRAD

The InSANE inelastic tail shown was calculated following the same method as POLRAD. After a lot of investigation, it was concluded that the discrepancy shown in Figure E.4 is due to the integration subroutine used in POLRAD.

Upon close inspection it was found that there are a number of discrepancies between what is written in the Fortran code and the POLRAD manual [113]. They are reported here for future reference and documentation purposes.

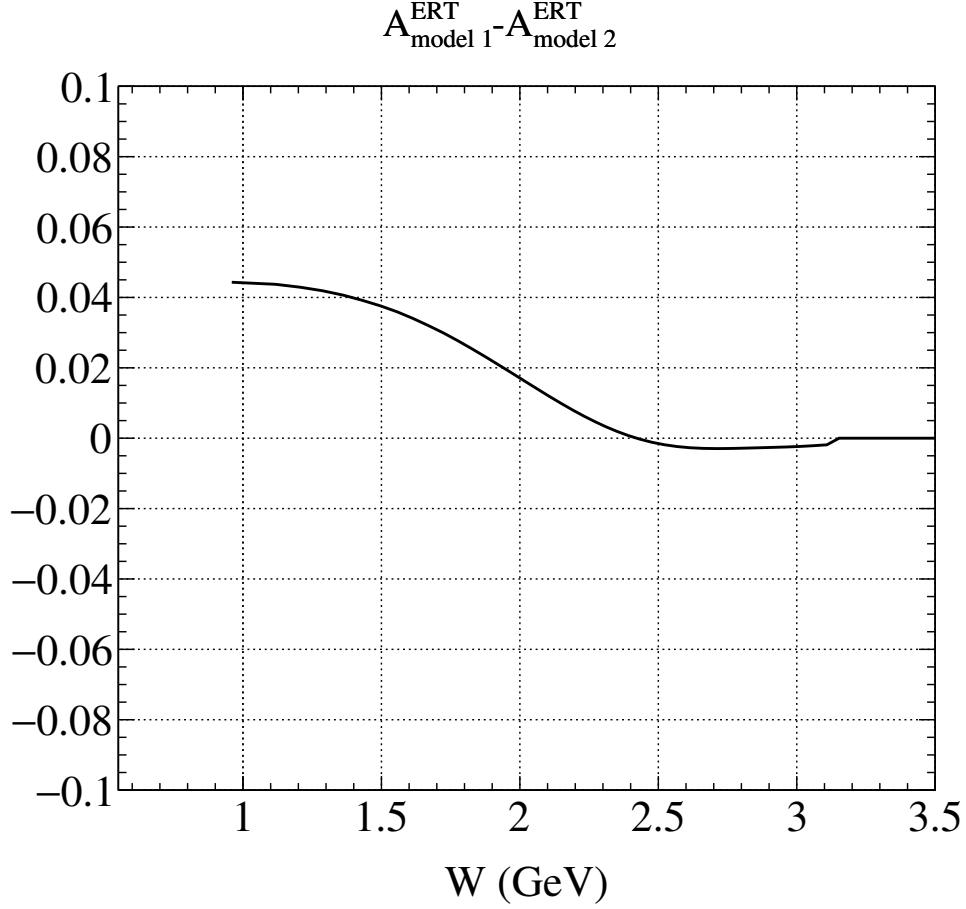


Figure E.9.: The extreme case of any model dependence on the elastic radiative tail. The dipole form factors were used as a baseline comparison.

Equation B.8 of [113] is missing a τ in the first term and should read

$$4F_{2-}^{\{\xi,\eta\}\eta} = (2F_d + F_{2+})(r_\eta s_{\{\xi,\eta\}} + s_\eta r_{\{\xi,\eta\}})\tau + F_{2-}(r_\eta r_{\{\xi,\eta\}} + \tau^2 s_\eta s_{\{\xi,\eta\}}) + 4\tau F_{1+} s_\eta s_{\{\xi,\eta\}} \quad (\text{E.4})$$

Equation defining a_{ik} of B.3 are missing several factors of M in denominator. For $k = 1, 2$ and $i = 4, 8$ there is a missing factor of $1/M$, and for $k = 1, 2, 3$ and $k = 5, 6$ there is a missing factor of $1/M^2$.

The substitution in Equation B.6 for calculating θ_{ij} is not clear. They mean to say that for each successive value of k one η is appended to the upper index.

For the θ_{ij} terms corresponding to *elastic* scattering, the substitution should be

$$\theta_{ij}(\tau) \rightarrow \theta_{ij}^A(\tau_A) \quad (\text{E.5})$$

where the index A is also applied to θ_{ij} , not just τ . In the POLRAD manual, the suggestion is to use τ_A , but with θ_{ij} unchanged. It is clear in their corresponding code that this is not the case and θ_{ij} should be used.

APPENDIX F

PAIR SYMMETRIC BACKGROUND CORRECTIONS

The primary source of background comes from photons that convert into electron/positron pairs in extra material at the target or detector material. A simulation was developed in order to understand this background. The following sections provide the details for calculating the background contaminations and dilutions used in the asymmetry analysis.

F.1 BETA Background subtraction

The correction for an experiment using a large magnetic spectrometer is

$$C_{bg} = \frac{1 - RA_{pair}/A_{raw}}{1 - R}, \quad (\text{F.1})$$

where $R = n_{pair,e+}/n_{dis,e-}$ and A_{pair} is the positron asymmetry. Note that there is also the measured ratio, $r = n_{pair,e+}/n_{total,e-} = R/(1 + R)$ which is often (incorrectly) interchanged with R .

The equations above are correct for an experiment which only detects electrons or high has a high positron rejection efficiency. However, for the case at hand, BETA was in an open configuration and detected both charges. Therefore, for each positron detected there is a corresponding electron, so a factor of two must be added to each R in the equation above. Thus the total rate would be

$$\begin{aligned} n_{total} &= n_{dis} + 2n_{pair} \\ &= n_{dis}(1 + 2R) \end{aligned}$$

or

$$\begin{aligned} n_{dis} &= n_{total} \frac{1}{1 + 2R} \\ n_{pair} &= n_{total} \frac{2R}{1 + 2R} \end{aligned}$$

It should be noted that due to the up-down symmetry of the target magnet, positron tracks are reconstructed the same as a positron track.

Using these definitions the correction can be split into a dilution correction and a contamination correction due to A_{pair} .

$$\begin{aligned} A_{corr} &= \left(\frac{1}{1 - 2R} \right) A_{raw} - \left(\frac{2RA_{pair}}{1 - 2R} \right) \\ &= \left(\frac{n_{dis}}{n_{dis} - 2n_{pair}} \right) A_{raw} - \left(\frac{2n_{pair}A_{pair}}{n_{dis} - 2n_{pair}} \right) \\ &= \left(\frac{1}{f_{bg}} \right) A_{raw} - (C_{A_{bg}}) \end{aligned}$$

F.2 Background Simulation

A simulation was developed to include all the target materials. The event generator sampled the inclusive electron cross section, inclusive photo- and electro-production cross sections for neutral pions. The pion cross sections used were obtained from Oscar Rondon's fit [68] to the world data for kinematics relevant to this experiment.

Results from the simulation are shown in Figure F.1. The impact of the Čerenkov ADC window cut (discussed in section 5.4) can be seen in Figure F.2 which shows the electron positron ratio. This cut is especially important at high energies where the relative size of the background is reduced by nearly a factor of two.

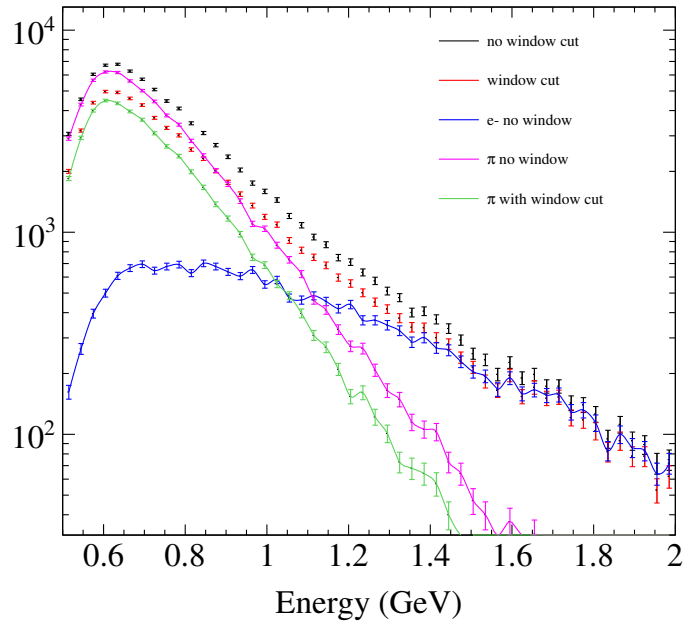


Figure F.1.: The energy distribution of the reconstruction of simulated events. The blue curve shows the relative yield for events that originate with a scattered electron. The green and pink curves show the diluting background events with and without a Čerenkov ADC window cut. Similarly, the red and black show the sum of all events with and with the window cut.

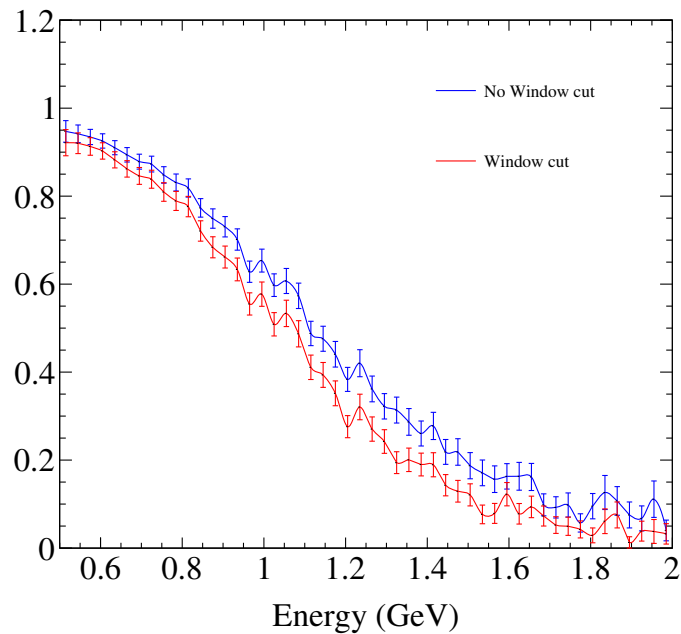


Figure F.2.: The ratio of positrons to electrons from simulation with and without a Čerenkov ADC window cut applied.

APPENDIX G

ERROR ANALYSIS

G.1 Statistical Uncertainty

The statistical uncertainty on the raw asymmetry is

$$(\sigma_{A_{\text{raw}}}^{\text{stat}})^2 = \frac{4n_1n_2}{(n_1 + n_2)^3} \quad (\text{G.1})$$

where n_1 and n_2 are the raw counting rates for the two electron helicities. When these are corrected for charge and live time (see equation 5.9) the statistical uncertainty becomes

$$(\sigma_{A_{\text{exp}}}^{\text{stat}})^2 = \frac{(A_{LT}^2 - 1)^2 (A_Q^2 - 1)^2 (\sigma_{A_{\text{raw}}}^{\text{stat}})^2}{(A_Q A_{\text{raw}} + A_{LT} (A_{\text{raw}} - A_Q) - 1)^4} \quad (\text{G.2})$$

where the live-time asymmetry is

$$A_{LT} = \frac{L_1 - L_2}{L_1 + L_2}, \quad (\text{G.3})$$

the charge asymmetry is

$$A_Q = \frac{Q_1 - Q_2}{Q_1 + Q_2}, \quad (\text{G.4})$$

and where $L_{1,2}$ and $Q_{1,2}$ are the live-times and accumulated charge for each helicity.

From equation 5.10 it follows that the statistical uncertainty after target dilution, target polarization and beam polarization corrections becomes

$$(\sigma_{A_{\text{meas}}}^{\text{stat}})^2 = \left(\frac{\sigma_{A_{\text{exp}}}^{\text{stat}}}{f P_B P_T} \right)^2 \quad (\text{G.5})$$

Similarly, from equation 5.12 the statistical uncertainty after background corrections is

$$(\sigma_{A_{\text{corr}}^{\text{stat}}}^{\text{stat}})^2 = \left(\frac{\sigma_{A_{\text{meas}}}^{\text{stat}}}{(1 - 2R)} \right)^2. \quad (\text{G.6})$$

Finally, the statical uncertainty after subtracting the elastic radiative tail is

$$(\sigma_{A_{\text{corr}}^{\text{el}}}^{\text{stat}})^2 = \left(\frac{\sigma_{A_{\text{corr}}^{\text{stat}}}^{\text{stat}} (\Sigma_{\text{el}} + \Sigma_{\text{in}})}{\Sigma_{\text{in}}} \right)^2. \quad (\text{G.7})$$

It is worth noting that the inelastic correction is purely a systematic uncertainty and does not affect the size of the statistical error bars.

G.2 Systematic Uncertainties

A summary of the estimated systematic uncertainties are given in table G.1. In the following text the estimated systematic uncertainty of an input quantity, e.g. X , is indicated by δ_X .

G.2.1 Measured Asymmetry

Using the raw asymmetry calculated in equation 5.7, the charge and live time corrected asymmetry in equation 5.8 can be rewritten as

$$A_m = \frac{A_{LT} + A_Q - A_{\text{raw}} - A_{LT}A_Q A_{\text{raw}}}{A_Q A_{\text{raw}} + A_{LT}(A_{\text{raw}} - A_Q) - 1}. \quad (\text{G.8})$$

From equation G.8 it is clear that the measured asymmetry only depends on the charge and live-time asymmetries, and not their absolute values. The systematic uncertainty after correcting for the charge and live-time asymmetries is

$$(\sigma_{A_m})^2 = \frac{(A_{\text{raw}}^2 - 1)^2 \left[(A_{LT}^2 - 1)^2 \delta_{A_Q}^2 + (A_Q^2 - 1)^2 \delta_{A_{LT}}^2 \right]}{(1 - A_{\text{raw}}(A_{LT} + A_Q) + A_{LT}A_Q)^4} \quad (\text{G.9})$$

where δ_{A_Q} is the charge asymmetry systematic uncertainty and $\delta_{A_{LT}}$ is the live-time systematic uncertainty.

G.2.2 Physics Asymmetry

The asymmetry corrected for target dilution, target polarization, and beam polarization, equation 5.10, gives the total systematic uncertainty

$$(\sigma_{A_{\text{meas}}})^2 = \frac{(\sigma_{A_{\text{exp}}})^2}{f^2 P_B^2 P_T^2} + \frac{A_{\text{exp}}^2 (f^2 P_T^2 \delta_{P_B}^2 + P_B^2 P_T^2 \delta_f^2 + f^2 P_B^2 \delta_{P_T}^2)}{f^4 P_B^4 P_T^4} \quad (\text{G.10})$$

where

G.2.3 Pair Symmetric Background Corrected Asymmetry

From the equation 5.12 the systematic uncertainty with the pair symmetric background correction becomes

$$(\sigma_{A_{\text{corr}}^{BG}})^2 = \frac{\sigma_{A_{\text{meas}}}^2}{(1 - 2R)^2} + \frac{4(1 - 2R)^2 R^2 \delta_{A_{\text{pair}}}^2 + 4(A_{\text{meas}} - A_{\text{pair}})^2 \delta_R^2}{(1 - 2R)^4} \quad (\text{G.11})$$

where δ_R is the uncertainty on the estimated ratio of electrons to positrons and $\delta_{A_{\text{pair}}}$ is the pair background asymmetry (see Appendix F for more details).

G.2.4 Elastic Radiative Tail Correction

The total inelastic asymmetry is calculated by subtracted the elastic radiative tail contribution. From equation 5.15 the systematic uncertainty is

$$(\sigma_{A_{\text{corr}}^{el}})^2 = \frac{(\sigma_{A_{\text{corr}}^{BG}})^2 (\Sigma_{el} + \Sigma_{in})^2}{\Sigma_{in}^2} + \frac{\delta_{\Sigma_{in}}^2 (\Delta_{el} - A_{\text{corr}}^{BG} \Sigma_{el})^2 + (\delta_{\Delta_{el}}^2 + (A_{\text{corr}}^{BG})^2 \delta_{\Sigma_{el}}^2) \Sigma_{in}^2}{\Sigma_{in}^4} \quad (\text{G.12})$$

where $\delta_{\Delta_{in,el}}$ is the systematic uncertainty in the inelastic and elastic cross section differences and $\delta_{\Sigma_{in,el}}$ is the total uncertainty of their sum.

G.2.5 Inelastic Radiative Tail Correction

Equation G.12 shows that the complete treatment of elastic tail requires an unfolding of procedure since quantities like Δ_{in} are the primary focus of such a measurement. The inelastic radiative tail correction, equation 5.18, introduces a single systematic uncertainty δ_{in} . The main source of this uncertainty should come from the treatment of the radiative, assuming a full measurement was completed, as outlined by Mo and Tsai [69], in order to proceed to unfold the Born cross sections. However, since only asymmetries were measured this uncertainty also reflects an uncertainty from a model or fit dependence of the cross sections.

G.3 Systematic Uncertainty Estimates

Table G.1.: Systematic uncertainty estimates.

	symbol	δ	A_{180} Relative Unc.
Charge asymmetry	A_Q	0.0015	3.0%
Live-time asymmetry	A_L	0.003	6.0%
Beam polarization	P_b	0.015	1%
Target polarization	P_t	0.04	6%
Dilution factor	f	0.02	9%
Positron to electron ratio	R	0.02	
Pair Symmetric Background Asymmetry	A_{pair}	0.04	
Inelastic cross section sum	Σ_{in}	0.01	
Elastic cross section sum	Σ_{el}	0.005	
Elastic cross section difference	Δ_{el}	0.005	

APPENDIX H

TABLES OF RESULTS

This appendix contains tables of results. More useful and detailed data files of the tables below will be made available upon request¹.

H.1 A_1 and A_2 with 4.7 GeV Beam

The tables H.1–H.3 show the results for A_1^p and tables H.4–H.6 show the results for A_2^p using a 4.7 GeV electron beam. The data is split into large Q^2 bins and binned in x . The mean values of Q^2 , W , θ , and ϕ for each bin are also shown in each table.

Table H.1.: A_1 results for $1.0 < Q^2 < 2.25$ and $E = 4.7$ GeV.

x	Q^2 [GeV ²]	W [GeV]	E' [GeV]	θ [deg.]	ϕ [deg.]	A	δ_A (stat.)	δ_A (syst.)
0.20352	1.4625	2.5698	0.90652	34.007	16.341	0.25963	0.095347	0.097287
0.21136	1.512	2.5538	0.92377	34.278	16.238	0.48746	0.088355	0.098327
0.21982	1.5671	2.538	0.93703	34.69	15.688	0.36567	0.080835	0.10156
0.22908	1.6287	2.5221	0.94707	35.227	14.829	0.5547	0.07231	0.10871
0.23908	1.6972	2.5062	0.95291	35.912	13.663	0.39612	0.063408	0.11042
0.25	1.7731	2.4897	0.95657	36.702	13.405	0.51532	0.054099	0.10925
0.26191	1.8518	2.4694	0.96827	37.329	13.308	0.42719	0.047256	0.1137
0.27503	1.9366	2.4462	0.98371	37.923	13.44	0.37375	0.041773	0.11139
0.28953	2.0292	2.4204	1.0012	38.525	13.495	0.47109	0.03745	0.11739
0.30522	2.1202	2.3886	1.0341	38.745	13.749	0.49551	0.035509	0.124
0.32176	2.1598	2.3309	1.1582	36.796	13.558	0.4633	0.04665	0.069295
0.34205	2.1664	2.2468	1.3602	33.785	16.252	0.56538	0.083776	0.067955
0.36306	2.2077	2.1804	1.4949	32.446	16.945	0.76938	0.14499	0.074745
0.38822	2.2041	2.0868	1.7035	30.345	15.656	1.0569	1.7586	0.38687

¹whit@jlab.org or whit@temple.edu

Table H.2.: A_1 results for $2.25 < Q^2 < 3.5$ and $E = 4.7$ GeV.

x	Q^2 [GeV ²]	W [GeV]	E' [GeV]	θ [deg.]	ϕ [deg.]	A	δ_A (stat.)	δ_A (syst.)
0.30943	2.2642	2.4359	0.83684	44.421	12.698	-0.058687	0.25086	0.11054
0.31826	2.2879	2.4045	0.90497	42.911	14.671	0.3176	0.079285	0.079263
0.3292	2.32	2.3681	0.98041	41.504	14.709	0.32426	0.054153	0.077249
0.34081	2.3677	2.3365	1.0339	40.849	14.044	0.62097	0.048006	0.076292
0.35304	2.4249	2.3073	1.0758	40.562	14.136	0.42527	0.047126	0.07172
0.36562	2.4829	2.2776	1.1172	40.315	14.393	0.59717	0.047155	0.073788
0.37846	2.538	2.2466	1.1624	40.011	14.569	0.51116	0.048075	0.07148
0.39154	2.6008	2.2182	1.1963	39.933	14.629	0.62702	0.049936	0.07485
0.40486	2.6669	2.1906	1.2259	39.938	14.56	0.58824	0.052723	0.072297
0.41857	2.7346	2.1627	1.2546	39.972	14.55	0.59085	0.054976	0.073929
0.43315	2.8047	2.1329	1.2855	39.984	14.535	0.64742	0.057031	0.076201
0.44876	2.8781	2.101	1.3184	39.985	14.528	0.7132	0.059732	0.084452
0.46561	2.9554	2.0666	1.3536	39.986	14.594	0.55167	0.063287	0.077499
0.48382	3.0383	2.0299	1.3895	40.006	14.716	0.68841	0.067317	0.09024
0.50349	3.1244	1.99	1.4292	39.991	14.75	0.69553	0.072711	0.091688
0.52484	3.2101	1.9456	1.4766	39.85	14.847	0.69668	0.079665	0.060826
0.54763	3.2803	1.8945	1.5439	39.348	14.749	0.77289	0.095393	0.066147
0.57273	3.3089	1.8298	1.6571	38.053	13.943	0.9081	0.13149	0.06604
0.60006	3.3117	1.7571	1.7946	36.502	12.109	0.23618	0.1901	0.063408
0.63127	3.2874	1.6735	1.9606	34.688	14.008	0.25816	0.28117	0.074129
0.66538	3.3162	1.5964	2.0798	33.76	15.856	0.26182	0.50049	0.11484
0.7037	3.3703	1.5164	2.1837	33.178	15.974	0.43637	0.63244	0.066217
0.7418	3.443	1.4419	2.2624	32.935	15.869	2.3016	1.3922	0.1778
0.78193	3.4267	1.3552	2.3977	31.906	14.748	-6.8596	6.7275	0.50808

Table H.3.: A_1 results for $3.5 < Q^2 < 5.0$ and $E = 4.7$ GeV.

x	Q^2 [GeV ²]	W [GeV]	E' [GeV]	θ [deg.]	ϕ [deg.]	A	δ_A (stat.)	δ_A (syst.)
0.50023	3.506	2.0936	0.99421	51.161	14.292	-6.0859e-05	11335	0.014688
0.513	3.5328	2.0577	1.0645	49.514	16.622	0.49558	1.0189	0.25266
0.5303	3.5577	2.0079	1.1597	47.515	15.98	0.62748	0.52556	0.17122
0.54997	3.5548	1.9466	1.2909	44.884	16.701	0.4341	0.25899	0.075074
0.56805	3.5781	1.8977	1.3791	43.487	16.9	0.64018	0.17308	0.078573
0.58767	3.6214	1.8496	1.4521	42.607	17.432	0.72314	0.15909	0.073078
0.60773	3.6631	1.8013	1.5239	41.814	16.758	0.83724	0.158	0.065518
0.62826	3.7162	1.7547	1.584	41.299	15.997	0.58923	0.16022	0.061362
0.64943	3.7889	1.7103	1.6271	41.149	15.491	0.71531	0.15536	0.053639
0.6719	3.8595	1.6627	1.675	40.938	15.659	0.52603	0.17646	0.054555
0.69607	3.9367	1.6121	1.7222	40.777	15.39	0.2962	0.22298	0.067989
0.72194	4.0196	1.5582	1.769	40.655	15.879	1.0881	0.25652	0.07898
0.75012	4.0921	1.4977	1.8289	40.365	15.314	0.17798	0.24574	0.05538
0.78049	4.1533	1.431	1.9003	39.919	15.775	1.2868	0.34803	0.10214
0.81381	4.2607	1.3618	1.9462	39.95	15.82	1.3032	0.44564	0.1178
0.84916	4.3644	1.2864	1.9973	39.908	16.237	-0.51154	0.59372	0.14028
0.88881	4.4592	1.199	2.0626	39.695	15.924	1.8362	0.76968	0.1587

Table H.4.: A_2 results for $1.0 < Q^2 < 2.25$ and $E = 4.7$ GeV.

x	Q^2 [GeV ²]	W [GeV]	E' [GeV]	θ [deg.]	ϕ [deg.]	A	δ_A (stat.)	δ_A (syst.)
0.20352	1.4625	2.5698	0.90652	34.007	16.341	0.30393	0.30418	0.097287
0.21136	1.512	2.5538	0.92377	34.278	16.238	0.13267	0.27045	0.098327
0.21982	1.5671	2.538	0.93703	34.69	15.688	0.26911	0.23557	0.10156
0.22908	1.6287	2.5221	0.94707	35.227	14.829	-0.1416	0.20793	0.10871
0.23908	1.6972	2.5062	0.95291	35.912	13.663	-0.24028	0.17984	0.11042
0.25	1.7731	2.4897	0.95657	36.702	13.405	0.22828	0.15961	0.10925
0.26191	1.8518	2.4694	0.96827	37.329	13.308	0.12517	0.14412	0.1137
0.27503	1.9366	2.4462	0.98371	37.923	13.44	0.22453	0.13122	0.11139
0.28953	2.0292	2.4204	1.0012	38.525	13.495	-0.0097248	0.11924	0.11739
0.30522	2.1202	2.3886	1.0341	38.745	13.749	0.1199	0.1121	0.124
0.32176	2.1598	2.3309	1.1582	36.796	13.558	0.20589	0.13765	0.069295
0.34205	2.1664	2.2468	1.3602	33.785	16.252	-0.033791	0.23739	0.067955
0.36306	2.2077	2.1804	1.4949	32.446	16.945	0.068401	0.36228	0.074745
0.38822	2.2041	2.0868	1.7035	30.345	15.656	-0.19658	0.62789	0.38687

Table H.5.: A_2 results for $2.25 < Q^2 < 3.5$ and $E = 4.7$ GeV.

x	Q^2 [GeV ²]	W [GeV]	E' [GeV]	θ [deg.]	ϕ [deg.]	A	δ_A (stat.)	δ_A (syst.)
0.30943	2.2642	2.4359	0.83684	44.421	12.698	0.17507	0.83278	0.11054
0.31826	2.2879	2.4045	0.90497	42.911	14.671	-0.25417	0.279	0.079263
0.3292	2.32	2.3681	0.98041	41.504	14.709	0.59718	0.18504	0.077249
0.34081	2.3677	2.3365	1.0339	40.849	14.044	-0.16888	0.1551	0.076292
0.35304	2.4249	2.3073	1.0758	40.562	14.136	0.061307	0.1501	0.07172
0.36562	2.4829	2.2776	1.1172	40.315	14.393	-0.084201	0.14805	0.073788
0.37846	2.538	2.2466	1.1624	40.011	14.569	-0.17091	0.14989	0.07148
0.39154	2.6008	2.2182	1.1963	39.933	14.629	-0.045377	0.15224	0.07485
0.40486	2.6669	2.1906	1.2259	39.938	14.56	-0.16356	0.15717	0.072297
0.41857	2.7346	2.1627	1.2546	39.972	14.55	0.15849	0.16247	0.073929
0.43315	2.8047	2.1329	1.2855	39.984	14.535	-0.2418	0.16522	0.076201
0.44876	2.8781	2.101	1.3184	39.985	14.528	-0.12462	0.17121	0.084452
0.46561	2.9554	2.0666	1.3536	39.986	14.594	-0.16274	0.17877	0.077499
0.48382	3.0383	2.0299	1.3895	40.006	14.716	0.16031	0.18641	0.09024
0.50349	3.1244	1.99	1.4292	39.991	14.75	-0.12856	0.20145	0.091688
0.52484	3.2101	1.9456	1.4766	39.85	14.847	-0.0027396	0.2151	0.060826
0.54763	3.2803	1.8945	1.5439	39.348	14.749	-0.087906	0.26114	0.066147
0.57273	3.3089	1.8298	1.6571	38.053	13.943	-0.79499	0.3407	0.06604
0.60006	3.3117	1.7571	1.7946	36.502	12.109	0.93833	0.4501	0.063408
0.63127	3.2874	1.6735	1.9606	34.688	14.008	1.4907	0.63519	0.074129
0.66538	3.3162	1.5964	2.0798	33.76	15.856	0.58215	1.0772	0.11484
0.7037	3.3703	1.5164	2.1837	33.178	15.974	0.43353	1.3557	0.066217
0.7418	3.443	1.4419	2.2624	32.935	15.869	-2.4572	3.1197	0.1778
0.78193	3.4267	1.3552	2.3977	31.906	14.748	2.1793	4.6673	0.50808

H.2 A_1 and A_2 with 5.9 GeV Beam

The tables H.1–H.3 show the results for A_1^p and tables H.4–H.6 show the results for A_2^p using a 4.7 GeV electron beam. The data is split into large Q^2

Table H.6.: A_2 results for $3.5 < Q^2 < 5.0$ and $E = 4.7$ GeV.

x	Q^2 [GeV ²]	W [GeV]	E' [GeV]	θ [deg.]	ϕ [deg.]	A	δ_A (stat.)	δ_A (syst.)
0.50023	3.506	2.0936	0.99421	51.161	14.292	0.00046781	16464	0.014688
0.513	3.5328	2.0577	1.0645	49.514	16.622	2.4614	1.668	0.25266
0.5303	3.5577	2.0079	1.1597	47.515	15.98	-0.24733	0.98042	0.17122
0.54997	3.5548	1.9466	1.2909	44.884	16.701	-0.24966	0.55184	0.075074
0.56805	3.5781	1.8977	1.3791	43.487	16.9	0.9192	0.42815	0.078573
0.58767	3.6214	1.8496	1.4521	42.607	17.432	-0.55624	0.42848	0.073078
0.60773	3.6631	1.8013	1.5239	41.814	16.758	0.083842	0.41521	0.065518
0.62826	3.7162	1.7547	1.584	41.299	15.997	0.57516	0.41731	0.061362
0.64943	3.7889	1.7103	1.6271	41.149	15.491	-0.09536	0.3964	0.053639
0.6719	3.8595	1.6627	1.675	40.938	15.659	-0.24192	0.42985	0.054555
0.69607	3.9367	1.6121	1.7222	40.777	15.39	0.57247	0.52459	0.067989
0.72194	4.0196	1.5582	1.769	40.655	15.879	-1.1092	0.60961	0.07898
0.75012	4.0921	1.4977	1.8289	40.365	15.314	1.0997	0.55638	0.05538
0.78049	4.1533	1.431	1.9003	39.919	15.775	1.1022	0.76834	0.10214
0.81381	4.2607	1.3618	1.9462	39.95	15.82	-1.7362	0.982	0.1178
0.84916	4.3644	1.2864	1.9973	39.908	16.237	2.8097	1.2815	0.14028
0.88881	4.4592	1.199	2.0626	39.695	15.924	-1.6765	1.666	0.1587

Table H.7.: A_1 results for $1.0 < Q^2 < 2.25$ and $E = 5.9$ GeV.

x	Q^2 [GeV ²]	W [GeV]	E' [GeV]	θ [deg.]	ϕ [deg.]	A	δ_A (stat.)	δ_A (syst.)
0.20362	1.8843	2.8722	0.96029	33.757	17.852	0.16763	0.44475	0.20104
0.21143	1.9573	2.86	0.95869	34.501	15.919	0.24512	0.23354	0.1342
0.21992	2.0358	2.8461	0.95901	35.236	14.468	0.61591	0.15998	0.11904
0.2291	2.1219	2.8318	0.95649	36.07	13.455	0.36114	0.11698	0.10326
0.23787	2.1772	2.8028	1.0138	35.485	14.041	0.40027	0.13997	0.095259

bins and binned in x . The mean values of Q^2 , W , θ , and ϕ for each bin are also shown in each table.

Table H.8.: A_1 results for $2.25 < Q^2 < 3.5$ and $E = 5.9$ GeV.

x	Q^2 [GeV ²]	W [GeV]	E' [GeV]	θ [deg.]	ϕ [deg.]	A	δ_A (stat.)	δ_A (syst.)
0.23624	2.254	2.8579	0.80873	40.224	14.194	-0.56309	0.64314	0.23227
0.24123	2.2801	2.8377	0.85582	39.326	11.56	0.070684	0.11511	0.091254
0.24843	2.3299	2.8158	0.89493	38.903	12.032	0.27843	0.084565	0.083541
0.25679	2.3913	2.793	0.9302	38.735	13.009	0.28901	0.074665	0.077979
0.26567	2.4593	2.7708	0.95958	38.769	13.488	0.3061	0.067037	0.084039
0.27506	2.536	2.7501	0.97938	39.044	13.741	0.29318	0.060881	0.073931
0.28492	2.6199	2.7303	0.9926	39.448	13.671	0.38213	0.0563	0.071663
0.29523	2.705	2.7086	1.0101	39.742	13.821	0.34028	0.053992	0.07199
0.30598	2.7909	2.685	1.0321	39.933	14.045	0.30994	0.052622	0.071473
0.31717	2.8786	2.6602	1.0561	40.097	14.133	0.30211	0.052404	0.065535
0.32874	2.969	2.6347	1.0799	40.282	14.105	0.33319	0.05263	0.067883
0.34068	3.0611	2.6083	1.1045	40.46	14.042	0.43309	0.053388	0.063603
0.35295	3.1546	2.5811	1.1297	40.624	13.867	0.4995	0.054303	0.068022
0.36552	3.2475	2.5526	1.1582	40.709	13.744	0.4464	0.056089	0.071941
0.37826	3.3273	2.5195	1.2053	40.32	13.349	0.3923	0.058641	0.059909
0.39102	3.3757	2.4773	1.292	39.108	12.837	0.42781	0.070283	0.067674
0.40392	3.3997	2.4283	1.4071	37.524	11.341	0.58736	0.10672	0.065139
0.41722	3.3783	2.3661	1.5768	35.291	11.32	1.0351	0.25255	0.10815
0.4649	3.3713	2.1819	2.0271	30.841	13.972	0.14783	13080	0.00028915
0.48321	3.4156	2.1292	2.1246	30.294	13.805	0.21325	13319	0.0076801
0.50129	3.4476	2.0762	2.2263	29.715	13.83	0.4265	13605	0.0044683
0.52142	3.4695	2.0162	2.3453	29.023	14.35	-0.43975	14002	0.0042626

Table H.9.: A_1 results for $3.5 < Q^2 < 5.0$ and $E = 5.9$ GeV.

x	Q^2 [GeV ²]	W [GeV]	E' [GeV]	θ [deg.]	ϕ [deg.]	A	δ_A (stat.)	δ_A (syst.)
0.37499	3.5357	2.6026	0.86703	49.218	15.718	-0.14677	10805	0.090294
0.38682	3.5544	2.5524	0.99534	45.944	15.861	0.3607	0.21522	0.11568
0.39881	3.5865	2.5073	1.1002	43.801	14.642	0.42521	0.094219	0.070682
0.41227	3.6347	2.462	1.1946	42.298	13.951	0.39227	0.070549	0.061725
0.42655	3.7075	2.4215	1.261	41.586	12.997	0.47112	0.066714	0.061184
0.44179	3.803	2.3843	1.3054	41.402	12.831	0.48354	0.069772	0.062287
0.45784	3.9052	2.346	1.3474	41.302	12.694	0.47384	0.074153	0.060089
0.47452	4.0105	2.3066	1.3889	41.23	12.64	0.43891	0.078877	0.059429
0.49188	4.1186	2.2658	1.4307	41.179	12.453	0.62243	0.08467	0.077794
0.50985	4.2274	2.2233	1.4742	41.111	12.359	0.42467	0.092491	0.063748
0.52835	4.339	2.18	1.5164	41.073	12.38	0.62727	0.10016	0.078907
0.54741	4.4498	2.1349	1.5609	40.994	12.277	0.73748	0.10952	0.071825
0.5669	4.5649	2.0896	1.6017	40.968	12.307	0.69256	0.12331	0.06621
0.58697	4.675	2.0418	1.6485	40.825	12.388	0.5756	0.13563	0.07546
0.60678	4.7503	1.9894	1.7209	40.226	12.255	0.43545	0.15864	0.075189
0.6274	4.7767	1.9278	1.8357	38.969	11.981	0.68319	0.21258	0.10219
0.64849	4.8049	1.8666	1.9442	37.929	10.747	0.75308	0.31793	0.12872
0.6703	4.796	1.7997	2.0792	36.612	9.2617	1.1616	0.55475	0.20209
0.6944	4.7212	1.7198	2.2682	34.722	10.72	2.6476	1.5714	0.22924

Table H.10.: A_1 results for $5.0 < Q^2 < 7.5$ and $E = 5.9$ GeV.

x	Q^2 [GeV ²]	W [GeV]	E' [GeV]	θ [deg.]	ϕ [deg.]	A	δ_A (stat.)	δ_A (syst.)
0.56608	5.0198	2.1744	1.1664	50.6	12.938	-0.00052565	10938	0.0024209
0.60158	5.089	2.0618	1.3835	46.625	12.665	-0.33716	1.4996	0.32468
0.62172	5.0986	1.9956	1.5221	44.357	12.701	0.23012	0.31916	0.12891
0.64306	5.1658	1.9359	1.6119	43.347	13.165	0.18436	0.23454	0.092091
0.66629	5.2445	1.8727	1.6981	42.548	13.505	0.50021	0.2244	0.087002
0.69036	5.3297	1.8084	1.7788	41.907	12.842	0.68897	0.23825	0.067359
0.71554	5.457	1.7462	1.8288	41.83	12.587	0.55959	0.24932	0.094148
0.74161	5.5839	1.6809	1.8805	41.715	12.749	1.0391	0.27329	0.08103
0.76849	5.7186	1.6132	1.9274	41.702	12.654	0.50873	0.38323	0.12418
0.79597	5.8518	1.5427	1.9751	41.682	12.818	0.042863	0.43279	0.11627
0.82404	5.9894	1.4693	2.0195	41.694	13.014	1.3087	0.48957	0.13521
0.85304	6.1288	1.3913	2.0643	41.715	13.42	-1.1049	0.67396	0.20649
0.88238	6.2682	1.3097	2.1074	41.765	13.229	0.14824	0.95516	0.30396
0.91264	6.3893	1.2213	2.1619	41.646	12.7	0.76978	1.4268	0.35395

Table H.11.: A_2 results for $1.0 < Q^2 < 2.25$ and $E = 5.9$ GeV.

x	Q^2 [GeV ²]	W [GeV]	E' [GeV]	θ [deg.]	ϕ [deg.]	A	δ_A (stat.)	δ_A (syst.)
0.20362	1.8843	2.8722	0.96029	33.757	17.852	0.1092	0.12675	0.20104
0.21143	1.9573	2.86	0.95869	34.501	15.919	0.2971	0.10398	0.1342
0.21992	2.0358	2.8461	0.95901	35.236	14.468	-0.075179	0.090333	0.11904
0.2291	2.1219	2.8318	0.95649	36.07	13.455	0.091437	0.079289	0.10326
0.23787	2.1772	2.8028	1.0138	35.485	14.041	0.097685	0.082258	0.095259

Table H.12.: A_2 results for $2.25 < Q^2 < 3.5$ and $E = 5.9$ GeV.

x	Q^2 [GeV ²]	W [GeV]	E' [GeV]	θ [deg.]	ϕ [deg.]	A	δ_A (stat.)	δ_A (syst.)
0.23624	2.254	2.8579	0.80873	40.224	14.194	-3.4667	0.93863	0.23227
0.24123	2.2801	2.8377	0.85582	39.326	11.56	0.156	0.13588	0.091254
0.24843	2.3299	2.8158	0.89493	38.903	12.032	0.01234	0.093773	0.083541
0.25679	2.3913	2.793	0.9302	38.735	13.009	0.05787	0.078812	0.077979
0.26567	2.4593	2.7708	0.95958	38.769	13.488	0.10671	0.069514	0.084039
0.27506	2.536	2.7501	0.97938	39.044	13.741	0.0071657	0.063885	0.073931
0.28492	2.6199	2.7303	0.9926	39.448	13.671	0.03653	0.060738	0.071663
0.29523	2.705	2.7086	1.0101	39.742	13.821	0.11883	0.059	0.07199
0.30598	2.7909	2.685	1.0321	39.933	14.045	-0.0017938	0.058143	0.071473
0.31717	2.8786	2.6602	1.0561	40.097	14.133	0.032635	0.057696	0.065535
0.32874	2.969	2.6347	1.0799	40.282	14.105	-0.0064269	0.057945	0.067883
0.34068	3.0611	2.6083	1.1045	40.46	14.042	-0.090434	0.058523	0.063603
0.35295	3.1546	2.5811	1.1297	40.624	13.867	-0.062238	0.059637	0.068022
0.36552	3.2475	2.5526	1.1582	40.709	13.744	0.067182	0.061356	0.071941
0.37826	3.3273	2.5195	1.2053	40.32	13.349	0.062337	0.065437	0.059909
0.39102	3.3757	2.4773	1.292	39.108	12.837	0.13199	0.077686	0.067674
0.40392	3.3997	2.4283	1.4071	37.524	11.341	0.12085	0.10286	0.065139
0.41722	3.3783	2.3661	1.5768	35.291	11.32	0.065893	0.15736	0.10815
0.4649	3.3713	2.1819	2.0271	30.841	13.972	-0.70349	1013.5	0.00028915
0.48321	3.4156	2.1292	2.1246	30.294	13.805	-0.94976	1224.2	0.0076801
0.50129	3.4476	2.0762	2.2263	29.715	13.83	-1.7781	1451.3	0.0044683
0.52142	3.4695	2.0162	2.3453	29.023	14.35	1.703	1728	0.0042626

Table H.13.: A_2 results for $3.5 < Q^2 < 5.0$ and $E = 5.9$ GeV.

x	Q^2 [GeV ²]	W [GeV]	E' [GeV]	θ [deg.]	ϕ [deg.]	A	δ_A (stat.)	δ_A (syst.)
0.37499	3.5357	2.6026	0.86703	49.218	15.718	0.95135	1044.7	0.090294
0.38682	3.5544	2.5524	0.99534	45.944	15.861	-0.21184	0.1723	0.11568
0.39881	3.5865	2.5073	1.1002	43.801	14.642	-0.043533	0.1064	0.070682
0.41227	3.6347	2.462	1.1946	42.298	13.951	0.10673	0.083765	0.061725
0.42655	3.7075	2.4215	1.261	41.586	12.997	-0.045687	0.077164	0.061184
0.44179	3.803	2.3843	1.3054	41.402	12.831	0.043436	0.077634	0.062287
0.45784	3.9052	2.346	1.3474	41.302	12.694	0.090392	0.080702	0.060089
0.47452	4.0105	2.3066	1.3889	41.23	12.64	0.08416	0.084907	0.059429
0.49188	4.1186	2.2658	1.4307	41.179	12.453	0.12974	0.089936	0.077794
0.50985	4.2274	2.2233	1.4742	41.111	12.359	0.1306	0.096092	0.063748
0.52835	4.339	2.18	1.5164	41.073	12.38	0.054358	0.10365	0.078907
0.54741	4.4498	2.1349	1.5609	40.994	12.277	0.014378	0.11388	0.071825
0.5669	4.5649	2.0896	1.6017	40.968	12.307	0.053614	0.12654	0.06621
0.58697	4.675	2.0418	1.6485	40.825	12.388	-0.0094425	0.14187	0.07546
0.60678	4.7503	1.9894	1.7209	40.226	12.255	-0.029734	0.17404	0.075189
0.6274	4.7767	1.9278	1.8357	38.969	11.981	-0.15858	0.23599	0.10219
0.64849	4.8049	1.8666	1.9442	37.929	10.747	-0.49136	0.30364	0.12872
0.6703	4.796	1.7997	2.0792	36.612	9.2617	0.5095	0.4334	0.20209
0.6944	4.7212	1.7198	2.2682	34.722	10.72	0.034691	0.67964	0.22924

Table H.14.: A_2 results for $5.0 < Q^2 < 7.5$ and $E = 5.9$ GeV.

x	Q^2 [GeV ²]	W [GeV]	E' [GeV]	θ [deg.]	ϕ [deg.]	A	δ_A (stat.)	δ_A (syst.)
0.56608	5.0198	2.1744	1.1664	50.6	12.938	0.0044827	99.403	0.0024209
0.60158	5.089	2.0618	1.3835	46.625	12.665	0.38026	0.42838	0.32468
0.62172	5.0986	1.9956	1.5221	44.357	12.701	-0.46761	0.27008	0.12891
0.64306	5.1658	1.9359	1.6119	43.347	13.165	0.032125	0.242	0.092091
0.66629	5.2445	1.8727	1.6981	42.548	13.505	0.28666	0.2359	0.087002
0.69036	5.3297	1.8084	1.7788	41.907	12.842	-0.21936	0.25199	0.067359
0.71554	5.457	1.7462	1.8288	41.83	12.587	0.26626	0.26951	0.094148
0.74161	5.5839	1.6809	1.8805	41.715	12.749	-0.74906	0.28759	0.08103
0.76849	5.7186	1.6132	1.9274	41.702	12.654	0.20719	0.37653	0.12418
0.79597	5.8518	1.5427	1.9751	41.682	12.818	-0.26055	0.42538	0.11627
0.82404	5.9894	1.4693	2.0195	41.694	13.014	-0.52174	0.50673	0.13521
0.85304	6.1288	1.3913	2.0643	41.715	13.42	-0.10637	0.74638	0.20649
0.88238	6.2682	1.3097	2.1074	41.765	13.229	0.38041	1.0629	0.30396
0.91264	6.3893	1.2213	2.1619	41.646	12.7	-0.50039	1.6488	0.35395